

AD A140019

RADC-TR-83-265

Final Technical Report

December 1983



ULTRA LIGHTWEIGHT MIRROR FABRICATION TECHNOLOGY

Eastman Kodak Company

Sponsored by

Defense Advanced Research Projects Agency (DOD)

ARPA Order No. 3503

APPROVED FOR PUBLIC RELEASE; DISTRIBUTION UNLIMITED

The views and conclusions contained in this document are those of the authors and should not be interpreted as necessarily representing the official policies, either expressed or implied, of the Defense Advanced Research Projects Agency or the U.S. Government.

DTIC FILE COPY

**ROME AIR DEVELOPMENT CENTER
Air Force Systems Command
Griffiss Air Force Base, NY 13441**

**DTIC
ELECTE
S APR 11 1984 D**

D

84 04 11 005

This report has been reviewed by the RADC Public Affairs Office (PA) and is releasable to the National Technical Information Service (NTIS). At NTIS it will be releasable to the general public, including foreign nations.

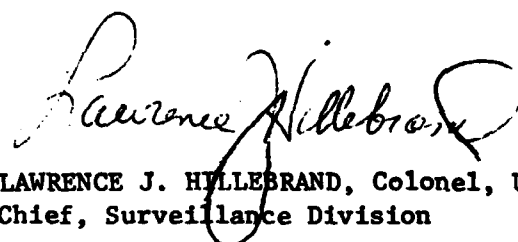
RADC-TR-83-265 has been reviewed and is approved for publication.

APPROVED:



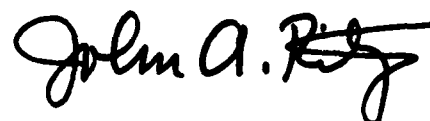
DORIS HAMILL, Capt, USAF
Project Engineer

APPROVED:



LAWRENCE J. HILLEBRAND, Colonel, USAF
Chief, Surveillance Division

FOR THE COMMANDER:



JOHN A. RITZ
Acting Chief, Plans Office

If your address has changed or if you wish to be removed from the RADC mailing list, or if the addressee is no longer employed by your organization, please notify RADC (OCSE) Griffiss AFB NY 13441. This will assist us in maintaining a current mailing list.

Do not return copies of this report unless contractual obligations or notices on a specific document requires that it be returned.

Accession For	
NTIS GRA&I	<input checked="" type="checkbox"/>
DTIC TAB	<input type="checkbox"/>
Unannounced	<input type="checkbox"/>
Justification	
By	
Distribution/	
Availability Codes	
Dist	Special
A/1	



**ULTRA LIGHTWEIGHT MIRROR
FABRICATION TECHNOLOGY**

John A. Spina

Contractor: Eastman Kodak Company
 Contract Number: F30602-79-C-0115
 Effective Date of Contract: February 1979
 Contract Expiration Date: September 1983
 Short Title of Work: Ultra Lightweight Mirror Fabrication Technology
 Program Code Number: 3E20
 Period of Work Covered: February 80 - September 83

Principal Investigator: John A. Spina
 Phone: 716-724-5277

RADC Project Engineer: Doris Hamill, Capt, USAF
 Phone: 315-330-3144

Approved for public release; distribution unlimited

This research was supported by the Defense Advanced Research Projects Agency of the Department of Defense and was monitored by Doris Hamill, Capt, USAF (OCSE) Griffiss AFB NY 13441, under Contract F30602-79-C-0115.

UNCLASSIFIED

SECURITY CLASSIFICATION OF THIS PAGE (When Data Entered)

REPORT DOCUMENTATION PAGE		READ INSTRUCTIONS BEFORE COMPLETING FORM
1. REPORT NUMBER RADC-TR-83-265	2. GOVT ACCESSION NO. AD-A140019	3. RECIPIENT'S CATALOG NUMBER
4. TITLE (and Subtitle) ULTRA LIGHTWEIGHT MIRROR FABRICATION TECHNOLOGY		5. TYPE OF REPORT & PERIOD COVERED Final Technical Report February 80 - September 83
		6. PERFORMING ORG. REPORT NUMBER CP-00673
7. AUTHOR(s) John A. Spina		8. CONTRACT OR GRANT NUMBER(s) F30602-79-C-0115
9. PERFORMING ORGANIZATION NAME AND ADDRESS Eastman Kodak Company/US Apparatus Division 901 Elmgrove Road Rochester NY 14650		10. PROGRAM ELEMENT, PROJECT, TASK AREA & WORK UNIT NUMBERS 62301E C5030101
11. CONTROLLING OFFICE NAME AND ADDRESS Defense Advanced Research Projects Agency 1400 Wilson Blvd Arlington VA 22209		12. REPORT DATE December 1983
14. MONITORING AGENCY NAME & ADDRESS (if different from Controlling Office) Rome Air Development Center (OCSE) Griffiss AFB NY 13441		13. NUMBER OF PAGES 126
		15. SECURITY CLASS. (of this report) UNCLASSIFIED
		15a. DECLASSIFICATION/DOWNGRADING SCHEDULE N/A
16. DISTRIBUTION STATEMENT (of this Report) Approved for public release; distribution unlimited		
17. DISTRIBUTION STATEMENT (of the abstract entered in Block 20, if different from Report) Same		
18. SUPPLEMENTARY NOTES RADC Project Engineer: Doris Hamill, Capt, USAF (OCSE)		
19. KEY WORDS (Continue on reverse side if necessary and identify by block number) frit space optics lightweight mirrors mirror fabrication		
20. ABSTRACT (Continue on reverse side if necessary and identify by block number) The technology for making ultra lightweight, passive, large optics for cryogenic operation in space is discussed. The key to the success of this technology is frit bonding. Frit is used with a new approach to fusion welding glass cores. The techniques for surfacing and mounting such a mirror are also developed. The mirror material is investigated to determine whether its homogeneity is adequate for the performance levels required.		

DD FORM 1473
1 JAN 73

EDITION OF 1 NOV 65 IS OBSOLETE

UNCLASSIFIED

SECURITY CLASSIFICATION OF THIS PAGE (When Data Entered)

TABLE OF CONTENTS

<u>Section</u>	<u>Title</u>	<u>Page</u>
	List of Figures	iv
	List of Tables.	vii
	Background.	viii
1.0	INTRODUCTION.	1
1.1	Program Scope	1
1.2	Summary and Conclusions	2
1.2.1	Cryogenic Mirror Performance.	2
1.2.2	Cryogenic Mirror Performance-Fused Quartz	4
1.2.3	Refractive Index Homogeneity.	5
1.2.4	Corning Glass Works Subcontract	5
1.2.5	Aspheric Mirror Fabrication Demonstration	6
1.2.6	Cryogenic Mirror Mount Evaluation	8
2.0	CRYOGENIC MIRROR PERFORMANCE - FUSED SILICA	9
2.1	Objective and Conclusions	9
2.2	Mirror Description.	9
2.3	Analytical Predictions.	11
2.3.1	Global Deformation.	11
2.4	Test Program.	15
2.4.1	Test Flow	15
2.4.2	Air Bag Test Description.	16
2.4.3	Cryogenic Test Description.	17
2.4.4	Thermal Data Acquisition System	19
2.4.5	Interferometer/Camera Assembly.	20
2.5	Test Results.	20
2.5.1	Thermal Data Summary.	20
2.5.2	Optical Quality	23
3.0	CRYOGENIC MIRROR PERFORMANCE - FUSED QUARTZ	26
3.1	Objective and Conclusions	26
3.2	Test Description - Sinter Bonded Mirror	27
3.2.1	Test Results - Sinter Bonded Mirror	28
3.3	Test Description - Fusion Bonded Mirror	35
3.3.1	Test Results - Fusion Bonded Mirror	38
4.0	REFRACTIVE INDEX HOMOGENEITY TASK	41
4.1	Objective	41
4.2	Glass Sample Description.	41
4.3	Test Description.	42
4.4	Evaluation Results.	42

<u>Section</u>	<u>Title</u>	<u>Page</u>
5.0	CORNING GLASS WORKS SUBCONTRACT	44
5.1	Summary and Conclusions	44
5.2	Frit/Glass Thermal Expansion Mismatch	44
5.3	Seal Stability.	47
5.4	Radiation Effects of Frit Bonds	48
5.5	Cleaning Alternatives	48
5.6	Nondestructive Testing.	49
5.7	Frit/Glass Interfacial Characteristics.	51
5.7.1	Chemical.	51
5.7.2	Physical.	51
5.8	L-Specimen Strength	52
5.9	1.5-Meter ULW Fused Silica Core	53
5.9.1	Background and Summary.	53
5.9.2	Design Description.	54
5.9.3	Fabrication Process	54
5.9.4	Results	56
6.0	ASPHERIC MIRROR FABRICATION DEMONSTRATION	57
6.1	Objective and Conclusions	57
6.2	Mirror Description.	58
6.3	Mirror Blank Preparation.	60
6.4	Fabrication and Test Program.	62
6.4.1	Process and Test Description.	62
6.4.2	Figure Error Results.	67
7.0	CRYOGENIC MIRROR MOUNTING	71
7.1	Objective and Conclusions	71
7.2	Material and Configuration Evaluation	72
7.2.1	Mirror Geometry and Design Conditions	72
7.2.2	Effect of Mount Materials on Induced RMS Figure Error	73
7.2.3	Effect of Mount Materials on Vertical Movement of Mirror	77
7.2.4	Fundamental Mode of Mirror/Mount Structure.	79
7.2.5	Flight-Induced Loads.	81
7.2.6	Support Leg Design Analysis	83
7.3	Cryogenic Mirror Mount Performance Evaluation	87
7.3.1	Mirror/Mount System Performance	87
7.3.2	Kinematic Cell and Attachment Geometry.	89
7.3.3	Mount Attachment Concepts	92

LIST OF FIGURES

<u>Figure</u>	<u>Title</u>	<u>Page</u>
1.1.1	Work Breakdown Structure	2
1.2.1-1	Ultra Lightweight Mirror	3
1.2.1-2	Cryogenic Test Setup	3
1.2.2-1	0.31-Meter Fused Quartz Mirrors.	4
1.2.4-1	1.5-Meter Fusion Welded 7940 Fused Silica Core	6
1.2.5-1	Demonstration Asphere.	7
1.2.6-1	Cryogenic Mirror Mount Concept	8
2.2-1	0.5-Meter Ultra Lightweight Mirror Configuration.	10
2.2-2	0.5-Meter Ultra Lightweight Mirror	10
2.3.1-1	Global Model	11
2.3.1-2	Global Model	12
2.3.1-3	Contour Map - Predicted Distortion Due to Glass/ Frit CTE Mismatch.	15
2.4.1-1	Test Flow - 0.5-Meter, Frit Bonded Mirror.	15
2.4.2-1	Air Bag Test Setup	16
2.4.3.1-1	Vacuum Chamber "C"	17
2.4.3.2-1	Cryogenic Shroud Assembly.	18
2.4.3.3-1	Insulated Fused Silica Mirror Support Assembly	18
2.4.3.3-2	Thermal Transfer Plate	19
2.4.3.3-3	Mirror Support Assembly Test Configuration	19
2.4.4-1	Instrumented Ultra Lightweight, Frit Bonded Mirror	20
2.5.1-1	Thermocouple Locations	21
2.5.1-2	Mirror Thermal Profile - Axial Gradients	22
2.5.2-1	Interferograms, 3-Point Support.	23
2.5.2-2	Surface Maps, 3-Point Support.	24
3.1-1	Fusion Bonded, 0.31-Meter, Ultra Lightweight Mirror	26
3.1-2	Sinter Bonded, 0.31-Meter, Ultra Lightweight Mirror	26
3.2-1	Test Flow, 305-Millimeter, Sinter Bonded Mirror	28
3.2-2	305-Millimeter Sintered Mirror, Mirror Thermal Profile.	29
3.2.1-1	Pre-Test Reference, 69°F.	31
3.2.1-2	Post-Test Reference, 69°F.	31
3.2.1-3	Cryogenic Temperature Test, -254°F	31
3.2.1-4	Sintered Mirror Cryogenic Test Evaluations	33
3.2.1-5	Sintered Mirror Relation of Core Geometry and Surface Error.	34
3.3-1	305-Millimeter, Fusion Bonded Mirror Test Flow Diagram.	35

<u>Figure</u>	<u>Title</u>	<u>Page</u>
3.3-2	305-Millimeter Fusion Bonded Mirror.	36
3.3.1-1	Fusion Bonded Mirror Interferograms.	38
3.3.1-2	Fusion Bonded Mirror - Cryogenic Test Evaluations.	39
3.3.1-1	Fusion Bonded Mirror - Elevated Temperature Test	40
4.2-1	60-Inch Diameter, 5-Inch Thick Boule	41
4.2-2	Homogeneity Test Setup	42
4.4-1	Interferogram of One Boule Sample.	43
4.4-2	Boule Homogeneity.	43
5.3-1	Temporal Stability of Six Test Seals	47
5.7.2-1	Micrograph Cross Section Code 7940, Fused Silica/ FN-1 Frit.	52
5.7.2-2	Micrograph Cross Section Code 7971, Fused Silica/ UA Frit.	52
5.9.1-1	Thermal Sensitivity - Fused Silica and ULE™	53
5.9.2-1	1.5-Meter Core Layout.	54
5.9.3-1	Core Fabrication Diagram	55
5.9.4-1	1.5-Meter Ultra Lightweight Mirror Core.	56
6.1-1	Demonstration Mirror Configuration	57
6.2-1	Asphere Radial and Sagittal Radii of Curvature.	59
6.2-2	Demonstration Asphere.	60
6.3-1	Slumped Mirror Blank	61
6.3-2	Mirror Blank In-Process Shaping.	61
6.4.1-1	Aspheric Departure From Minimum Removal Sphere	62
6.4.1-2	Profilometer Schematic	63
6.4.1-3	Profilometry, Space Telescope Primary Mirror . . .	63
6.4.1-4	Wavefront Test Setup	64
6.4.1-5	CO ₂ Interferometer/Display Monitor	64
6.4.1-6	Wavefront Test Setup	65
6.4.1-7	Flexible Symmetric Lap	65
6.4.1-8	Pitch Cutter	66
6.4.1-9	Demonstration Asphere in Polish.	67
6.4.2-1	Profilometer Measurements.	68
6.4.2-2	Figure Error Departure - Rough Aspherizing	68
6.4.2-3	Wavefront Error, CO ₂ Interferometry.	69
6.4.2-4	Figure Error Measurement Techniques and Results.	70
7.0-1	Cryogenic Mirror Mount Concept	71
7.2.2-1	Cryogenic Mirror Mount	74
7.2.2-2	Vertical Location of Planes.	74
7.2.2-3	Titanium Leg - Titanium Ring	75
7.2.2-4	Titanium Leg - Aluminum Ring	75
7.2.2-5	Aluminum Leg - Titanium Ring	76
7.2.2-6	Aluminum Leg - Aluminum Ring	76
7.2.2-7	Aluminum Leg - Aluminum Ring	76

<u>Figure</u>	<u>Title</u>	<u>Page</u>
7.2.3-1	Titanium Leg - Titanium Ring	78
7.2.3-2	Titanium Leg - Aluminum Ring	78
7.2.3-3	Aluminum Leg - Titanium Ring	78
7.2.3-4	Aluminum Leg - Aluminum Ring	78
7.2.3-5	Aluminum Leg - Aluminum Ring	79
7.2.4-1	Leg Stiffness For a 50 Hertz Fundamental Mode	81
7.2.5-1	Shuttle Coordinate System.	82
7.2.5-2	Flight-Induced Compressive Loads	83
7.2.6-1	Shape of Neutral Axis Under Transverse Loads . . .	84
7.2.6-2	Shape of Neutral Axis Under Longitudinal Loads.	84
7.2.6-3	Support Leg Geometry	85
7.2.6-4	Support Leg Transverse Spring Rate	86
7.2.6-5	Support Leg Longitudinal Spring Rate	86
7.3.2-1	Concept 1 of a Kinematic Cell.	90
7.3.2-2	Concept 2 of a Kinematic Cell.	90
7.3.2-3	Side-View of Kinematic Cells	91
7.3.2-4	Perspective View of Concept 1.	91
7.3.3-1	Mount Attachment Concept	93
7.3.3-2	Mount Attachment Concept	93
7.3.3-3	Geometry and Load Configuration for Flat Plate Stress Analysis.	94

LIST OF TABLES

<u>Table</u>	<u>Title</u>	<u>Page</u>
2.3.1-1	One-G/3-Point Mount Sensitivity to Mount Locations	12
2.3.1-2	One-G/3-Point Mount Sensitivity to Grid Size.	13
2.3.1-3	Isothermal Temperature Change, Thermal Strain Mismatch = 45 PPM	14
2.5.1-1	0.5-Meter Mirror Temperature Values - Cryogenic Test Series	22
2.5.2-1	Interferometric Summary 0.5-Meter Frit Bonded Mirror.	25
3.2-1	Temperature Values - Cryogenic Test Series.	30
3.2.1-2	305-Millimeter Sintered Mirror - Cryogenic Test.	34
3.3-1	Temperature Values - Cryogenic Test Series 305-Millimeter Fusion Bonded Mirror	37
3.3.1-1	305-Millimeter Fusion Bonded Mirror, Cryogenic and Elevated Temperature Test	40
4.4-1	Homogeneity Data.	42
5.2-1	FGF-Derived Expansion Mismatch for Experimental Frits Versus Code 7940.	45
5.4-1	Differential Strain Induced by Radiation Exposure for FGF Seals.	48
6.2-1	Optical Form Summary.	59
7.2.1-1	Mirror Parameters	72
7.2.2-1	Mirror Figure Sensitivity	74
7.2.2-2	Percent Dimensional Change.	75
7.2.5-1	Cargo Limit-Load Factors/Angular Acceleration for Preliminary Design.	82
7.3.1-1	Support Leg Properties.	88
7.3.1-2	Mirror/Mount System Performance	89

BACKGROUND

High performance, spaceborne, infrared surveillance systems of the future require fast, highly aspheric optical forms with smooth, low-scatter surfaces, high performance coatings, and an ultra lightweight design approach that can perform from room temperature to cryogenic temperature. The design approach must not only be rugged, low risk, and reliable, but also capable of surviving a launch environment and enduring in space for many years. A design approach, which meets performance requirements at cryogenic temperatures employing passive mirrors (without figure control actuators, sensors, electronics, etc.), offers significant advantage in weight, performance, and reliability.

For several years Kodak has been engaged in developing fused silica mirrors which meet stringent weight budgets, and optical figure quality requirements from room temperature to cryogenic temperature passively; i.e., without figure control actuators. This capability has been demonstrated with ultra lightweight fused silica, frit-bonded mirrors up to 0.5 meter in diameter. Technical issues addressed and resolved include the design and manufacture of ultra lightweight mirrors; glass/frit CTE match and bond strength, CTE homogeneity and polishing issues related to processing ultra lightweight mirrors to diffraction-limited performance. Significant advances in optical fabrication and metrology techniques have been demonstrated by the initial figuring of a 1.2-meter diameter, f/0.8 asphere representative of the highly aspheric Mini-HALO primary mirror.

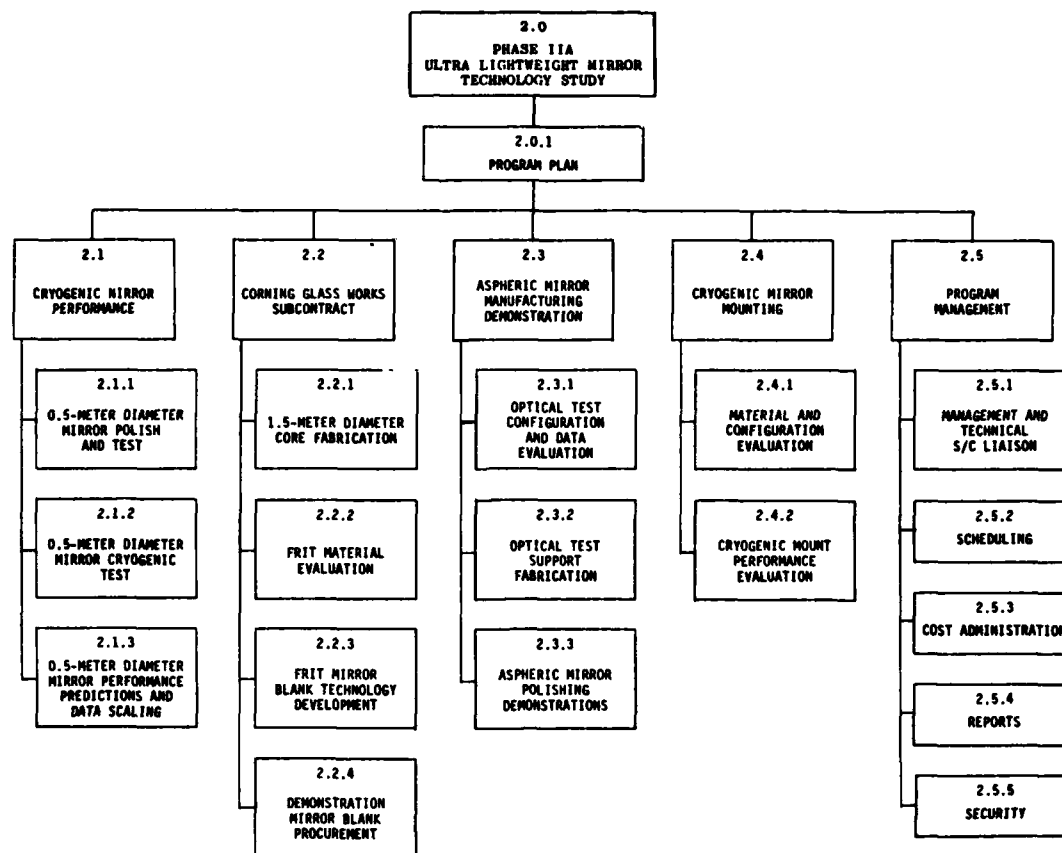
1.0 INTRODUCTION

This document is the final report for the Phase IIA Ultra Lightweight Ultra Mirror Technology Study. This work was sponsored by the Defense Advanced Research Projects Agency (DARPA) and conducted by Eastman Kodak Company under contract to Rome Air Development Center (RADC).

1.1 PROGRAM SCOPE

Advanced, high performance, spaceborne infrared surveillance systems of the future require high quality, ultra lightweight, highly aspheric mirrors capable of performing from room temperature down to cryogenic temperature (100°K). The overall objective of this effort is to investigate and demonstrate solutions to these critical technology issues.

Specifically, the Phase IIA ULW Mirror Technology Study centered on five major technical areas: (1) Cryogenic testing and analysis of a 0.5-meter diameter, ULW, fused silica mirror; (2) evaluation of frit bonding materials and processes for fused silica ULW mirror blanks; (3) development of a 1.5-meter diameter, ULW, fully sealed, fused silica core; (4) demonstration of optical fabrication techniques for a 1.2-meter diameter, $f/0.8$ asphere and; (5) design and analysis of a ULW mirror mount compatible with cryogenic temperatures. A major subcontractor in this effort is Corning Glass Works. The Work Break-down Structure for this effort is shown in Figure 1.1-1.



WORK BREAKDOWN STRUCTURE

Figure 1.1-1

1.2 SUMMARY AND CONCLUSIONS

This section summarizes the major accomplishments and conclusions reached as a result of this effort.

1.2.1 Cryogenic Mirror Performance - Fused Silica

A 0.5-meter diameter, frit bonded, fused silica, ULW mirror blank (4.5 kg) constructed under the Phase IA effort (Figure 1.2.1-1) was polished to a figure quality of 0.033 wave rms ($\lambda = 0.6328 \mu\text{m}$). This mirror, supported on a three-point kinematic mount was interferometrically tested at room

Figure 1 is a plan view of the bridge deck, which is circular. The overall diameter is labeled as 527.05 ± 0.51 . A horizontal centerline and a vertical centerline intersect at the center. On the right side of the deck, there is a rectangular area with a grid pattern, representing the impact damage. This area is labeled with a radius of $262.128 \pm 0.508 R$. The width and height of this damaged area are both labeled as 50.80 . A line points from the text "SEE DETAIL A" to the grid area. To the right of the main plan view is a detail view labeled "DETAIL A SCALE 2/1". This detail shows a cross-section of the deck with a central vertical axis. The total width of the detail is 1.270 . The distance from the centerline to the left edge is 3.810 , and the distance to the right edge is also 3.810 .

FRONT PLATE

2032.0 \pm 25.4
SPHERICAL R

DETAIL A

43.43 \pm .51

68.326

25.40

9.65 \pm 1.52
DIA ONE HOLE PER
STRUT PLATE

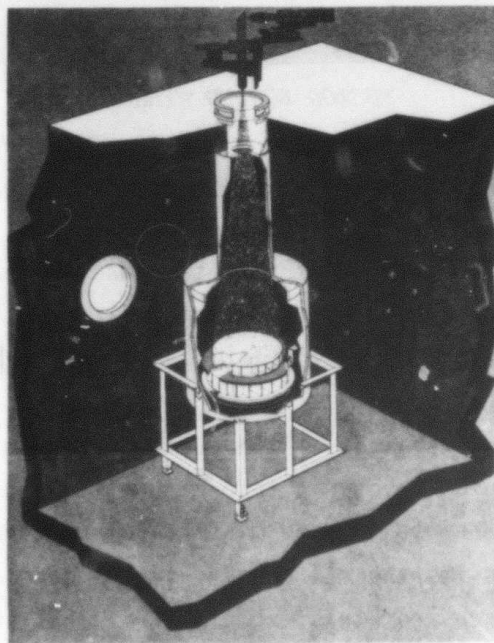
BACK PLATE

3.683 \pm .127

3.683 \pm .127

Figure 1.2.1-1

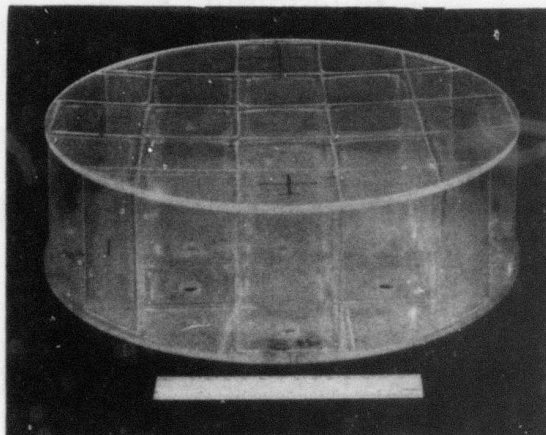
The conclusions drawn from these results are: the thermal stability of the 0.5-meter ULW frit bonded mirror is excellent and comparable to heavier, conventional fusion welded and solid fused silica mirrors; the frit bonding technique is an attractive construction approach for cryogenic application requiring minimum weight, high resonant frequency, and good optical quality.



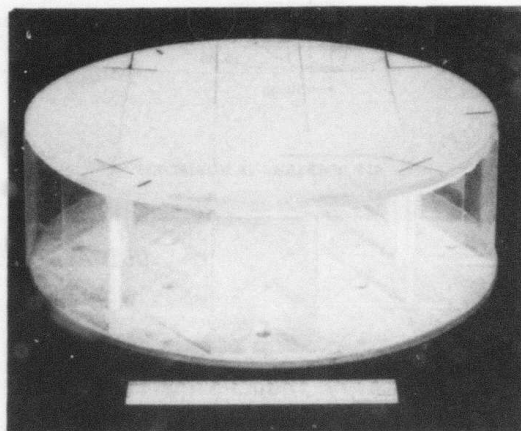
3

1.2.2 Cryogenic Mirror Performance-Fused Quartz

Two 31-centimeter diameter, fused quartz lightweight mirror blanks (Figure 1.2.2-1) were polished and cryogenically tested at Kodak. (The mirror blanks were fabricated by Heraeus Amersil in Germany.) One mirror blank was constructed using a fusion bonding (hard firing) process. The second mirror blank was constructed using a sintered glass for both core and faceplate bonding. For both mirror blanks, the core cells were formed by a tube-drawing process.



FUSION BONDED MIRROR



SINTER GLASS BONDED MIRROR

0.31-METER FUSED QUARTZ MIRRORS

Figure 1.2.2-1

The objective of this task was to evaluate the stability of these mirrors over a range of environmental conditions including static loading, thermal cycling and performance at cryogenic temperature (100°K).

The stability of the fusion bonded mirror over these environmental conditions and at cryogenic temperature was found to be excellent. Thermal testing of the sinter bonded mirror, however, revealed evidence of poor joint strength and its thermal sensitivity is considered to be unacceptable. The conclusion drawn from this experiment is that the Heraeus-Amersil fusion bonding (hard firing) process appears to be a viable approach to the fabrication of lightweight fused quartz mirror blanks. This process is worthy of further development and investigation.

1.2.3 Refractive Index Homogeneity

The objective of this task was to measure the variation in refractive index of glass samples of a Code 7940 (fused silica) glass boule selected from the current government inventory. These data will be preserved for possible future work directed at establishing correlation of refractive index inhomogeneity with coefficient of thermal expansion inhomogeneity. Evaluation showed the samples to have a maximum inhomogeneity for index of refraction of 6.3×10^{-6} (P-V).

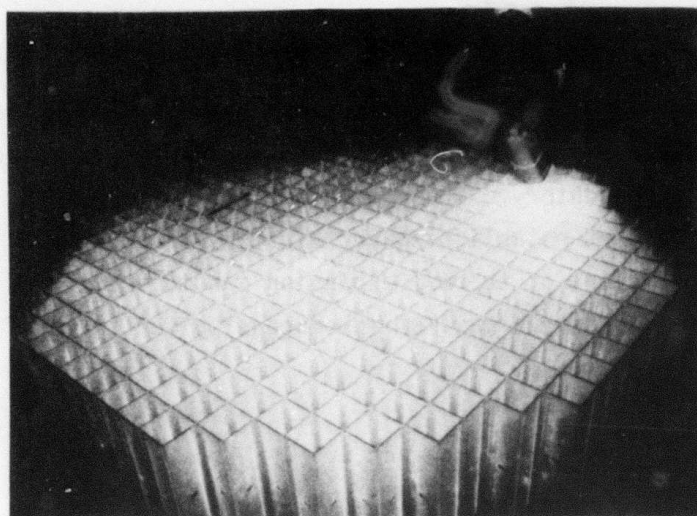
1.2.4 Corning Glass Works Subcontract

Under a subcontract from Kodak, Corning Glass Works (CGW) completed frit bonding material studies for fused silica glass and demonstrated fusion welding techniques for ULW fused silica cores.

The frit studies included characterization of frit/glass thermal expansion mismatch, physical and chemical properties, temporal stability, radiation sensitivity, and L-specimen (end-of-core joint) strength testing. Corning investigated alternative cleaning methods to the standard acid etching process and evaluated a promising nondestructive (acoustic emission) test method for frit/glass joint integrity.

The higher thermal expansivity of fused silica (Code 7940) over ULETM fused silica (Code 7971) precludes fused silica core construction in sizes above 0.5-meter using the Corning ULETM "cold core" welding techniques. Corning altered the fusion welding process for fused silica to minimize the thermal stress in the core to safe levels during fabrication.

This process was used to fabricate the 1.5-meter diameter fusion welded core shown in Figure 1.2.4-1. This core is as deep as that of the ULETM primary mirror for the Space Telescope (280 millimeters) and only half the density.



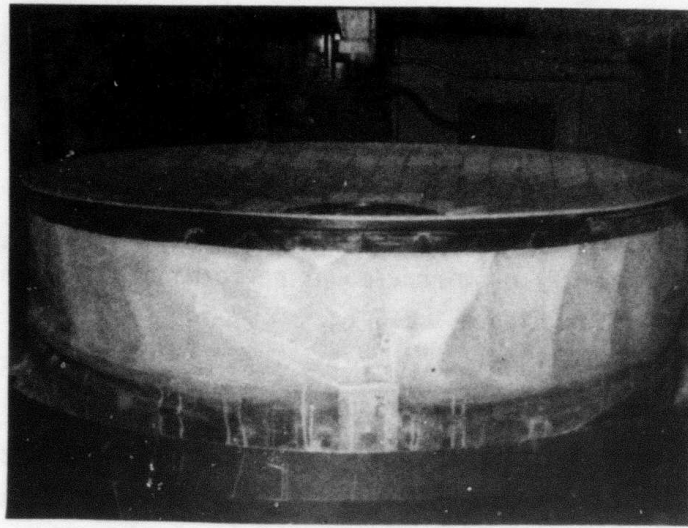
1.5-METER FUSION WELDED 7940 FUSED SILICA CORE

Figure 1.2.4-1

1.2.5 Aspheric Mirror Fabrication Demonstration

The demonstrated ability to fabricate highly aspheric, optical forms required for advanced infrared (IR) surveillance systems of the future is a key technical issue. The objective of this task was to develop and demonstrate optical fabrication and metrology techniques needed to produce mirrors with aspheric departure on order of magnitude greater than that of the NASA Space Telescope Primary Mirror; the current state-of-the-art capability.

The demonstration asphere chosen, was a 1.2-meter diameter, $f/0.8$ parabola shown in Figure 1.2.5-1. This asphere has a maximum departure from the vertex sphere of 3,870 waves ($\lambda = 0.6328 \mu\text{m}$).



DEMONSTRATION ASPHERE

Figure 1.2.5-1

This mirror blank was ground, and then aspherized using a combination of mechanical gaging techniques and CO₂ interferometry. Full-size, flexible laps were used during the polishing process. The figure error was reduced to 14 waves ($\lambda = 0.6328 \mu\text{m}$) when the funding limit for this task was reached.

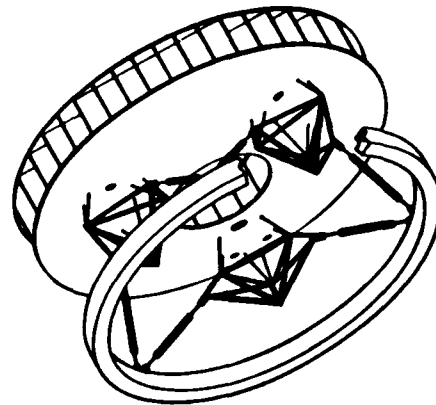
The conclusions reached from this task are:

- The mechanical gaging techniques used to track the surface profile during initial (rough) aspherizing, while adequate, were tedious and cumbersome. A more efficient profiling technique should be pursued.
- The technology to design, construct, and condition full-size laps with the flexibility required to accommodate this radical aspheric departure was demonstrated.
- Convergence demonstrated to-date indicates that this polishing technique should be capable of making a significant improvement in the figure quality of the steep asphere.

1.2.6 Cryogenic Mirror Mount Evaluation

The objective of this task was to identify and analyze a launch-compatible primary mirror mounting approach. The mount would be capable of supporting a strain-free ULW mirror from room temperature to cryogenic temperature (100°K). This study concentrated on analyzing the influence of mount attachment material and geometry on mirror/mount performance. The candidate mirror/mount concept appears in Figure 1.2.6-1.

The mount consists of a kinematic set of three (3) bipod flexures connecting the mirror through three (3) tetrahedral kinematic cells to a main support ring. The kinematic cells are attached to the backplate of the mirror using six (6) flexures to distribute the environmental loads over the mirror plate. The material and geometry of the flexures, as well as size and location of the kinematic cells are optimized for mirror dynamic modes and frequencies, minimum mirror thermal deformation and dimensional registration.



CRYOGENIC MIRROR MOUNT CONCEPT

Figure 1.2.6-1

2.0 CRYOGENIC MIRROR PERFORMANCE - FUSED SILICA

2.1 OBJECTIVE AND CONCLUSIONS

Fused silica, frit bonding materials were developed and used to construct an ultra lightweight (4.5 kilograms) 0.5-meter diameter mirror during the previous Phase IA contract effort. In designing and constructing this mirror blank, the critical issues of frit/glass joint bond strength and CTE match from the frit firing temperature to room temperature were successfully addressed. The objective of this current task was to evaluate the performance of this frit bonded mirror at cryogenic temperature (approximately 100°K).

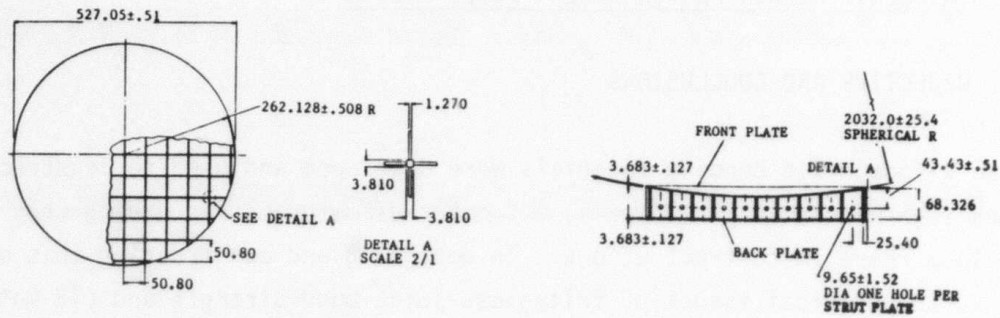
The mirror was supported on a three-point mount at room temperature (294°K) and at 108°K. The measured rms figure errors at these temperatures were 0.112 wave and 0.134 wave rms ($\lambda = 0.6328 \mu\text{m}$), respectively. The thermally-induced quilting was minimal at 0.008 wave rms.

The conclusions reached as a result of this experiment are:

- The thermal stability of the ultra lightweight, frit bonded, fused silica mirror is excellent and comparable to that of conventional, fusion welded and solid fused silica mirrors.
- The frit bonding technique is an attractive construction approach for cryogenic applications requiring minimum weight and good optical quality.

2.2 MIRROR DESCRIPTION

The 0.5-meter diameter, frit bonded, fused silica mirror has the configuration described in Figure 2.2-1. The mirror is a concave-plano with a spherical front surface radius of 2,032 millimeters. The core plates are 1.27-millimeters thick. The mirror faceplates are 3.68-millimeters thick. The core is fusion welded and the faceplates are frit bonded to the core. The finished mirror weighs 4.5 kilograms and was polished to 0.033 wave rms surface quality.

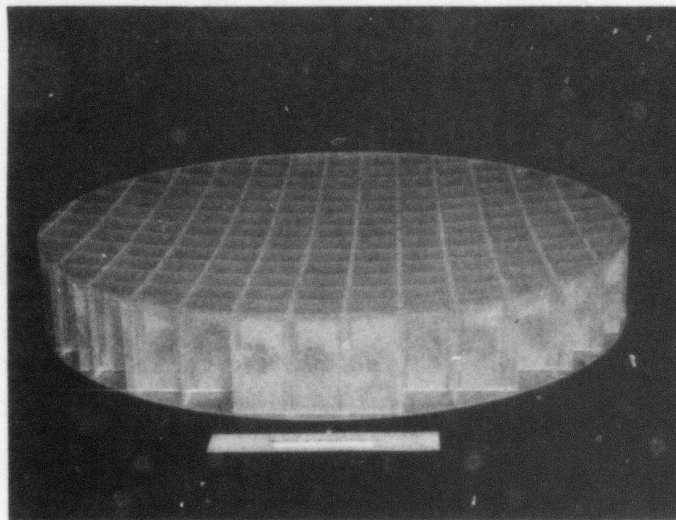


ALL DIMENSIONS IN MILLIMETERS

0.5-METER ULTRA LIGHTWEIGHT MIRROR CONFIGURATION

Figure 2.2-1

A picture of the ultra lightweight mirror is shown in Figure 2.2-2.



0.5-METER ULTRA LIGHTWEIGHT MIRROR

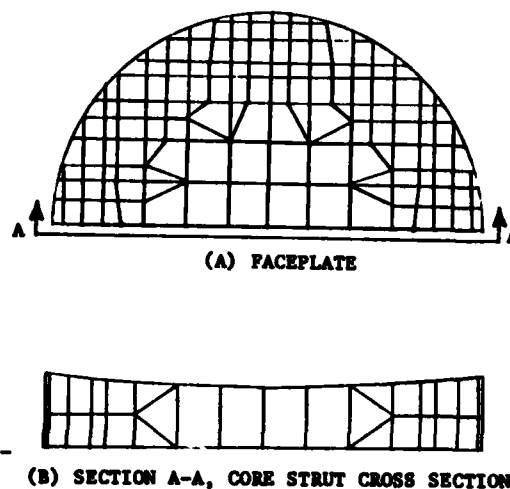
Figure 2.2-2

2.3 ANALYTICAL PREDICTIONS

The effect of the frit material on the isothermal cryogenic performance of the mirror was analyzed as described below. Mirror deformation produced by the axial strain mismatch of the frit/glass was analyzed using a finite element model of the entire mirror. The deformations produced by the axial frit strain are referred to as *global deformation*. Global deformations are represented using Zernike polynomials.

2.3.1 Global Deformation

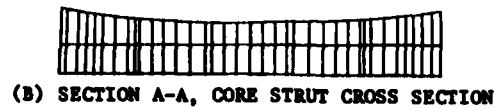
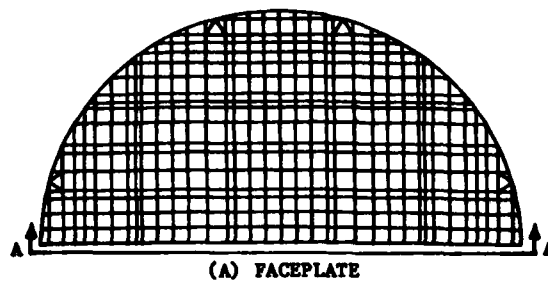
Two different finite element models of the mirror were assembled to calculate the global deformations of the mirror. The first model (Figure 2.3.1-1) had 2400 degrees of freedom, and the second model (Figure 2.3.1-2) had 7690 degrees of freedom. These models took advantage of the 180-degree symmetry of the square-cored mirror supported on a three-point mount. Two-dimensional plate elements were used to model the mirror faceplates and core struts, and the frit material was simulated by rod elements which were offset from the midplane of the mirror faceplates.



GLOBAL MODEL
(2400 DEGREES OF FREEDOM)

Figure 2.3.1-1

During cryogenic testing the mirror was supported on-back at three points, 120 degrees apart at the 0.7 radial zone. The surface deformation, produced by a one-g gravity load applied to a mirror supported in this manner, was calculated in order to determine the accuracy of the models. Two different cases were run in order to investigate the sensitivity of the model to the mount locations. The first case has all three support points located over core posts; the second case has two of the three support points located over core struts. The results are shown in Table 2.3.1-1. As expected, the major aberration is primary trefoil. The primary difference between these



GLOBAL MODEL
(7690 DEGREES OF FREEDOM)

Figure 2.3.1-2

Table 2.3.1-1						
ONE-G/3-POINT MOUNT SENSITIVITY TO MOUNT LOCATIONS						
CHARACTERISTICS	ALL SUPPORT POINTS UNDER POSTS			ONE SUPPORT POINT UNDER A POST		
	P-V	RESIDUAL P-V	RESIDUAL * RMS	P-V	RESIDUAL P-V	RESIDUAL * RMS
POWER	-0.0155	0.2794	0.0578	-0.0003	0.2291	0.0522
PRIMARY SPHERICAL	0.0333	0.2686	0.0569	0.0335	0.2185	0.0513
PRIMARY COMA	0.0026	0.2693	0.0569	0.0055	0.2171	0.0513
PRIMARY ASTIGMATISM	0.0934	0.2306	0.0536	0.018	0.2060	0.0512
PRIMARY TREFOIL	0.2766	0.1309	0.0228	0.2634	0.1167	0.0223
PRIMARY TETRAFOIL	0.0142	0.1291	0.0226	0.0003	0.1167	0.0223
PRIMARY PENTAFOIL	0.0342	0.1140	0.0221	0.0234	0.1134	0.022
PRIMARY HEXAFOIL	0.0506	0.1266	0.0209	0.0444	0.1091	0.0211
SECONDARY SPHERICAL	-0.0153	0.1316	0.0206	-0.0174	0.1158	0.0207
SECONDARY COMA	0.0026	0.1333	0.0206	0.0016	0.1165	0.0207
SECONDARY ASTIGMATISM	0.0188	0.1224	0.0204	0.0043	0.1187	0.0207
SECONDARY TREFOIL	0.1091	0.0857	0.0111	0.1129	0.0795	0.0108
TERTIARY SPHERICAL	-0.0034	0.0857	0.0111	-0.004	0.0795	0.0108
TERTIARY COMA	0.0039	0.0840	0.0111	0.0055	0.0778	0.0108
*Values indicated are residual errors after aberration removal.						

two cases is astigmatism. (The mirror is supported in test with only one support point over a post).

Comparing the results of the more detailed model to the results predicted by the coarse model provides a measure of the sensitivity of the model to grid geometry. The Zernike aberrations predicted by the two models are shown in Table 2.3.1-2. Comparison of the predicted magnitudes for the major aberration (primary trefoil) shows that there is a 12 percent difference in the results. Since these results are close, this indicates that the 7690 degree of freedom model is sufficiently detailed to accurately represent the mirror.

<p align="center"><i>Table 2.3.1-2</i> ONE-G/3-POINT MOUNT SENSITIVITY TO GRID SIZE</p>						
CHARACTERISTICS	COARSE MODEL			REFINED MODEL		
	P-V	RESIDUAL P-V*	RESIDUAL RMS*	P-V	RESIDUAL P-V*	RESIDUAL RMS*
POWER	-0.0003	0.2291	0.0522	-0.0365	0.2914	0.0594
PRIMARY SPHERICAL	0.0335	0.2185	0.0513	0.0345	0.2761	0.0585
PRIMARY COMA	0.0055	0.2171	0.0513	0.0033	0.277	0.0585
PRIMARY ASTIGMATISM	0.018	0.2060	0.0512	0.0714	0.2623	0.0566
PRIMARY TREFOIL	0.2634	0.1167	0.0223	0.2958	0.154	0.0221
PRIMARY TETRAFOIL	0.0003	0.1167	0.0223	0.0139	0.1496	0.022
PRIMARY PENTAFOIL	0.0234	0.1134	0.022	0.0289	0.1373	0.0216
PRIMARY HEXAFOIL	0.0444	0.1091	0.0211	0.0601	0.1410	0.02
SECONDARY SPHERICAL	-0.0174	0.1158	0.0207	-0.0119	0.1471	0.0198
SECONDARY COMA	0.0016	0.1165	0.0207	0.0025	0.1481	0.0198
SECONDARY ASTIGMATISM	0.0043	0.1187	0.0207	0.015	0.1473	0.0197
SECONDARY TREFOIL	0.1129	0.0795	0.0108	0.1106	0.1017	0.0108
TERTIARY SPHERICAL	-0.004	0.0795	0.0108	-0.005	0.1039	0.0107
TERTIARY COMA	0.0055	0.0778	0.0108	0.0029	0.103	0.0107
*Values indicated are residual errors after aberration removal.						

Response of the mirror to an isothermal temperature change was predicted by using the detailed finite element model. In this model the frit was simulated with one-dimensional rod elements whose line of action was assumed to act at

the back of the mirror faceplates. The thermal load was produced by giving the frit elements the measured coefficient of thermal expansion mismatch from the parent glass material. The magnitude of the load is a function of the product of this coefficient mismatch and the isothermal temperature change. For this test (100°K) the magnitude of the strain was estimated at 45×10^{-6} . Results of this load case are shown in Table 2.3.1-3. It should be noted that virtually all of the predicted aberration is random in nature. The rms surface error is small (0.003 wave rms). A contour map of the distorted surface is shown in Figure 2.3.1-3 and indicates the majority of the thermal change due to frit/glass CTE mismatch is located at the edge of the mirror.

Table 2.3.1-3
ISOTHERMAL TEMPERATURE CHANGE,
THERMAL STRAIN MISMATCH = 45 PPM

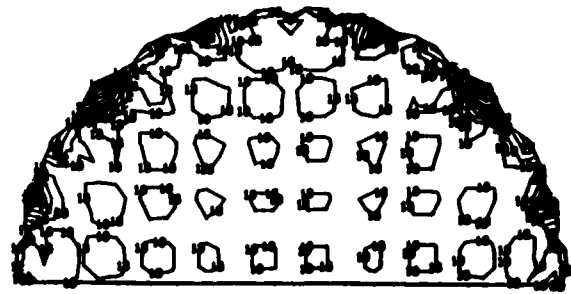
CHARACTERISTICS	P-V ($\lambda = 0.6328 \mu\text{M}$)	RESIDUAL P-V ($\lambda = 0.6328 \mu\text{M}$)	RESIDUAL RMS ($\lambda = 0.6328 \mu\text{M}$)
INPUT ARRAY	-	0.0365	0.0031
POWER	0.0032	0.0363	0.0029
PRIMARY SPHERICAL	0.0022	0.0363	0.0029
PRIMARY COMA	0.0	0.0363	0.0029
PRIMARY ASTIGMATISM	0.0002	0.0363	0.0029
PRIMARY TREFOIL	0.0	0.0363	0.0029
PRIMARY TETRAFOIL	0.0035	0.0361	0.0028
PRIMARY PENTAFOIL	0.0	0.0361	0.0028
PRIMARY HEXAFOIL	0.0	0.0361	0.0028
SECONDARY SPHERICAL	0.003	0.0361	0.0027
SECONDARY COMA	0.0	0.0361	0.0027
SECONDARY ASTIGMATISM	0.0	0.0361	0.0027
SECONDARY TREFOIL	0.0	0.0361	0.0027
TERTIARY SPHERICAL	0.0018	0.0361	0.0026
TERTIARY COMA	0.0	0.0361	0.0026

2.4 TEST PROGRAM

2.4.1 Test Flow

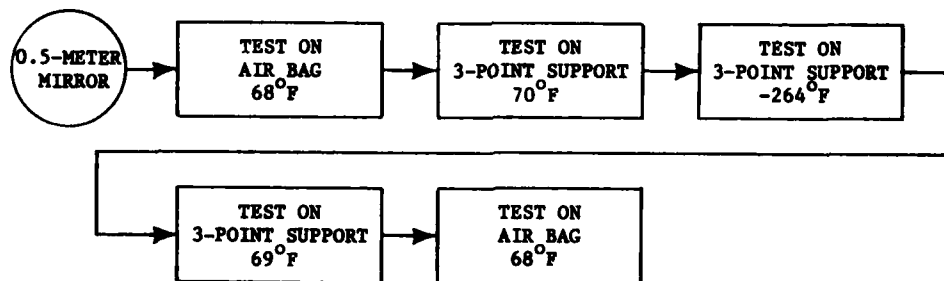
The test flow for the mirror is shown in Figure 2.4.1-1. Interferometric baseline testing first occurred at room ambient temperature and pressure with the 0.5-meter mirror supported on back on an inflatable membrane

device commonly referred to as an air bag support. After this test, the mirror was transferred to a large vacuum chamber equipped for cryogenic optical testing. For this testing, the mirror was supported on a three-point test support within a liquid nitrogen (LN_2) shroud/test stand and instrumented with temperature sensors. An interferometric reference test at room ambient and low pressure (40 micrometers) was obtained on the three-point support as a reference for subsequent testing at cryogenic temperature.



CONTOUR MAP - PREDICTED DISTORTION
DUE TO GLASS/FRIT CTE MISMATCH (100°K)

Figure 2.3.1-3



TEST FLOW - 0.5-METER, FRIT BONDED MIRROR

Figure 2.4.1-1

The cryogenic test was initiated with a controlled discharge of liquid nitrogen to the shroud with the chamber at low pressure. Thermal data was recorded at a scan rate of one channel per second for the first four hours. The scan rate was then reduced to one 18-channel scan every 15 minutes for the remainder of the monitoring period. The mirror achieved an isothermal condition after 83 hours and settled out at -263.68°F . This temperature was held for 15 hours. During this interval, interferograms of the mirror figure

error were obtained. The lowest mirror temperature recorded was -264.46°F . The maximum temperature excursion from room temperature was 336°F .

Subsequent to interferometric cryogenic testing, the vacuum chamber was repressurized to 450 millimeters with moisture-free nitrogen gas. A warmup program was initiated to return the mirror to room ambient temperature. After thermal normalization, the nitrogen atmosphere was purged from the chamber and a post-cryogenic interferometric test was conducted on the three-point support. Following this test, the chamber was repressurized and the mirror inspected for structural integrity. The mirror was then tested on the air bag support at room temperature and pressure.

2.4.2 Air Bag Test Description

Figure 2.4.2-1 is a picture of the interferometric air bag test setup used to confirm figure quality at ambient room temperature before and after exposure to the cryogenic environment.

The 0.5-meter mirror is supported on-back at the base of a vibration isolated vertical test stand. The on-back support is an inflatable membrane device commonly referred to at Kodak as an air bag. A downward-looking Twyman-Green interferometer and photographic camera are located above the mirror at the mirror center-of curvature.



AIR BAG TEST SETUP

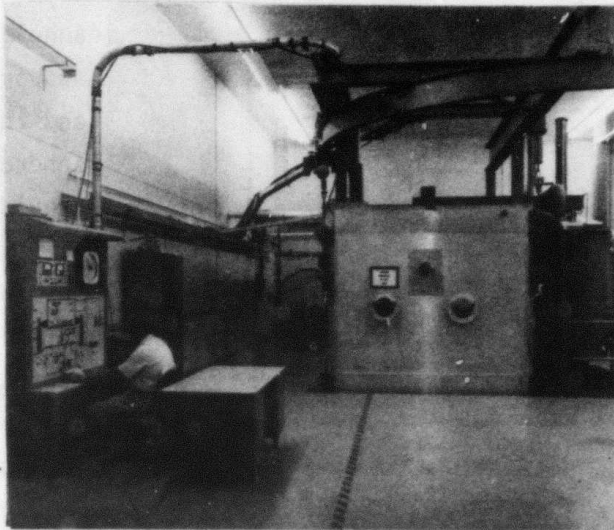
Figure 2.4.2-1

The inflated air bag provides a constant force per-unit-area support for the mirror. This results in a low strain condition in the mirror and provides a reliable and repeatable simulation of zero-gravity.

2.4.3 Cryogenic Test Description

2.4.3.1 Test Chamber - All cryogenic testing occurred in vacuum chamber "C", which was equipped with a small cryogenic shroud. Vacuum chamber "C"

(Figure 2.4.3.1-1) is a large rectangular, walk-in chamber which is 8-feet wide by 8-feet high by 16-feet long. The chamber is equipped with electrical power, instrumentation, and liquid nitrogen pass-through capability. A 10-inch diameter by 2.5-inch thick optical window is mounted to a penetration port directly above the cryogenic shroud test position.

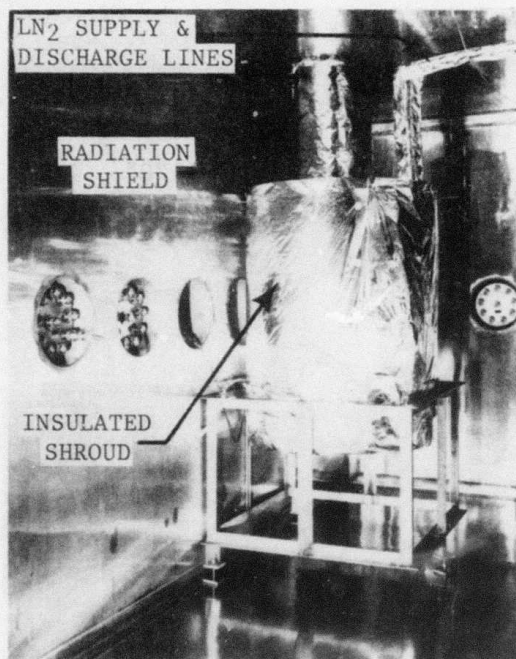


VACUUM CHAMBER "C"

Figure 2.4.3.1-1

The temperature of the chamber walls can be controlled from 40°F to 120°F. Maximum vacuum capability of the chamber is 10^{-5} torr. The chamber setup includes an internal cryogenic shroud and mirror support assembly; interferometer/camera assembly, and a thermal data acquisition system.

2.4.3.2 Cryogenic Shroud Assembly - The shroud assembly (shown in Figure 2.4.3.2-1) is a three-part cylindrical enclosure, 25 inches in diameter and 45 inches long. The side wall and removable bottom pan are double-wall, formed and welded stainless steel. The cover is a brass weldment with attached copper liquid distribution tubing. Liquid nitrogen coolant is distributed to the pan, through the side wall, to the cover, then discharged to a facility exhaust vent. The shroud assembly is mounted to a welded steel support stand. Removal of the pan provides access to the shroud enclosure for loading the test mirror. A cylindrical aluminum, thermal radiation shield, positioned between the cover and chamber ceiling, reduces thermal losses. Multilayer, aluminized polyester insulation completely encloses the shroud assembly.



CRYOGENIC SHROUD ASSEMBLY

Figure 2.4.3.2-1

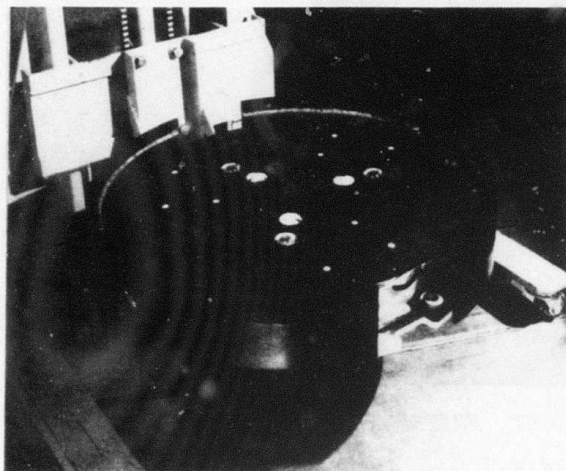
tion. A 26-inch diameter, plano/plano, fused silica blank was employed as a thermally-stable mirror mounting platform. Three concave recesses were machined into the mounting platform, thereby providing exact positioning and retention of the fused silica support spheres. The fused silica support platform is totally encased in multilayer, aluminized, polyester insulation. Three Teflon, disk type standoffs were attached to the support surface to support the thermal transfer plate. The black anodized aluminum, thermal transfer plate was incorporated into the test assembly to improve radiational thermal transfer from the backplate, effectively reducing the axial thermal gradient of the test mirror.

2.4.3.3 Mirror Support Assembly - The test mirror support assembly (Figures 2.4.3.3-1 through 2.4.3.3-3) is comprised of four structural components: an annular support ring, a fused silica support base, a thermal transfer plate, and three, fused silica mirror support spheres. The aluminum annular ring provides the mechanical interface between the mirror support assembly and the shroud. Four clearance slots machined in the ring periphery provide clearance for brackets attached to the shroud assembly. Insertion of the assembled test components into the shroud and a 10-degree clockwise rotation securely locks the assembly into the test position.



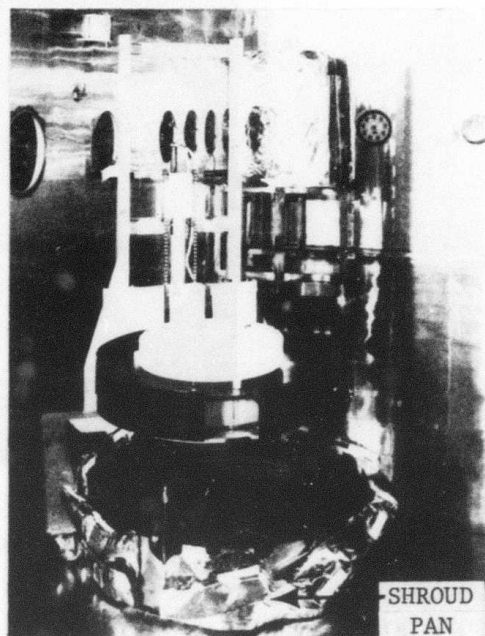
INSULATED FUSED SILICA
MIRROR SUPPORT ASSEMBLY

Figure 2.4.3.3-1



THERMAL TRANSFER PLATE

Figure 2.4.3.3-2

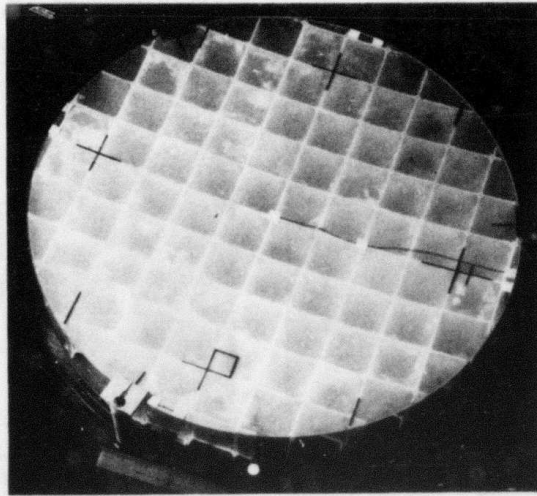


*MIRROR SUPPORT ASSEMBLY
TEST CONFIGURATION*

Figure 2.4.3.3-3

2.4.4 Thermal Data Acquisition System

A 24-channel DYMEC/Hewlett-Packard data acquisition system was used to monitor the temperature of the mirror during cryogenic testing. Data was recorded at a scan rate of one channel per second for the first 4 hours. The scan rate was reduced to one 18-channel scan every 15 minutes for the remainder of the monitoring period. Copper/constantan Type "T" thermocouples were securely attached to temperature monitoring points with compliant, fiberglass backed, pressure-sensitive tape. Each thermocouple was characterized at three temperature levels: 70°F, 32°F, and -320°F. Figure 2.4.4-1 is a picture of the instrumented ultra lightweight, frit bonded mirror.



INSTRUMENTED ULTRA LIGHTWEIGHT, FRIT BONDED MIRROR

Figure 2.4.4-1

2.4.5 Interferometer/Camera Assembly

A Twyman-Green interferometer was positioned outside the chamber optical window at the center of curvature of the 0.5-meter diameter fused silica mirror. The interferometer, which was aligned normal to the window, used a 0.6-inch diameter aperture window area. Interferograms were recorded with a 35-millimeter single lens, reflex camera.

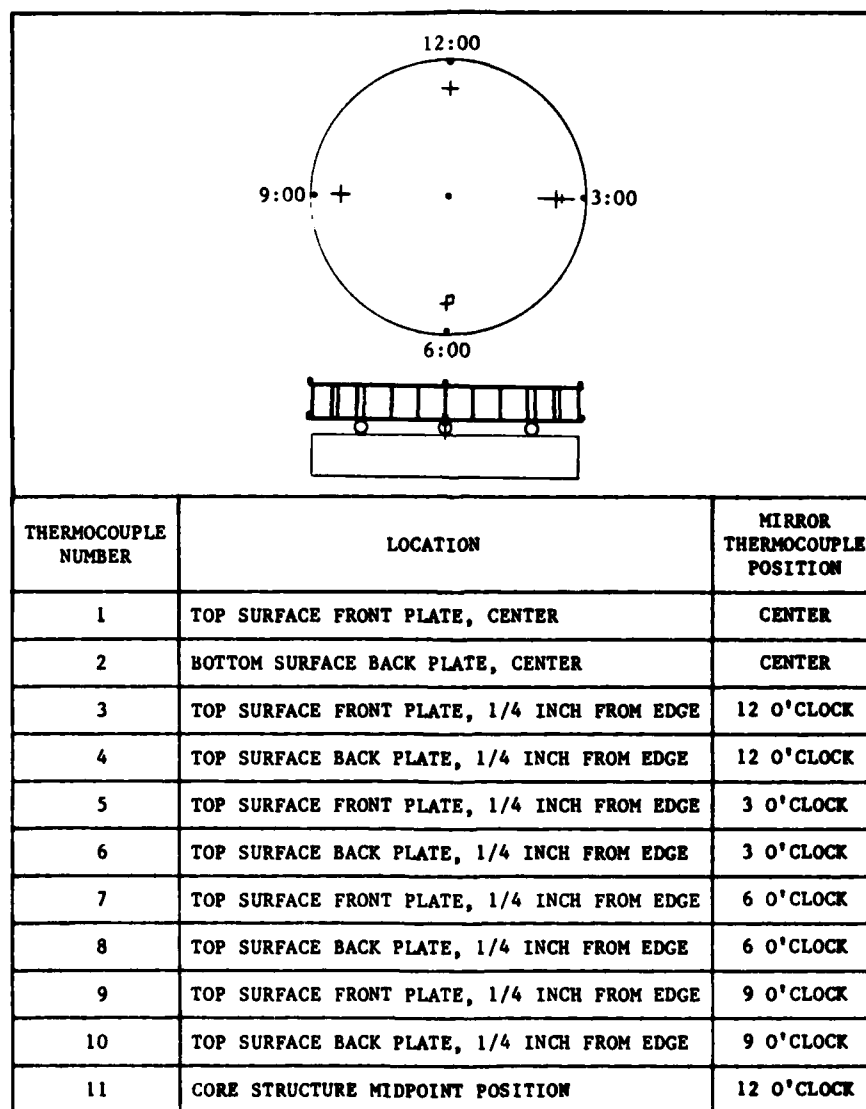
2.5 TEST RESULTS

2.5.1 Thermal Data Summary

Eleven thermocouples were attached at selected mirror locations (Figure 2.5.1-1). Thermocouple 1 was attached to the top surface center position of the front plate. Thermocouple 2 was attached to the bottom surface center position of the back plate. Thermocouples 2, 5, 7, and 9 were attached to the top surface of the front plate, one-quarter inch in-board from the outside edge at the 12, 3, 6, and 9 o'clock positions, respectively. Thermocouples 4, 6, 8, and 10 were attached to the top surface of the back plate, one-quarter inch from the edge at the 12, 3, 6, and 9 o'clock positions, respec-

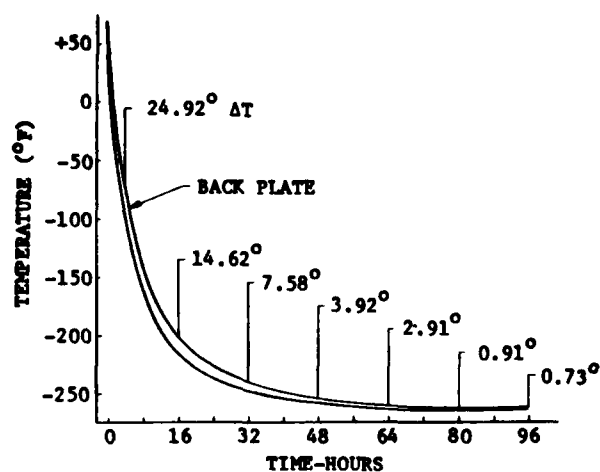
tively. Thermocouple 11 was attached to the core structure midway between the plates at the 12 o'clock position. These positions were chosen to measure axial, radial, and circumferential thermal gradients. Additional thermocouples were attached to locations of general interest (the fused silica mirror support, the thermal transfer plate, shroud surfaces, etc.).

Table 2.5.1-1 summarizes the temperature values and thermal gradient data for each of the interferometric tests. Figure 2.5.1-2 illustrates the mirror thermal profile during cooldown.



THERMOCOUPLE LOCATIONS

Figure 2.5.1-1



MIRROR THERMAL PROFILE -
AXIAL GRADIENTS

← Figure 2.5.1-2

Table 2.5.1-1

0.5-METER MIRROR TEMPERATURE VALUES -
CRYOGENIC TEST SERIES

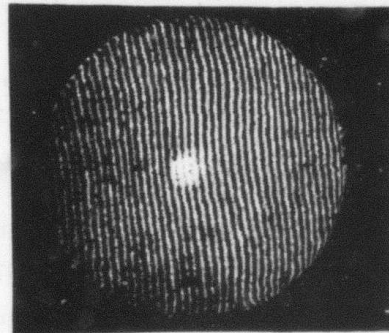
INTERFEROMETRIC EVALUATION		PRE-TEST REF AMBIENT TEMP VACUUM	CRYO TEMP VACUUM	POST TEST REF AMBIENT TEMP VACUUM
ELAPSE TIME		-	95.5 HOURS	-
LOCATION	TC	TEMP (°F) ΔT (°F)	TEMP (°F) ΔT (°F)	TEMP (°F) ΔT (°F)
FRONT PLATE CENTER	1	70.45 0.12	2.61 0.50	68.76 0.36
BACK PLATE	2	70.33	-261.92	68.40
FRONT PLATE 12 O'CLOCK	3	70.37 0.07	-264.75 0.50	68.60 0.14
BACK PLATE	4	70.30	-264.25	68.46
FRONT PLATE 3 O'CLOCK	5	70.40 0.04	-264.67 1.00	68.58 0.11
BACK PLATE	6	70.36	-263.67	68.49
FRONT PLATE 6 O'CLOCK	7	70.43 0.14	-264.33 0.75	68.66 0.19
BACK PLATE	8	70.57	-263.58	68.85
FRONT PLATE 9 O'CLOCK	9	70.57 0.18	-264.75 0.67	68.82 0.03
BACK PLATE	10	70.75	-264.08	68.85
12 O'CLOCK MIDPOINT SUPPORT STRUCTURE	11	70.52	-259.62	68.61
AVERAGE AXIAL ΔT EDGE LOCATIONS		0.11	0.73	0.12
MAXIMUM RADIAL ΔT		0.11	1.08	0.17

2.5.2 Optical Quality

Representative interferograms obtained at room temperature and cryogenic temperature (-264°F) on the three-point support are shown in Figure 2.5.2-1. The character of each is similar and dominated by the gravity distortion effect of the three-point support. Little quilting (polishing or thermally-induced) is evident. Interferograms from each test were processed and contour surface maps were generated as shown in Figure 2.5.2-2. Included is the point-to-point difference or delta map between the reference and cryogenic test. The rms surface error at room temperature is 0.112 wave rms. The dominant character of the figure error is, a trefoil pattern stemming from the three-point support. The rms surface error at cryogenic temperature is only slightly higher at 0.134 wave rms. The dominant figure error at cryogenic temperature is also the gravity-related trefoil pattern. The magnitude of the delta map between the room temperature test and cryogenic test is 0.06 wave rms. The character of this map is predominantly random.



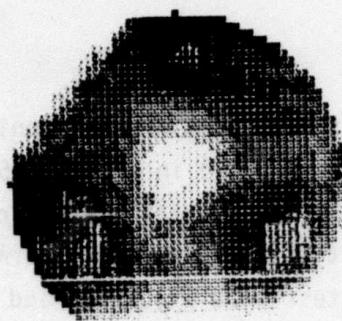
REFERENCE TEST, 70°F



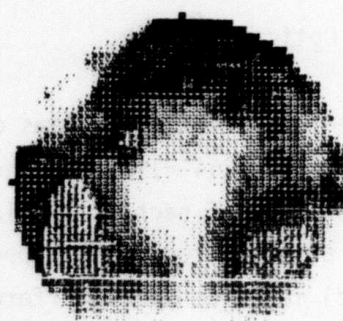
CRYOGENIC TEST, -264°F

INTERFEROGRAMS, 3-POINT SUPPORT

Figure 2.5.2-1



REFERENCE TEST, 70°F
0.112 λ RMS



CRYOGENIC TEST, -264°F
0.134 λ RMS



DELTA MAP, REF.- CRYOGENIC TEST
0.06 λ RMS

SURFACE MAPS, 3-POINT SUPPORT

Figure 2.5.2-2

The thermally-induced quilting was evaluated by subjecting the delta map of Figure 2.5.2-2 to a special quilting analysis routine which operates on the surface error which is spatially correlated with the core (cell) spacing after all Zernike aberrations have been removed. This analysis indicates the thermally-induced quilting was quite small (0.008 wave rms).

Table 2.5.2-1 summarizes the figure error results obtained at room temperature and cryogenic temperature. The post cryogenic testing at room temperature on the three-point support and on the air bag support produced virtually identical results to those obtained prior to exposure to the cryogenic environment.

Table 2.5.2-1 INTERFEROMETRIC SUMMARY 0.5-METER FRIT BONDED MIRROR				
TEST	TEMPERATURE °F	PRESSURE	RMS VALUE	P-V VALUE
AIRBAG	68	1 ATMOSPHERE	0.033	0.17
REFERENCE 3-POINT SUPPORT	70	40 μ m	0.113	0.67
CRYOGENIC 3-POINT SUPPORT	-264	70 μ m	0.134	0.88
REFERENCE 3-POINT SUPPORT	69	60 μ m	0.112	0.65
AIRBAG	68	1 ATMOSPHERE	0.033	0.16

The conclusions reached from these results are:

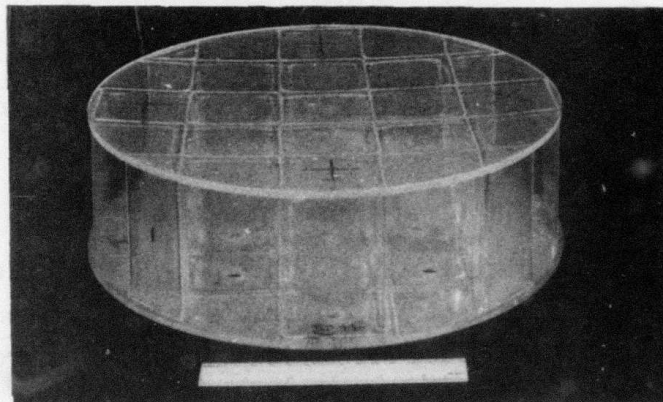
- The thermal stability of the 0.5-meter ULW frit bonded mirror is excellent and comparable to that of conventional (heavier) fusion-welded and solid fused silica mirrors.
- The thermally induced quilting is negligible.
- The frit bonding technique is an attractive construction approach for cryogenic applications requiring minimum weight, high resonant frequency, and good optical quality.

3.0 CRYOGENIC MIRROR PERFORMANCE - FUSED QUARTZ

3.1 OBJECTIVE AND CONCLUSIONS

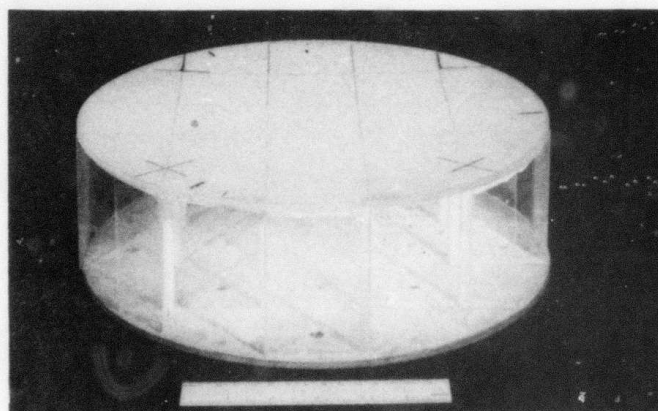
The objective of this task was to evaluate the performance and environmental stability of two 305-millimeter diameter, ULW, fused quartz mirrors. The two fused quartz ULW mirror blanks, fabricated by Heraeus Amersil Company in Germany, were polished, thermal tested, and evaluated at Kodak. These activities took place over a period from September 1982 to April 1983 under joint DARPA/Kodak funding.

Both mirrors are geometrically identical, having 60-millimeter square tubes with 2-millimeter thick walls joined at the corners to form a lightweight core to which 5-millimeter thick facesheets are bonded. The core cells were formed by a tube drawing process. Different bonding methods were used to fabricate each of these 2.44-kilogram mirrors. A fusion bonding (hard firing) process was used on one mirror (Figure 3.1-1) and the other (Figure 3.1-2) relied on sintered glass as the bonding agent. The sintered glass on both facesheets is responsible for the white, snow-like appearance of this mirror.



*FUSION BONDED, 0.31-METER,
ULTRA LIGHTWEIGHT MIRROR*

Figure 3.1-1



*SINTER BONDED, 0.31-METER,
ULTRA LIGHTWEIGHT MIRROR*

Figure 3.1-2

The fusion bonded (hard firing) lightweight mirror blank was polished to a spherical shape and a 0.086 wave rms surface error as tested on an air bag support. This mirror was evaluated interferometrically over a temperature range from room ambient (294⁰K) to 95⁰K; was evaluated at 365⁰K after seven thermal cycles to this temperature and at room temperature after ten cycles of mechanical loading equivalent to four times gravity loading. The stability of this mirror over these environmental conditions is considered to be excellent. The interferometrically measured surface rms change (point-to-point) from room temperature to 95⁰K was 0.042 wave rms.

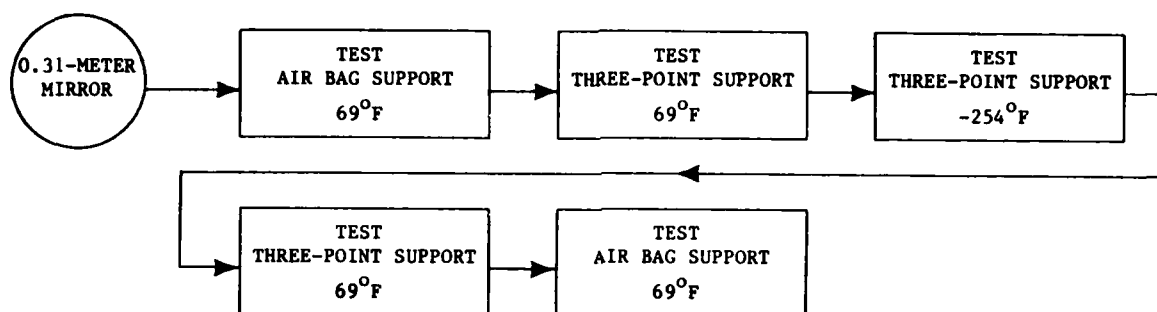
The sinter bonded ULW mirror blank was ground and polished to a spherical shape with and a 0.106 wave rms surface error, as tested on an air bag support. The sinter bonded mirror was evaluated at 115⁰K. The measured surface rms (delta) change from room temperature to 115⁰K was 0.115 wave rms. This mirror revealed evidence of poor vertical joint strength and its thermal sensitivity is considered to be unacceptable.

The thermal stability of the 305-millimeter, fusion bonded, lightweight mirror from 95⁰K is considered excellent. Structural stability after exposure to thermal and mechanical bonding was verified. This mirror exhibits good bonding strength, with a low and uniform coefficient of thermal expansion over the temperature range tested. The Heraeus Amersil process of drawing fused quartz tubes and fusing these together to form a lightweight core appears to be a viable and attractive approach to the fabrication of lightweight mirror blanks. This process is worthy of further development and investigation.

3.2 TEST DESCRIPTION - SINTER BONDED MIRROR

The test flow for the sinter bonded mirror is indicated in Figure 3.2-1 and is identical to that described in Paragraph 2.4.1 for the fused silica, frit bonded mirror. This testing included an air bag support baseline

testing before and after cryogenic testing and testing in a thermal vacuum chamber on a three-point kinematic support at room temperature and cryogenic temperature. The thermal data acquisition system, interferometric test system, and test support devices used are described in Section 2.4 of this report.



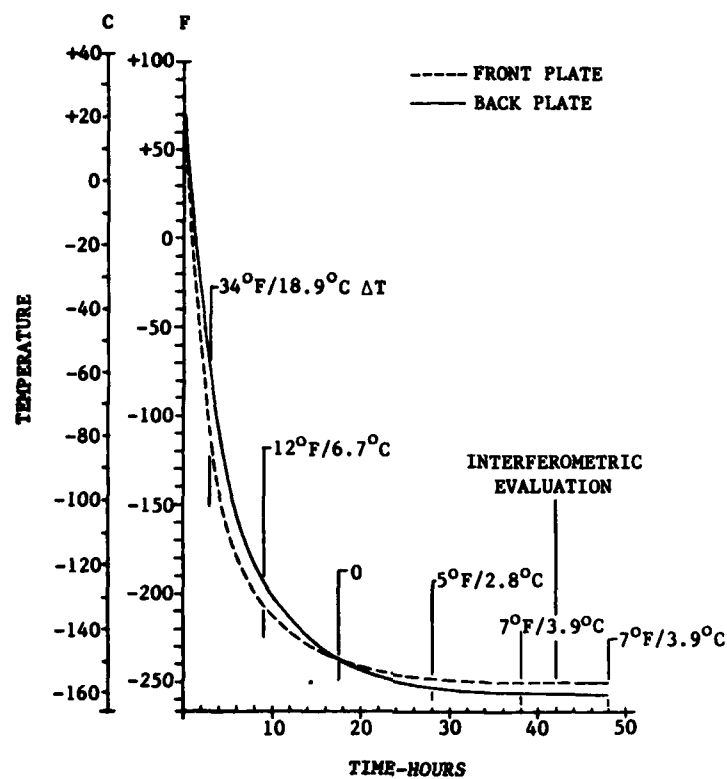
TEST FLOW
305-MILLIMETER, SINTER BONDED MIRROR

Figure 3.2-1

Low temperature testing of this mirror occurred in February 1982. Isothermal conditions were achieved after 41.5 hours of LN₂ discharge and stabilized at an average mirror temperature of -254°F. The average front-to-back plate edge position, axial, thermal gradient was 5.70°F. Maximum radial thermal gradients were 5.57°F and 2.97°F for front and back plate sensor positions, respectively. Figure 3.2-2 displays the test mirror thermal profile and typical edge location axial gradients at various test intervals. Table 3.2-1 displays the temperature values and thermal gradients for reference and cryogenic temperature testing.

3.2.1 Test Results - Sinter Bonded Mirror

Interferograms of the sinter bonded mirror supported on three points in the test stand at 70°F before and after thermal testing are shown in Figures 3.2.1-1 and 3.2.1-2. The pre- and post-test wavefronts have no discernable difference, and indicate good test repeatability. At approximately 115°K, a significant degradation was apparent in the interferogram as shown in Figure 3.2.1-3.



305-MILLIMETER SINTERED MIRROR
MIRROR THERMAL PROFILE

Figure 3.2-2

Table 3.2-1

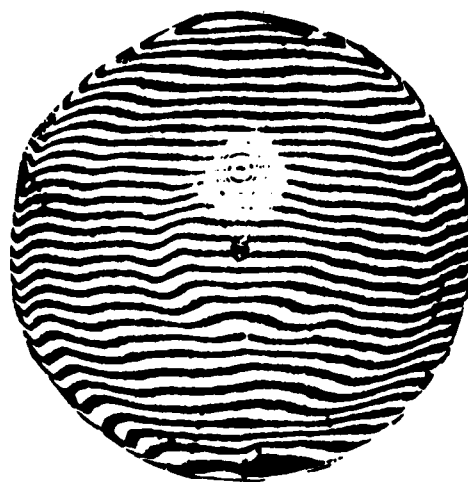
TEMPERATURE VALUES - CRYOGENIC TEST SERIES
(305-MILLIMETER SINTERED MIRROR)

INTERFEROMETRIC EVALUATION		SINTERED MIRROR ASSEMBLY											
		1				2				3			
		PRE-TEST REFERENCE AMBIENT TEMPERATURE LOW PRESSURE				CRYOGENIC TEMPERATURE LOW PRESSURE				POST-TEST REFERENCE AMBIENT TEMPERATURE LOW PRESSURE			
ELAPSE TIME		-				41.5 HOURS				-			
LOCATION	TC	TEMPERATURE		ΔT		TEMPERATURE		ΔT		TEMPERATURE		ΔT	
		$^{\circ}F$	$^{\circ}C$	$^{\circ}F$	$^{\circ}C$	$^{\circ}F$	$^{\circ}C$	$^{\circ}F$	$^{\circ}C$	$^{\circ}F$	$^{\circ}C$	$^{\circ}F$	$^{\circ}C$
FRONT PLATE	1	68.77	20.43	0.16	0.09	-246.73	-154.85	8.27	4.59	69.40	20.78	0.17	0.10
CENTER	2	68.61	20.34			-255.00	-159.44			69.23	20.68		
BACK PLATE													
FRONT PLATE	3	68.77	20.43	0.14	0.08	-244.33	-156.29	6.05	3.36	69.36	20.76	0.07	0.04
12 O'CLOCK	4	68.63	20.35			-255.38	-159.66			69.29	20.72		
BACK PLATE													
FRONT PLATE	5	68.80	20.44	0.13	0.08	-252.04	-157.80	4.24	2.36	69.37	20.76	0.05	0.03
3 O'CLOCK	6	68.65	20.36			-258.28	-160.06			69.32	20.73		
BACK PLATE													
FRONT PLATE	7	68.68	20.37	0.10	0.06	-250.87	-157.15	7.10	3.94	69.31	20.73	0.15	0.08
6 O'CLOCK	8	68.78	20.43			-257.97	-161.09			69.46	20.81		
BACK PLATE													
FRONT PLATE	9	68.62	20.34	0.23	0.13	-252.30	-157.94	5.42	3.01	69.16	20.64	0.36	0.20
9 O'CLOCK	10	68.85	20.47			-257.72	-160.96			69.52	20.84		
BACK PLATE													
MAXIMUM RADIAL ΔT		$^{\circ}F$	$^{\circ}C$	$^{\circ}F$		$^{\circ}C$		$^{\circ}F$		$^{\circ}C$		$^{\circ}F$	
FRONT PLATE		0.15		0.09		5.57		3.09		0.24		0.14	
BACK PLATE		0.24		0.13		2.97		1.65		0.29		0.16	
AVERAGE AXIAL ΔT		$^{\circ}F$	$^{\circ}C$	$^{\circ}F$		$^{\circ}C$		$^{\circ}F$		$^{\circ}C$		$^{\circ}F$	
EDGE LOCATIONS		0.15		0.09		6.22		3.45		0.16		0.09	



PRE-TEST REFERENCE , 69°F

Figure 3.2.1-1



POST-TEST REFERENCE , 69°F

Figure 3.2.1-2



CRYOGENIC TEMPERATURE TEST , -254°F

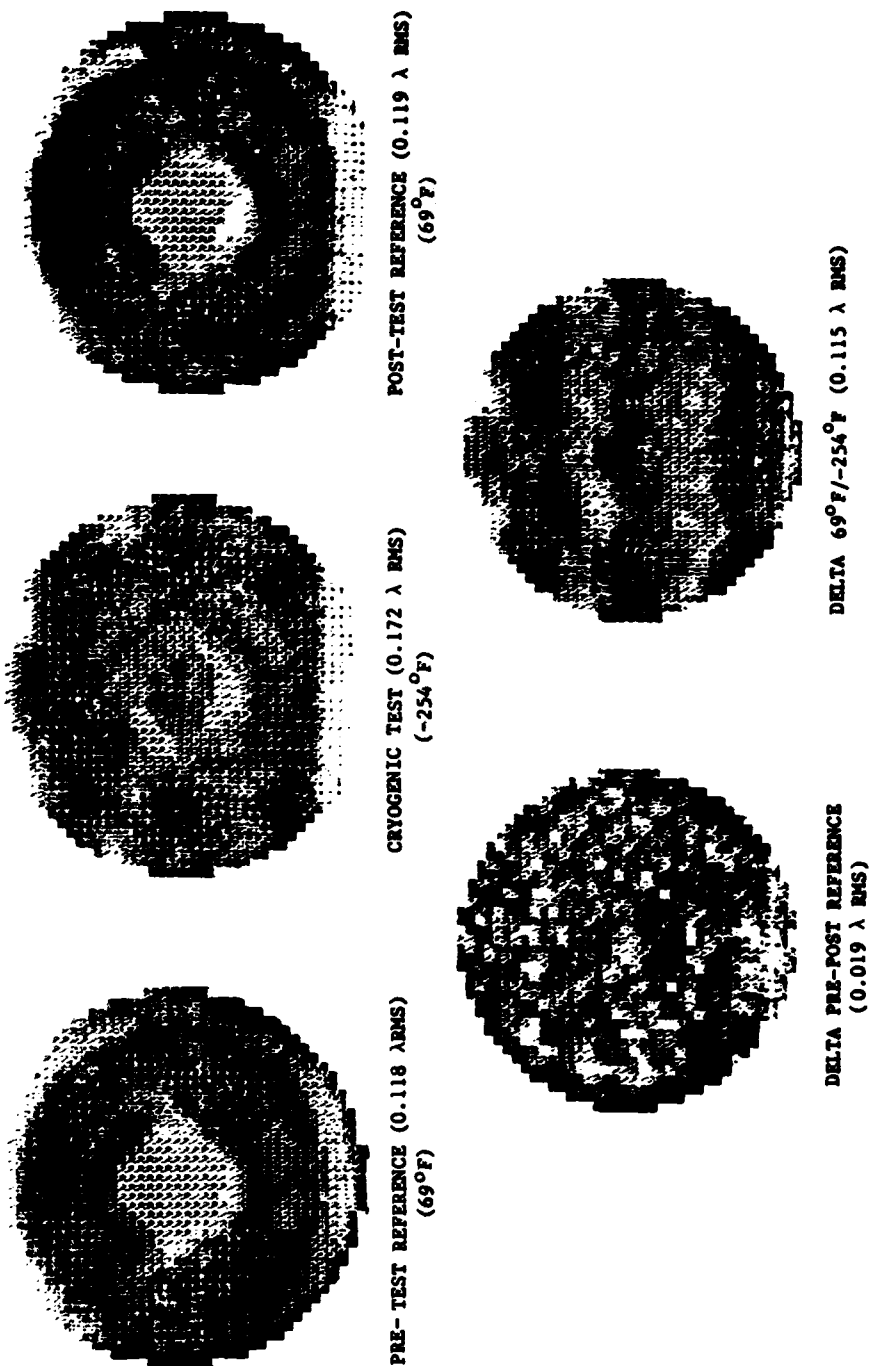
Figure 3.2.1-3

INTERFEROGRAMS, SINTER BONDED MIRROR

The cryogenic test evaluations are presented in Figure 3.2.1-4 as computer generated surface contour maps and computer evaluated surface error magnitudes. The dark areas of the maps indicate the relative highs. The light shading of the maps indicate the relative lows. Both the pre- and post-test contours are essentially identical, with primary spherical as the principal aberration. The delta map; a point-for-point subtraction of the pre-test from the post-test data; shows a predominantly random difference. The delta magnitude of 0.019 wave rms is small and within the test error for a single orientation, three-point support test. This data indicates that no permanent change to the mirror occurred during the cryogenic test.

At 115°K a significant change in the surface character and the amount of surface error (0.172 wave rms) is apparent. The delta map shows the change from room temperature to 115°K to be large (0.115 wave rms) and consists of a regular pattern of alternating high and low regions corresponding to the core cell spacing. Comparison of the delta map with the mirror structure shows that the high areas are within the square tubes which form the core. The low areas occur in the spaces formed by the sides of four individual square tubes joined at their corners. This situation is shown in Figure 3.2.1-5 where the outline of the five full square tubes in the core have been superimposed on the delta map. The positions of the remaining tubes can be visualized and their correspondence to the surface contour readily seen.

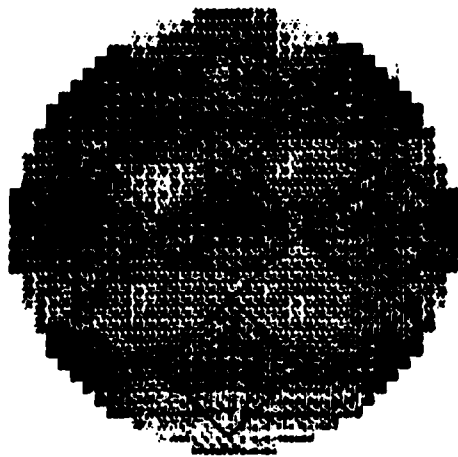
The most likely cause of this phenomenon is core-to-plate CTE mismatch combined with low vertical joint (tube-to-tube) bond strength. As the mirror temperature is lowered, the tubes will tend to contract radially. Without strong bonds, differential contraction between the core and faceplates will cause the tubes to produce a force at the back surface of the faceplate; caused by compression within the tubes. The offset from the faceplate neutral axis can result in bending moments which produce the observed checkerboard pattern. This test revealed a fundamental problem with the sinter bonded mirror, and no additional thermal tests were conducted.



$$\lambda = 0.6328 \mu\text{m}$$

SINTERED MIRROR CRYOGENIC TEST EVALUATIONS
(THREE POINT SUPPORT)

Figure 3.2.1-4



*SINTERED MIRROR
RELATION OF CORE GEOMETRY AND
SURFACE ERROR*

Figure 3.2.1-5

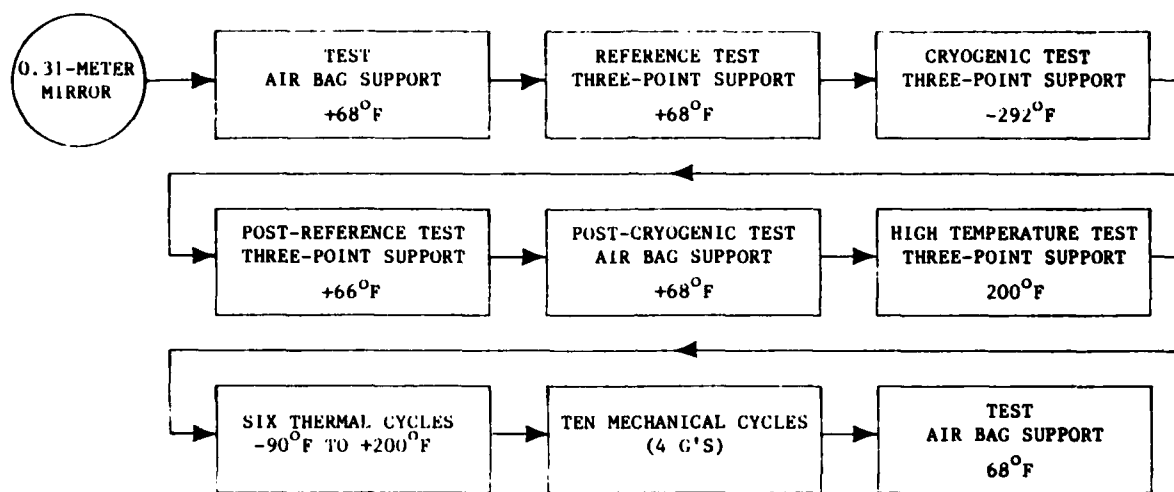
A post cryogenic test evaluation conducted on an air bag support resulted in a measured surface figure quality of 0.102 wave rms (0.59λ P-V). The point-for-point subtraction from the previous air bag test data resulted in a delta of 0.011 wave rms (0.09λ P-V). The magnitude of this delta indicates that no permanent structural changes occurred during the thermal cycle. Table 3.2.1-2 summarizes the interferometric test data for this mirror.

Due to the apparent problem with the sintered bonds at cryogenic temperatures, further testing and evaluation was discontinued on this mirror.

<i>Table 3.2.1-2</i>		
<i>305-MILLIMETER SINTERED MIRROR - CRYOGENIC TEST</i>		
INTERFEROMETRIC EVALUATION	RMS VALUE (6328 Å)	P-V VALUE (6328 Å)
PRE-TEST, AIR BAG SUPPORT BASELINE, 294°K (69°F)	0.106	0.6175
PRE-TEST, THREE-POINT SUPPORT REFERENCE LOW PRESSURE, 294°K (69°F)	0.118	0.6196
CRYOGENIC TEST, THREE-POINT SUPPORT LOW PRESSURE, 115°K (-254°F)	0.172	1.3075
POST-TEST, THREE-POINT SUPPORT REFERENCE LOW PRESSURE, 294°K (69°F)	0.119	0.6509
POST-TEST, AIR BAG SUPPORT BASELINE, 294°K (69°F)	0.102	0.5902
AIR BAG TEST, DELTA 294°K	0.011	0.0940
PRE/POST TEST, THREE-POINT SUPPORT, DELTA, 294°K	0.019	0.1381
THREE-POINT SUPPORT, DELTA (294°K/115°K)	0.115	0.9330

3.3 TEST DESCRIPTION - FUSION BONDED MIRROR

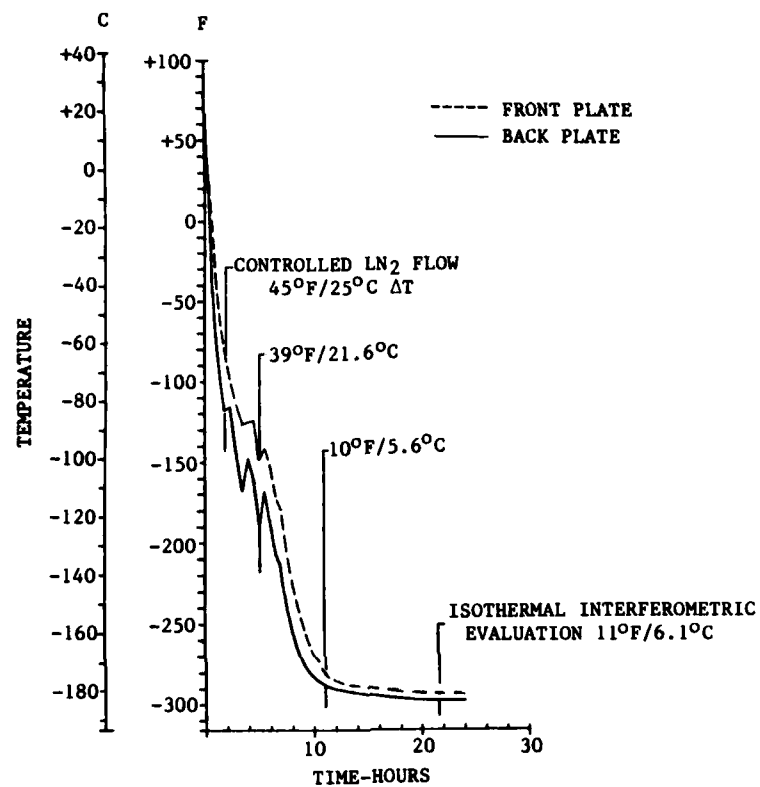
The test flow for the fusion bonded mirror is indicated in Figure 3.3-1. This mirror was subjected to a room ambient cryogenic temperature test sequence similar to that of the frit bonded mirror and the sinter bonded mirror described earlier in this report. The environmental test program for the fusion bonded mirror also included performance evaluation at elevated temperature (+200°F), evaluation after exposure to thermal cycling from -90°F to +200°F, and after ten cycles of mechanical loading at four times gravity.



305- MILLIMETER, FUSION BONDED MIRROR TEST FLOW DIAGRAM

Figure 3.3-1

Low temperature testing of this mirror was initiated in March 1982. Cryogenic isothermal conditions were achieved after 21.5 hours of LN₂ discharge with an average mirror temperature of -292°F. The average front-to-back plate edge position axial thermal gradient was 9.05°F. Maximum radial thermal gradients were 4.8°F and 2.8°F for front and back plate sensor positions, respectively. A thermal-time profile of the mirror is displayed in Figure 3.3-2. Table 3.3-1 shows the temperature values and thermal gradients for the room ambient temperature reference tests and the cryogenic test.



305-MILLIMETER FUSION BONDED MIRROR
(MIRROR THERMAL PROFILE AND AXIAL GRADIENTS)

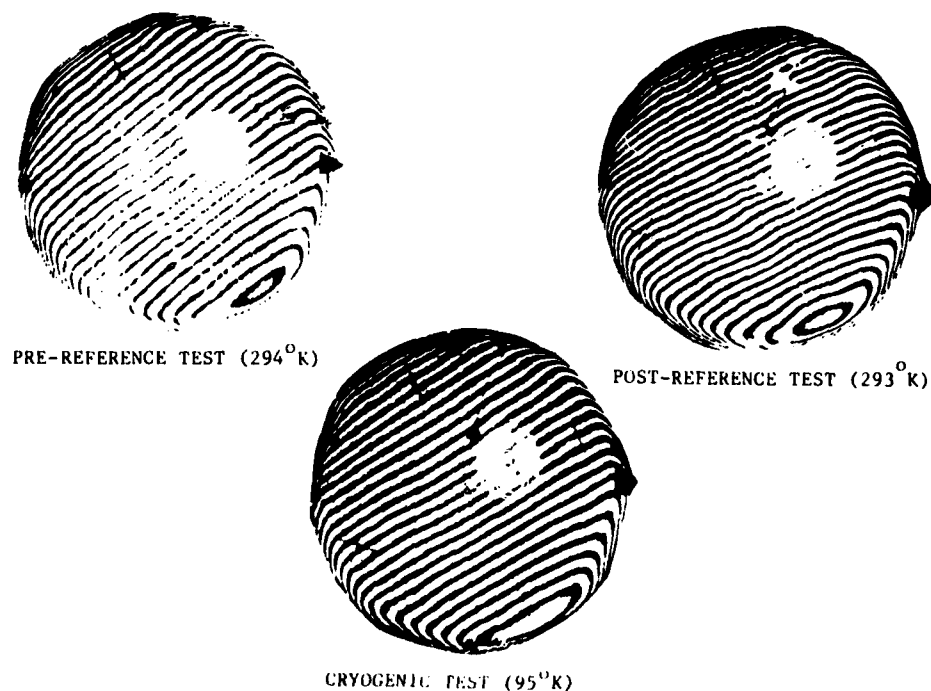
Figure 3.3-2

Table 3.3-1
TEMPERATURE VALUES - CRYOGENIC TEST SERIES
305-MILLIMETER FUSION BONDED MIRROR

		HARD-FIRED MIRROR ASSEMBLY											
		1				2				3			
INTERFEROMETRIC EVALUATION		PRE-TEST REFERENCE AMBIENT TEMPERATURE LOW PRESSURE				CRYOGENIC TEMPERATURE LOW PRESSURE				POST-TEST REFERENCE AMBIENT TEMPERATURE LOW PRESSURE			
ELAPSE TIME		-				21.5 HOURS				-			
LOCATION	TC	TEMPERATURE		ΔT		TEMPERATURE		ΔT		TEMPERATURE		ΔT	
		°F	°C	°F	°C	°F	°C	°F	°C	°F	°C	°F	°C
FRONT PLATE CENTER BACK PLATE	1	68.16	20.10	0.07	0.04	-283.7	-175.39	11.7	6.50	66.04	18.92	0.08	0.05
	2	68.09	20.01			-295.4	-181.89			65.96	18.88		
FRONT PLATE 12 O'CLOCK BACK PLATE	3	68.20	20.12	0.08	0.05	-288.5	-178.06	6.9	3.83	66.00	18.90	0.20	0.12
	4	68.12	20.07			-295.4	-181.89			65.80	18.78		
FRONT PLATE 3 O'CLOCK BACK PLATE	5	68.36	20.22	0.09	0.05	-287.2	-177.33	8.7	4.84	66.20	19.02	0.20	0.12
	6	68.17	20.10			-295.9	-182.17			66.00	18.90		
FRONT PLATE 6 O'CLOCK BACK PLATE	7	68.29	20.17	0.42	0.25	-286.6	-177.00	10.7	5.94	66.22	19.03	0.27	0.16
	8	67.87	19.92			-297.3	-182.94			65.97	18.88		
FRONT PLATE 9 O'CLOCK BACK PLATE	9	68.42	20.25	0.22	0.13	-288.3	-177.94	9.9	5.50	66.30	19.08	0.32	0.19
	10	68.20	20.12			-298.2	-183.44			65.98	18.89		
MAXIMUM RADIAL ΔT		°F		°C		°F		°C		°F		°C	
FRONT PLATE		0.26		0.16		4.8		2.67		0.26		0.16	
BACK PLATE		0.22		0.13		2.8		1.56		0.16		0.10	
AVERAGE AXIAL ΔT		°F		°C		°F		°C		°F		°C	
EDGE LOCATIONS		0.18		0.11		9.58		5.32		0.21		0.13	

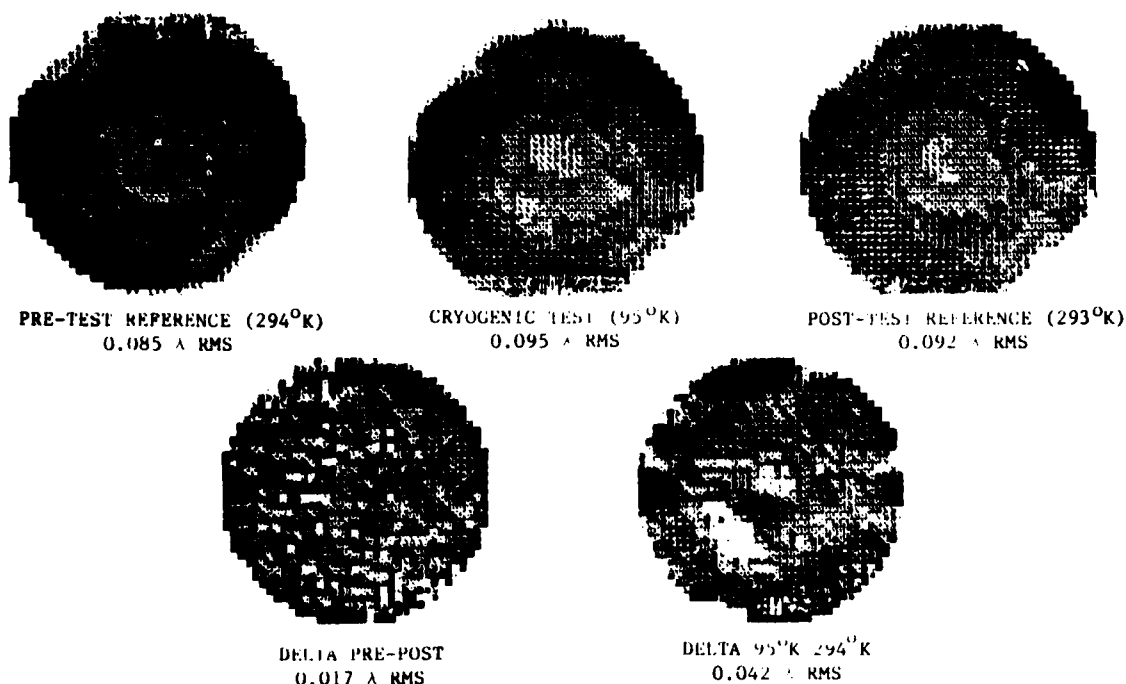
3.3.1 Test Results - Fusion Bonded Mirror

Shown in Figure 3.3.1-1 are interferograms of the fusion bonded mirror supported on three points in the cryogenic test stand before and after the thermal test cycle and at cryogenic temperature (95°K). Little change is discernable in the fusion bonded mirror at cryogenic temperature. Figure 3.3.1-2 represents the surface contour maps and difference maps for this test series. The predominant surface aberration on the three-point support is astigmatism, with the high axis running approximately from 8 o'clock to 2 o'clock positions. The pre- to post-reference test delta map appears random with a small (0.017 wave rms) difference, which is within the test error. The character of the mirror surface has changes only slightly at 95°K . The magnitude of the delta map from room temperature performance and temperature is only 0.042 wave rms. The low temperature performance and stability of the fusion bonded mirror is considered to be excellent.



FUSION BONDED MIRROR INTERFEROGRAMS

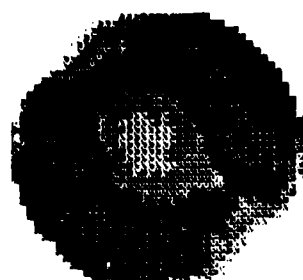
Figure 3.3.1-1



*FUSION BONDED MIRROR -
CRYOGENIC TEST EVALUATIONS
(THREE-POINT SUPPORT)*

Figure 3.3.1-2

A test at elevated temperature was also conducted to examine mirror stability at approximately 365°K (+200°F). The figure error at this temperature, shown in Figure 3.3.1-3, indicates little change from room ambient temperature. At 365°K, the surface quality was 0.101 wave rms compared to a room temperature value of 0.084 wave rms. The character of the 365°K figure and delta maps from room temperature and from 95°K are shown in Figure 3.3.1-3. The delta map from room temperature to 365°K has a value of 0.022 wave rms and appears predominantly random. The change from cryogenic to the elevated temperature is 0.048 wave rms. The delta magnitudes between the three test temperatures indicate a nearly linear variation with temperature. The small, linear reaction of this mirror with temperature changes is indicative of well-matched CTE and good structural integrity of all joints.



SURFACE ERROR AT 365°K
0.101 λ RMS



DELTA 365°K-294°K
0.022 λ RMS



DELTA 365°K-95°K
0.048 λ RMS

$\lambda = 0.6328 \mu\text{m}$

FUSION BONDED MIRROR - ELEVATED TEMPERATURE TEST

Figure 3.3.1-1

Before the final air bag test, the fusion bonded mirror was subjected to an additional six thermal cycles from 200°K to 365°K and ten cycles of an axial mechanical load equivalent to four times gravity. The purpose of these tests was to establish the bond stability under various types of loading. The value obtained for the final air bag test was 0.088 wave rms compared to 0.0856 wave rms for the initial air bag test. A point-to-point subtraction between these two tests yields a 0.010 wave rms delta which is predominately random. This result verifies the integrity and stability of this mirror over these environments. A summary of the test results for this mirror is presented in Table 3.3.1-1.

<p><i>Table 3.3.1-1</i> 305-MILLIMETER FUSION-BONDED MIRROR CRYOGENIC AND ELEVATED TEMPERATURE TEST</p>		
INTERFEROMETRIC EVALUATION	RMS VALUE (6328 Å)	P-V VALUE (6328 Å)
PRE-TEST, AIR BAG SUPPORT BASELINE, 294°K (68°F)	0.085	0.61
PRE-TEST REFERENCE, THREE-POINT SUPPORT 294°K (68°F)	0.084	0.59
CRYOGENIC TEST, THREE-POINT SUPPORT 95°K (-292°F)	0.095	0.62
HIGH TEMPERATURE, THREE-POINT SUPPORT 365°K (200°F)	0.101	0.77
POST-TEST REFERENCE, THREE-POINT SUPPORT 293°K (66°F)	0.092	0.70
POST-TEST, AIR BAG SUPPORT 294°K (70°F)	0.088	0.61
PRE/POST AIR BAG TEST, DELTA (294°K)	0.010	0.08
PRE/POST TEST, THREE-POINT SUPPORT, DELTA (294°K)	0.017	0.16

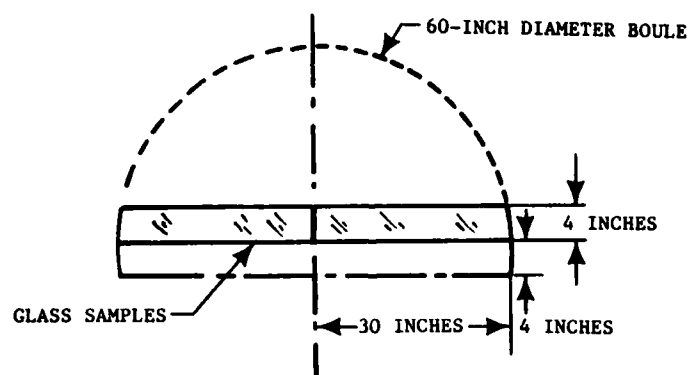
4.0 REFRACTIVE INDEX HOMOGENEITY TASK

4.1 OBJECTIVE

The objective of this task was to measure the variation of index of refraction in samples of a Code 7940 fused silica glass boule selected from the current government inventory. These data will be preserved for possible additional studies attempting to correlate variations in refractive index with coefficient of thermal expansion inhomogeneity.

4.2 GLASS SAMPLE DESCRIPTION

Two fused silica samples were cut from a 60-inch diameter, 5-inch thick boule (see Figure 4.2-1) by Corning Glass Works.



60-INCH DIAMETER, 5-INCH THICK BOULE

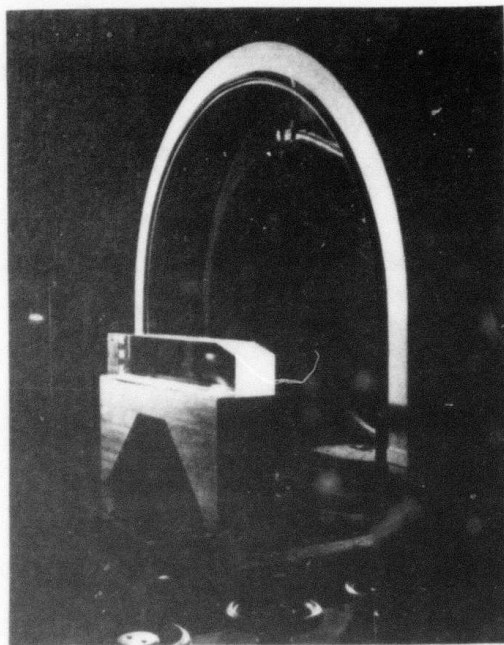
Figure 4.2-1

The samples were then shipped to Kodak, shaped, ground and polished, and interferometrically tested and evaluated. A picture of the polished glass samples in its test setup is shown in Figure 4.2-2.

4.3 TEST DESCRIPTION

The boule segments were evaluated both perpendicular to and parallel to the face of the boule, so as to measure radial and depth variation in index. This was done using a 26-inch aperture parallel beam interferometer, with the interferograms recorded on film and computer scanned and evaluated. In

order to obtain full aperture evaluation of the glass segments, it was necessary to fiducialize and take multiple subaperture photos. The resulting maps were pieced together during evaluation.



HOMOGENEITY TEST SETUP

Figure 4.2-2

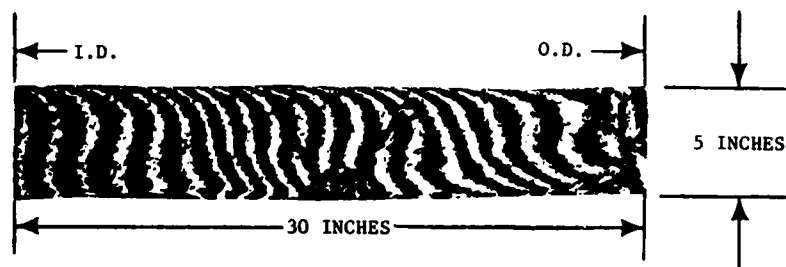
4.4 EVALUATION RESULTS

The measured values for the refractive index homogeneity are listed in Table 4.4-1.

Table 4.4-1 HOMOGENEITY DATA		
	VIEWED PERPENDICULAR TO BOULE FACE	VIEWED PARALLEL TO BOULE FACE
	P-V	P-V
SAMPLE #1	6.3×10^{-6}	4.4×10^{-6}
SAMPLE #2	5.9×10^{-6}	2.9×10^{-6}

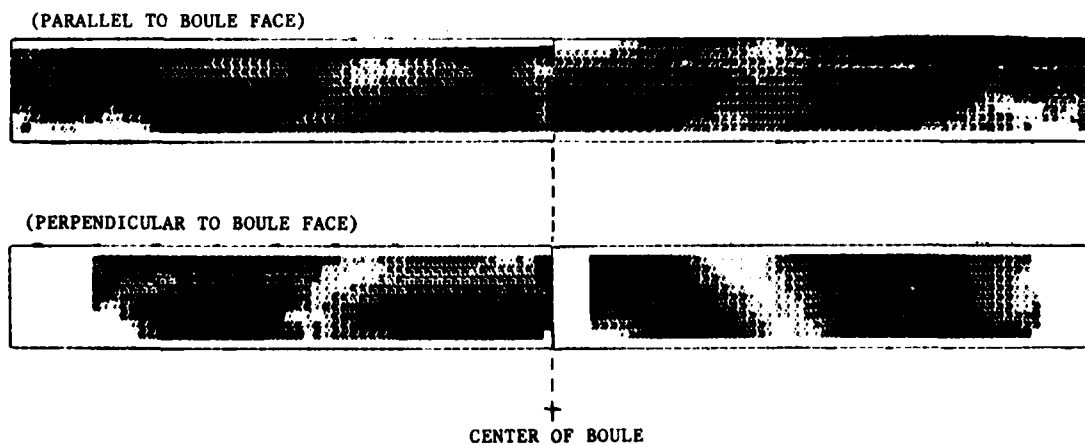
The test evaluation showed the fused silica boule to have a maximum inhomogeneity of 6.3×10^{-6} (P-V), but with a sharp index gradient existing in the upper and lower 1-inch layers of the boule (see Figure 4.4-1). Further evaluation will have to be performed to determine the impact this index gradient has on boule quality and usable material. Computer generated homogeneity maps of the glass segments are shown in Figure 4.4-2.

This data indicates excellent homogeneity of index over a 60-inch diameter.



INTERFEROGRAM OF ONE BOULE SAMPLE

Figure 4.4-1



BOULE HOMOGENEITY

Figure 4.4-2

5.0 CORNING GLASS WORKS SUBCONTRACT

5.1 SUMMARY AND CONCLUSIONS

Under a subcontract from Kodak, Corning Glass Works (CGW) completed frit bonding material studies for fused silica glass, investigated alternative cleaning methods to the standard acid etching, and nondestructive (acoustic emission) test methods for evaluating frit/glass joint integrity. Most significantly, Corning developed a fusion welding technique for ULW fused silica cores and demonstrated this process with the construction of a 300-millimeter high, 1.5-meter diameter core.

5.2 FRIT/GLASS THERMAL EXPANSION MISMATCH

The objective of this task was to determine a frit composition in which the thermal expansion mismatch between the frit and Code 7940 fused silica produced minimal strain in both the room temperature-to-cryogenic temperature (-195°C) range and in the frit setting point-to-room temperature range. The first objective is necessary to assure that the figure will not change when the mirror is exposed to thermal operating environments, which are substantially different than the environment in which the mirror was assembled and tested. The second criteria is important to assure that residual strains which may affect temporal stability are small. More than twenty compositions were evaluated for expansion mismatch and strength using frit-glass-frit (FGF) seal samples and T-samples. The T-samples were used to assess bond strength.

Development frits were coarse ground in small batches using a mortar and pestle. FGF seals were fabricated using a fast drying vehicle, then fired for 2 hours in a laboratory furnace. Based on the data from the initial sample measurements, predictions could be made as to the results for final, fine grind frit when fired with the screen oil vehicle. Results for eighteen frit compositions thus tested are given in Table 5.2-1. The setting point-to-room temperature and setting point-to-cryogenic thermal strain mismatches

are denoted by δ_R and δ_C , respectively; Δ represents the room temperature-to-cryogenic temperature strain mismatch. The first CN composition, which most closely met the goals mentioned earlier, was thus selected for further evaluation. This composition has been redesignated as FN frit. Three melts of FN frit have been made:

<u>Designation</u>	<u>Melt Size, 16</u>
FN	2
FN-1	11
FN-2	11

The firing behavior of FN and FN-1 frits was fully characterized. Although the firing behavior of the FN-2 frit was not fully characterized, enough data was collected to give confidence that the frit manufacturing process is understood and in control.

Since the CTE mismatch between frit and glass is a function of firing plateau, it is important to characterize this effect to determine the degree of furnace control that is

required during assembly of a mirror blank. Since it has been demonstrated that frit can be used to repair damaged blanks, it is also important to determine if the CTE mismatch is sensitive to multiple firings.

Table 5.2-1
FGF-DERIVED EXPANSION MISMATCH FOR
EXPERIMENTAL FRITS VERSUS CODE 7940

FRIT	GROUND STATE	δ_R , PPM	δ_C , PPM	$\Delta = \delta_C - \delta_R$, PPM
BB	C	- 87	-105	- 18
CL	C	-117	-119	- 2
CM	C	- 84	+ 13	+ 97
CN	C	- 23	- 33	- 10
CN	C	- 41	- 34	+ 7
CN	F	+ 17	+ 38	+ 21
CN	F	+ 35	+ 43	+ 8
CO	C	- 43	- 35	+ 8
CO	C	- 85	- 35	+ 50
CO	F	+ 72	+100	+ 28
CO	F	+ 34	+ 45	+ 11
CP	C	-108	- 33	+ 75
CQ	C	-109	- 29	+ 80
CR	C	- 73	+ 36	+109
CS	C	-111	-119	- 2
CT	C	- 58	+ 23	+ 81
DE	C	- 99	- 59	+ 40
DF	C	- 68	0	+ 68
DG	C	+ 7	+ 16	+ 9
DH	C	-243	-236	+ 7
DI	C	-126	- 89	+ 37
DJ	C	- 52	+ 2	+ 54
DK	C	- 86	-103	- 17
DL	C	0	+ 89	+ 89

The essential difference between the three frit compositions which were evaluated is average particle size, with FN frit at 6.0-micrometers, FN-1 at 10.1 micrometers, and FN-2 at 9.6 micrometers. Particle size has been recognized as influencing both wet-mix viscosity and refire longevity. This parameter can be controlled through proper grinding and filtering. The FN frit exhibited both an acceptable δ_R and Δ over a comfortable firing range (approximately 20°C). This frit composition also yielded acceptable thermal strains after having been refired for an additional 2 hours; however, triple firing produced high thermal strains.

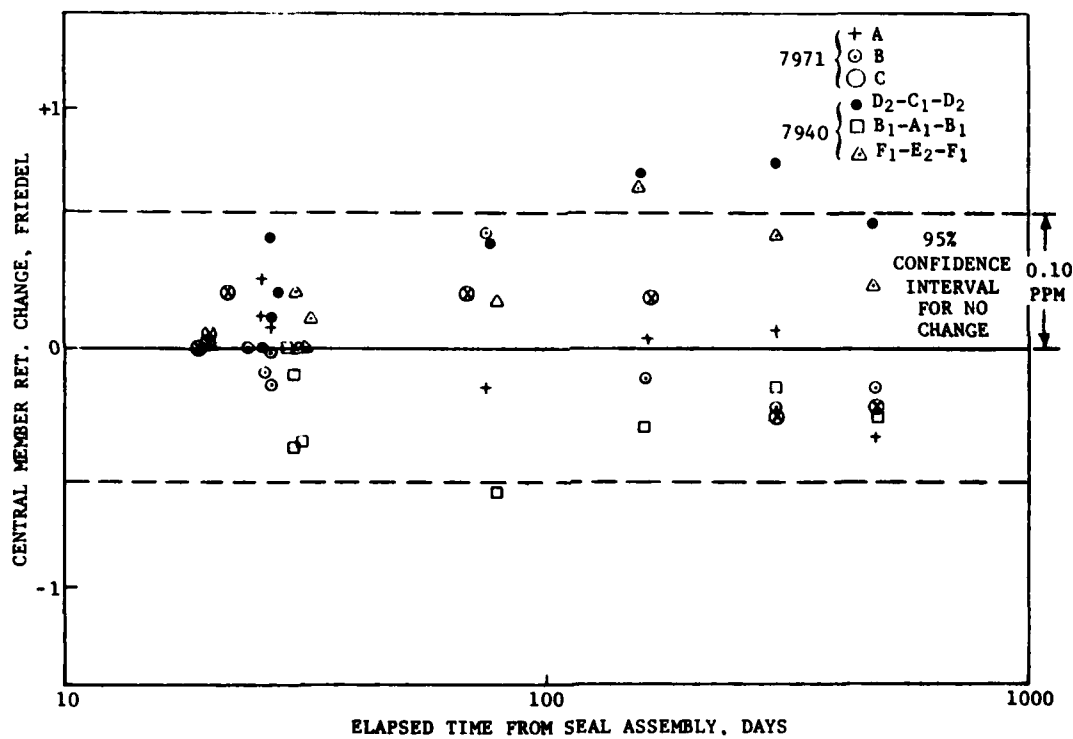
The FN-1 frit exhibited slightly larger room temperature strain than the FN frit when the seal sample was fired at 950°C for 2 hours. Additional measurements taken at firing temperatures in the vicinity of 950°C indicated that the minimum room temperature thermal strain range characteristic of frit was not in this area. Subsequent double and triple firings of this frit produced unacceptable room temperature strains. The limited data available for the FN-2 frit indicates that this frit composition is acceptable in that the thermal strain mismatch is small. It appears that the minimum area of the curve is near a firing temperature of 950°C. It is interesting to note that the thermal strain produced in the room temperature to -195°C range is low, even for the FN-1 frit which exhibited an unacceptably large room temperature strain.

In evaluating the frit compositions it is also important to assure that the joint strength is acceptable. Both for this frit system and the frit system used for ULETM Code 7971, bond strength is a function of surface preparation, frit composition, frit application, and firing temperature. To properly prepare the surface, xylene vapor is used to supplement the conventional dewaxing process, then the glass is acid etched. Experience has shown that the proper frit composition can be assessed by measuring average particle size and room temperature thermal strain. If both of these parameters are within a specified range, the frit composition is acceptable. A suitable application technique was discussed in the Phase I final report, and firing

temperature has already been discussed. The strength of twelve T-samples was measured and the 9630 ± 1119 psi results are typical of frit-bonded joints.

5.3 SEAL STABILITY

The six FGF seals described in the Final Report of Project C655010, 10 March 1980, were monitored photoelastically at selected intervals of time. The results, which are plotted as Figure 5.3-1, show no significant change over a time period of 1,000 days.



TEMPORAL STABILITY OF SIX TEST SEALS

Figure 5.3-1

In the period between 150 and 300 days, two 7940 seals experienced a small, possibly significant change; however, they have since returned to a stable condition. It is interesting and probably significant that both seals have differential thermal history purposely imposed on the seal samples for

generating some thermal expansion differences. It is, therefore, not a good idea to consider assembly of a mirror with parts having differing histories.

In summary, these seals are demonstrating that frit mirrors have excellent elastic stability which shows that frit does not microcrack and/or microyield and, in fact, maintains geometrical registry over prolonged periods of time.

5.4 RADIATION EFFECTS ON FRIT BONDS

Three fused silica and one ULETM FGF seals were exposed to strontium-yttrium radiation (primarily electrons) at a dose rate of 1 rad per second. Exposures were carried out long enough to produce dosages typical of expected operational environments. The primary measure of change is the optical retardation shift which is translated to a permanent differential length change between the frit and the glass substrate. Results are given in Table 5.4-1.

Negligible strain was induced in the Code 7940 specimen, resulting in a 1 ppm change which is within the experimental uncertainty. However, some real change occurred with the Code 7971 ULETM frit

seal. No assymetry in the stress pattern accompanied the change, leaving one to conclude that the dimensional change was primarily in the Code 7971 glass which was noticeably darkened by the radiation.

Table 5.4-1
DIFFERENTIAL STRAIN INDUCED BY RADIATION
EXPOSURE FOR FGF SEALS

GLASS	FRIT	RADIATION DOSAGE, RADS (AIR)	$\Delta\delta_R$, PPM	$\Delta\delta_c$, PPM
7940	20" MIRROR MIX	1.4×10^6	0	0
7940	20" MIRROR MIX	1.9×10^6	+ 1	0
7971	0-2	0.5×10^6	- 2	-
7971	UA*	2.1×10^6	+15	-

*Double Frit fired, 2h + 2h at 360°

5.5 CLEANING ALTERNATIVES

It is disappointing to report that the search for an alternative to our standard acid etch for surface preparation was unsuccessful. Although acid

is expensive and hazardous, we conclude that acid is essential for good frit adherence. Alternatives tried were:

- As received from plant
- Xylene dewaxing
- Sandblast
- Sandblast plus frit firing heat treatment
- Concentrated MICRO solution at room temperature
- Concentrated MICRO solution at room temperature with ultrasonic agitation
- Concentrated boiling MICRO solution

5.6 NONDESTRUCTIVE TESTING

The nondestructive evaluation of fritted glass joints in low-expansion glasses was investigated by Corning Glass Works (CGW) and the Physical Acoustics Corporation (PAC). The scope of this investigation included testing two 15-inch, frit bonded mirrors, and simple fritted glass joints for Acoustic Emission (AE) during static loading. One mirror contained visible discontinuities, while the second mirror was free of any known defects. The glass joint samples included three test specimens that were brought close to failure and began to emit acoustic emission activity.

A Physical Acoustics Corporation Model 3400, AE Analyzer/Locator system was used for mirror testing. This instrument has four independent AE channels which are used to detect the occurrence of an AE event. It also has the ability to determine the time difference of arrival of an AE event on each channel. This measurement allows the user to determine the origin or source of the AE activity through triangulation techniques.

Four PAC Model μ 100 transducers (1000 KHz resonance) were used to detect AE activity. The transducers were connected to Model 1220A preamplifiers. The system was filtered to process all signals above 150 KHz. A total system gain of 78 decibels with a detection threshold of 0.2 volt was used.

The tests involved placing a controlled compressional load on both the concave and convex sides of the mirrors. The mirrors were mounted on a $\frac{1}{4}$ -inch thick neoprene rubber pad and fixed into a Model TTCL Instron testing machine. A predetermined load of 10-20 pounds was applied to the center of each cell in the mirror through a $\frac{1}{2}$ -inch diameter loading ram at a fixed linear displacement rate. Each intersection on the honeycomb structure was assigned a sequential number. The AE transducers were located at the corners of each cell during a test.

On the "good" mirror, no activity could be detected on any cells during loading or unloading. On the mirror with intentional defects (produced by acid etching the faceplate differentially prior to frit firing), acoustic emissions were detected in cell number 102 on unloading the cell from the higher stress levels. Cell number 102 exhibited the worst frit pull-back condition and the acoustic emissions can be correlated through visual assessment.

It is possible that rubbing or frictional sources were generated in areas of visible frit discontinuities. However, there did not appear to be any propagation of the discontinuity.

In the second part of this investigation, acoustic emission of three-single frit joint samples were loaded in an attempt to characterize emissions as the joints were loaded to failure.

A reoccurring factor found in these tests and others performed previously was that at the onset of frit failure, there is a substantial release of high energy events. These events are of high amplitude, i.e., greater than 90 decibels. This response represents a classic type of failure mechanism relating to the initiation of a crack and is followed by events much lower in amplitude and energy attributed to propagation of a crack.

The results gathered from this technique are encouraging and should be pursued as a nondestructive test method for mirrors.

5.7 FRIT/GLASS INTERFACIAL CHARACTERISTICS

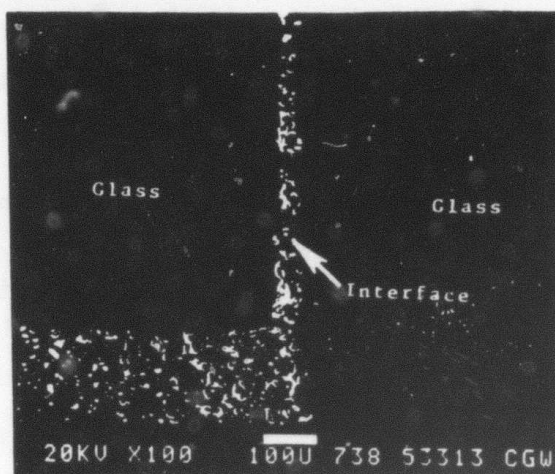
5.7.1 Chemical

It has been observed during photoelastic examination of FGF seals that a thin layer of the substrate glass, both Codes 7940 and 7971, exhibits differing optical retardation bordering the frit/glass interface (this has been thought of as a diffusion layer); we therefore, submitted some T-specimen strength joints representing FN-1/7940 and UA/7971 for electron microprobe analysis. Results show that both systems exhibit a diffusion layer about 8 microns in width.

This phenomenon is regarded as evidence of bonding activity and has no obvious negative overtones. The magnitude of optical retardation difference in this zone is about 12 nanometers per centimeter, equivalent to a stress of approximately 50 psi.

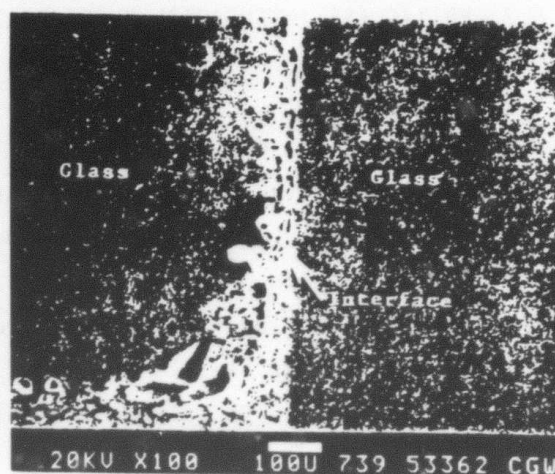
5.7.2 Physical

Counterparts of the specimens submitted to electron microprobe were investigated by the scanning electron microscope for detailed physical characteristics. Resulting micrographs are shown in Figures 5.7.2-1 and 5.7.2-2. Although aware that these frits tend to be porous, these micrographs give a good view of the nature and distribution of the voids.



MICROGRAPH CROSS SECTION CODE 7940
FUSED SILICA/FN-1 FRIT
(MAGNIFICATION: 100X)

Figure 5.7.2-1



MICROGRAPH CROSS SECTION CODE 7971
FUSED SILICA/UA FRIT
(MAGNIFICATION: 100X)

Figure 5.7.2-2

5.8 L-SPECIMEN STRENGTH

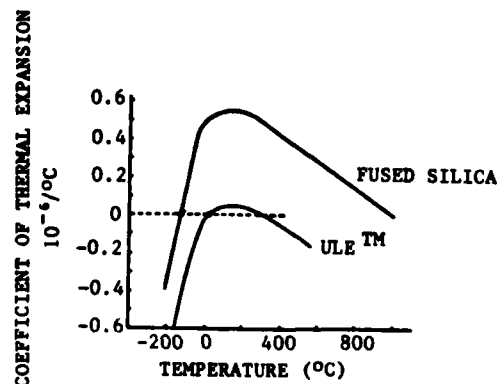
Thirty-two L-specimens were assembled per CGW Drawing No. 20576C and tested in accordance to CGW Procedure No. 20577L. Acid surface preparation was Corning's standard acid mix with a 45 minute immersion for all glass parts. Frit FN-1 was used and given a 2 hour firing at 955°C.

Strength testing results show that all specimens failed in the 1690 to 5223 psi range, averaging 3905 psi. It should be noted that these are simple bending stresses and do not account for any stress concentrations effects produced by the fillet geometry. All failures originated from the rough saw-cut side of the strut, with no failures attributable to frit or frit-bond failure. This data suggested that grinding both strut surfaces would be a strength-improving procedure.

5.9 1.5-METER ULW FUSED SILICA CORE

5.9.1 Background and Summary

This task was initiated to develop the manufacturing capability for large fused silica ultra lightweight mirror cores. This capability was demonstrated by fabricating a 1.5-meter diameter core. Initial development in 1981 showed that the 12-inch high, fused silica cells in the core could not be sealed using the standard ULETM cold-core process. This was due in part to the higher expansivity of fused silica during cooling from fusion temperatures (see Figure 5.9.1-1). Modifications and refinements needed to be made to the manufacturing equipment so as to control the thermal gradients in the core and to effect an annealing of the core prior to cooling to room temperature. Also repair techniques and sealing operating parameters needed to be defined. Fusion welding of 12-inch high, fused silica cells was demonstrated first in single cell units, then in a 15-cell core section, and finally in the 1.5-meter core. Corning experienced the normal core fabrication problems with the 1.5-meter core resulting in a small number of documented fractures. The final inspection, made on 22 July 1983, indicated the core to be of good quality and acceptable for use in a fused silica ultra lightweight mirror.

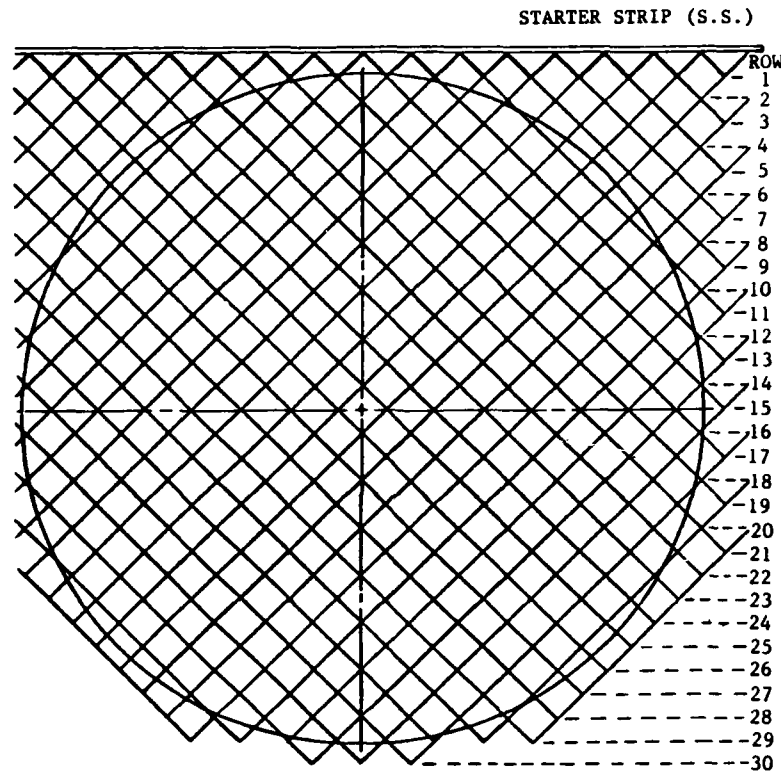


THERMAL SENSITIVITY - FUSED SILICA AND ULETM

Figure 5.9.1-1

5.9.2 Design Description

The 1.5-meter core is of ultra lightweight design, with a weight reduction of 95 percent from that of a solid. The core is 12 inches thick, with 3-inch square cells, 0.200-inch posts, and 0.075-inch thick struts (see Figure 5.9.2-1).

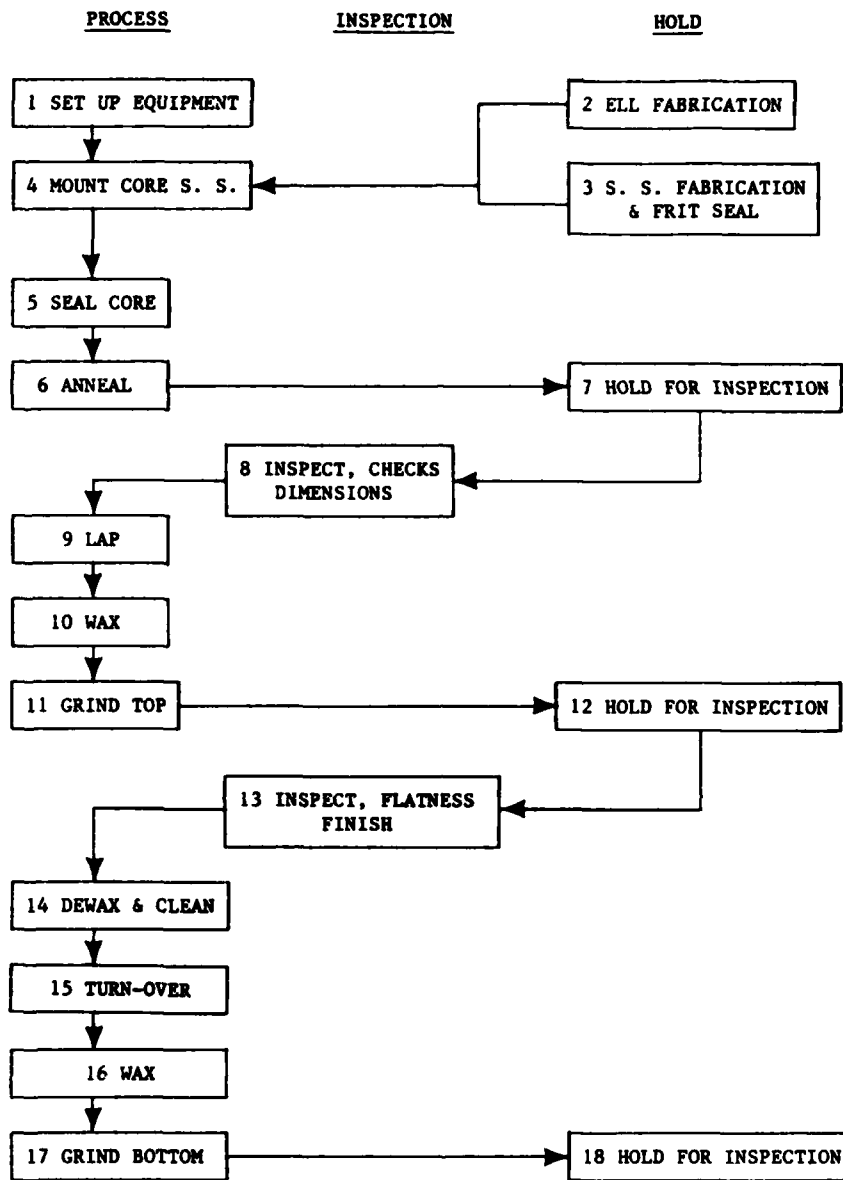


1.5-METER CORE LAYOUT

Figure 5.9.2-1

5.9.3 Fabrication Process

The fabrication process used for the 1.5-meter core is listed in Figure 5.9.3-1. While the process flow is basically the same as that used for ULETM glass, special requirements to control thermal gradients during fusing, and an in situ annealing to prevent stress buildups are required.



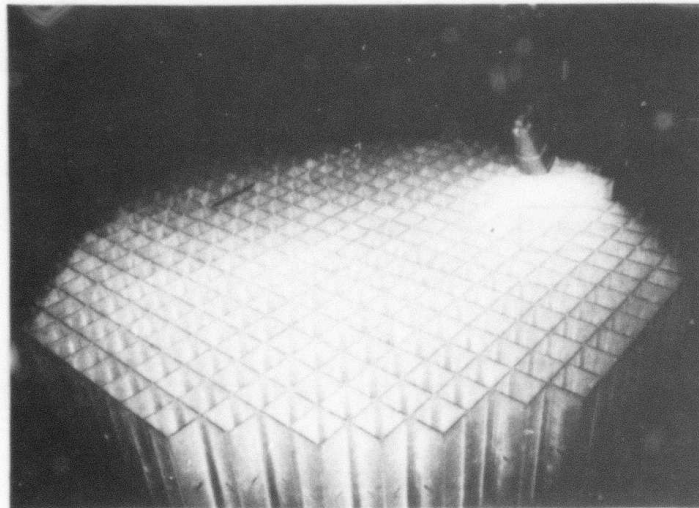
CORE FABRICATION DIAGRAM

Figure 5.9.3-1

The glass selection for core construction was deliberately, tightly controlled to minimize flaws which might impart stress concentration.

5.9.4 Results

Corning Glass Works successfully manufactured the 1.5-meter (Code 7940) fused silica core. It has been inspected, accepted, and packaged in a sturdy shipping/storage container. This ULW fused silica core is deep or thick enough to produce an ultra lightweight frit bonded mirror 1.5 meters in diameter with only half the density of the Space Telescope primary mirror. Although problems were encountered during fabrication of the core, an understanding of and solutions to these problems were demonstrated. As a result of this endeavor, the state-of-the-art in fusion core making has been advanced, and large fused silica ultra lightweight mirrors for cryogenic applications are now possible. A picture of the 1.5-meter core is shown in Figure 5.9.4-1.



1.5-METER ULTRA LIGHTWEIGHT MIRROR CORE

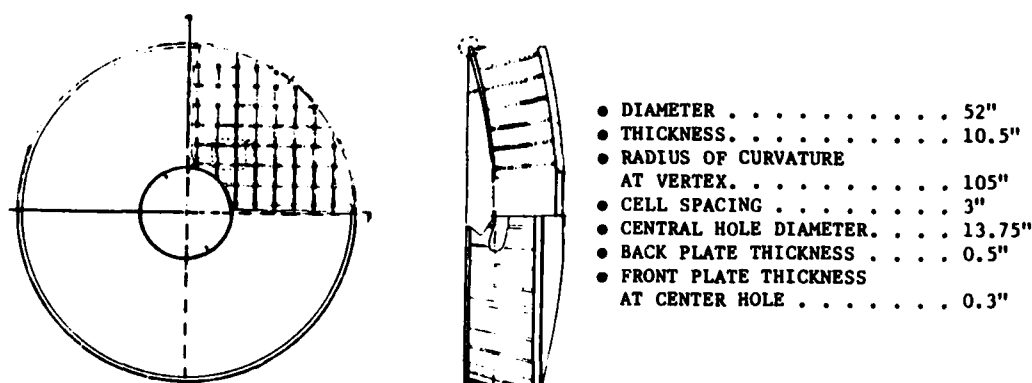
Figure 5.9.4-1

6.0 ASPHERIC MIRROR FABRICATION DEMONSTRATION

6.1 OBJECTIVE AND CONCLUSIONS

The objective of the demonstration task was to develop and demonstrate optical manufacturing and metrology techniques necessary for producing steep, highly aspheric mirrors. The asphere selected for demonstration has an aspheric departure an order of magnitude greater than that of the NASA Space Telescope primary mirror.

The demonstration was structured to address key fabrication and metrology issues within the cost and schedule constraints of the Phase IIA contract. The mirror blank used in the demonstration was an existing, lightweight, ULETM blank purchased from Corning Glass Works. Corning was contracted to resag the blank to a 105-inch radius of curvature. For ease of testing, the optical form selected was a 1.2-meter diameter, $f/0.8$ parabola, with a surface figure goal of 0.10 wave (rms) at 0.6328 micrometer. Figure 6.1-1 describes the demonstration mirror configuration.



DEMONSTRATION MIRROR CONFIGURATION

Figure 6.1-1

The following results and conclusions can be drawn from this task:

- A steep asphere with aspheric departure an order of magnitude greater than that of the NASA Space Telescope primary mirror (current state-of-the-

art in demonstrated optical fabrication capability) was aspherized and polished to a figure error of 14 waves P-V ($\lambda = 0.6328 \mu\text{m}$).

- The mechanical gaging technique used to track the surface profile during the initial (rough) aspherizing process, while adequate, was tedious and cumbersome. A more efficient profiling technique should be pursued and developed to optimize aspherizing optical forms of radical aspheric departure.

- The technology to design, construct, and condition full-size polishing laps with the global flexibility and local compliance required to accommodate this radical aspheric departure was demonstrated.

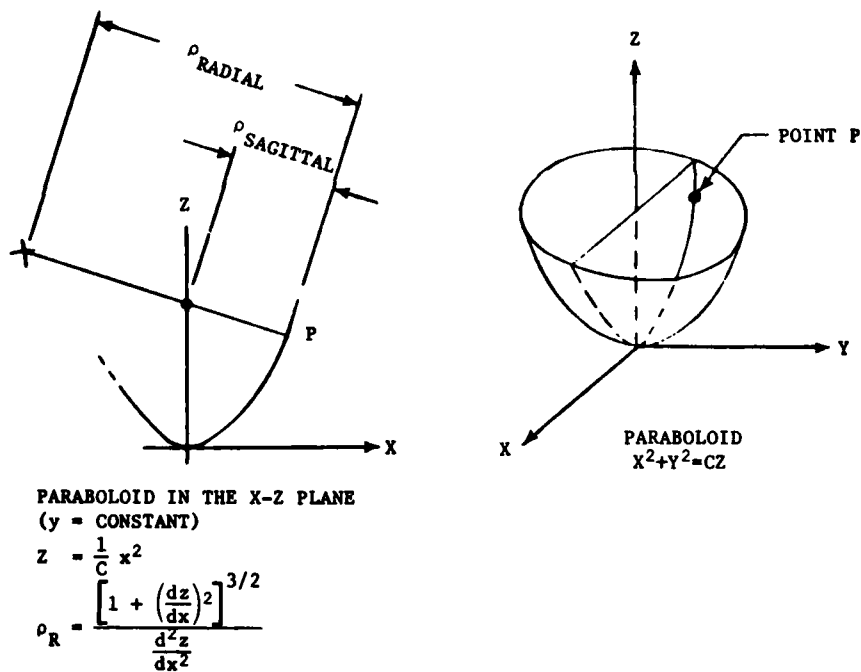
- Convergence demonstrated to date, indicates that this polishing technique should be capable of making significant improvement in the figure quality of this steep asphere.

6.2 MIRROR DESCRIPTION

The demonstrated ability to fabricate a fast/deep asphere is a key issue. While the testing difficulty was minimized by selecting a parabola, the asphericity was purposely chosen to be rather severe. Table 6.2-1 summarizes and compares by different figures of merit some anticipated aspheric forms based on today's knowledge. The Space Telescope Primary Mirror represents the current state-of-the-art capability. Note the increased degree of difficulty between system A and the Space Telescope. The demonstration mirror form was selected to specifically address the $f/0.8$ focal ratio, the departure from the vertex sphere, and the sag delta over a 1-inch diameter tool. The demonstration asphere has a departure from the vertex sphere of 3870 waves, a departure from the minimum removal sphere of 920 waves, and a maximum slope of 12,500 waves/inch ($\lambda = 0.6328 \mu\text{m}$). The delta sag over a 1-inch diameter gives some indication of the degree of difficulty in achieving a good polishing tool fit on the mirror surface. Figure 6.2-1 shows the radial and sagittal radii of curvature.

Table 6.2-1
OPTICAL FORM SUMMARY

CHARACTERISTICS	SYSTEM A	SYSTEM B	SYSTEM C	SPACE TELESCOPE	DEMONSTRATION MIRROR
DIAMETER (METERS)	1.5	4.0	1.2	2.4	1.2
f-NUMBER	0.8	1.25	1.28	2.3	0.8
FORM	ELLIPSE	PARABOLA	ELLIPSE	HYPERBOLA	PARABOLA
DEPARTURE FROM VERTEX SPHERE (MILS)	105	80	22	8	96
DEPARTURE FOR MINIMUM REMOVAL SPHERE (MILS)	26	20	6	2	23
DELTA SAG OVER 1-INCH DIAMETER TOOL (WAVES $\lambda = 6328 \text{ \AA}$)	5	0.5	1.5	0.2	6



ASPHERE RADIAL AND SAGITTAL RADII OF CURVATURE

Figure 6.2-1

The delta sag is as follows:

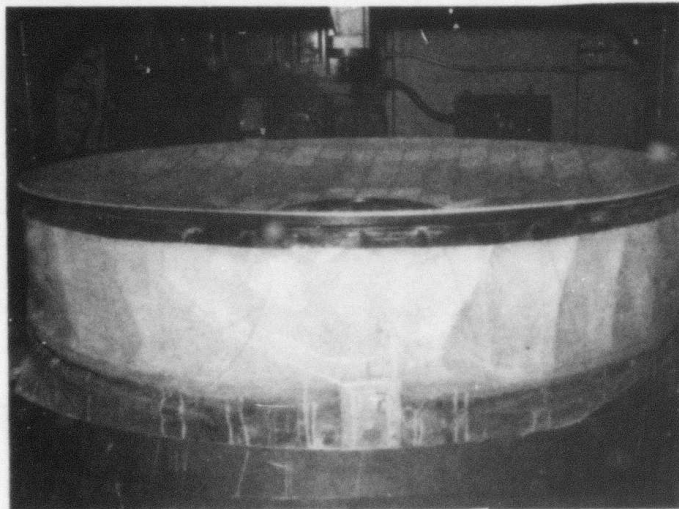
$$\Delta \text{ sag} = \frac{y_t^2}{2R_s} - \frac{y_t}{2R_r} = \frac{\alpha^2 D}{4(16f^2 + 1)^{3/2}}$$

α = Ratio of tool diameter to mirror diameter

D = Mirror diameter (inch)

f = Mirror f-number

The effect of this delta meant that Kodak must extend the current flexible lap approach to accommodate the increased surface departure, and must extend or develop metrology compatible with the increased asphericity. Figure 6.2-2 is a picture of the demonstration asphere in the polishing cycle.



DEMONSTRATION ASPHERE

Figure 6.2-2

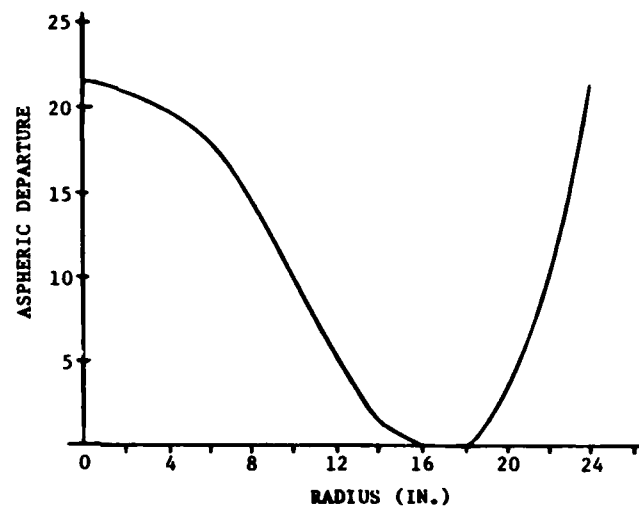
6.3 MIRROR BLANK PREPARATION

As a cost and schedule expedient, Corning Glass Works was contracted to thermally slump an existing ULETM, 1.4-meter diameter, lightweight blank to an f/0.9 form. Figure 6.3-1 is a picture of the slumped mirror blank as received at Kodak. As expected, thermal slumping to this f-number greatly distorted the blank. Extensive shaping and grinding were required to prepare

6.4 FABRICATION AND TEST PROGRAM

6.4.1 Process and Test Description

Subsequent to shaping and fine grinding the critical task of aspherizing began. Figure 6.4.1-1 is a plot of the aspheric departure from the minimum removal sphere cut into the faceplate. The maximum departure, or differential material removal that had to be achieved during the aspherizing and figuring operations was 0.023 inch; about an order of magnitude greater than that of the space telescope primary mirror.



ASPHERIC DEPARTURE FROM
MINIMUM REMOVAL SPHERE

Figure 6.4.1-1

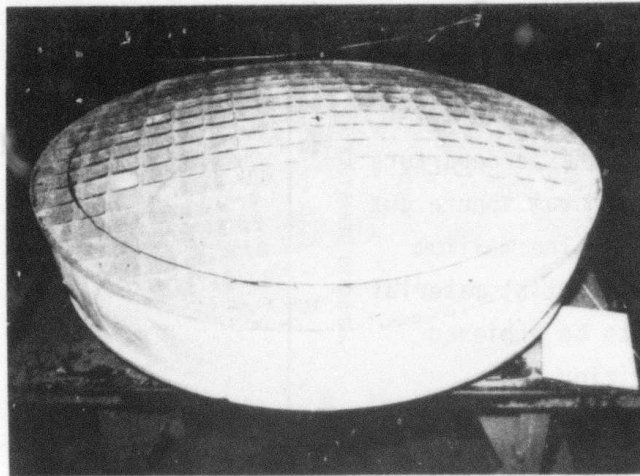
The degree of departure complicates tool design and surface profile measurements. The profile measurement approach used must have a capture range large enough to accommodate the steep aspheric departure (0.023 inch) while maintaining high accuracy (50×10^{-6} inch desired). A two-step approach was followed:

- (1) Mechanical gaging - rough aspherizing
- (2) CO₂ interferometry (10.6 micrometers) - aspherizing and polishing

Mechanical gaging technique was used initially, and then yielded to CO₂ interferometry to track the surface profile.

The mechanical gaging technique employed is known at Kodak as profilometry. Profilometry uses a glass master (profilometer master) as a reference in which a minimum removal sphere has been cut, and a special gage known as a profilometer. The profilometer includes a rigid, stable truss and a network

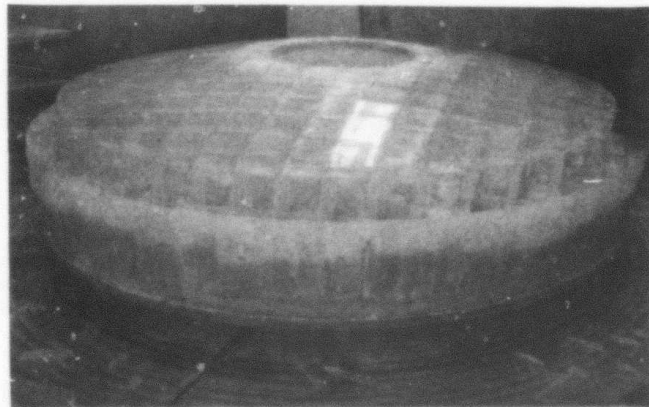
the blank for polishing. The blank was shaped using conventional shop techniques. Rounding, beveling, center hole core drilling, and generation of the minimum removal sphere were done on a Blanchard grinder modified to accommodate the steepness of this blank.



SLUMPED MIRROR BLANK

Figure 6.3-1

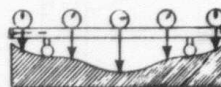
The blank was cut down to a 1.3-meter diameter aperture. A 0.35-meter diameter center hole was plunged-cut into the blank and front and backplate radii of 1.998 and 2.667 meters, respectively, were generated. The inner and outer diameters of the front and backplates were reference-rounded and beveled. Figure 6.3-2 is a picture of the blank (back surface up) during the extensive shaping process.



MIRROR BLANK IN-PROCESS SHAPING

Figure 6.3-2

of high accuracy mechanical gages. In use, the profilometer is set or "zeroed" on the profilometer master and then transferred to the optic in-work to track its profile. Figure 6.4.1-2 is a schematic of a profilometer.



PROFILOMETER SCHEMATIC

Figure 6.4.1-2

Figure 6.4.1-3 is a picture of a profilometer in use at Kodak on the NASA Space Telescope primary mirror.

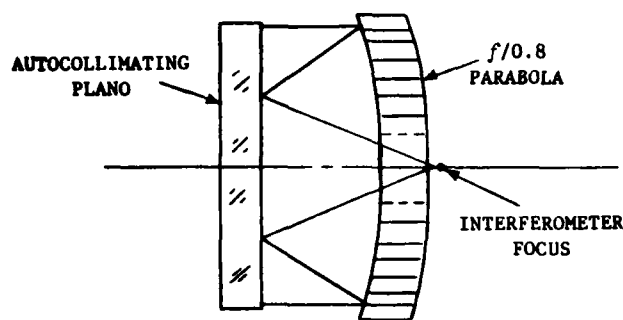


PROFILOMETRY, SPACE TELESCOPE PRIMARY MIRROR

Figure 6.4.1-3

For the demonstration asphere, 12-inch and a 24-inch long profilometers were used in an overlapping fashion, to track the surface profile.

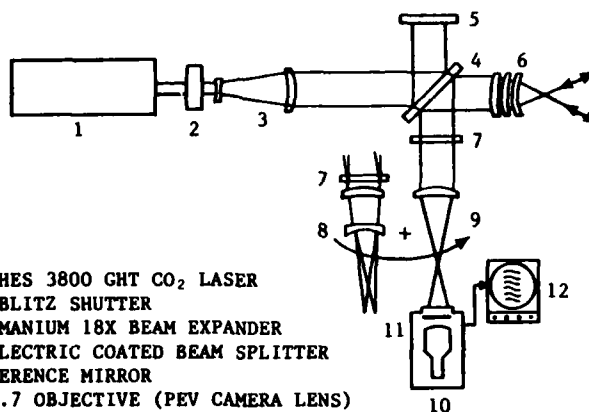
Following rough aspherizing on a loose abrasive tub grinder and profile tracking with profilometry (0.002-inch residual), CO₂ interferometry (10.6 micrometers) was used to complete the remaining process effort. Wavefront tests were made by using an autocollimating plano to produce a perfect null test of the $f/0.8$ parabola. A schematic of the test setup appears in Figure 6.4.1-4.



WAVEFRONT TEST SETUP

Figure 6.4.1-4

Note that this configuration requires two reflections from the demonstration asphere, which results in a test wavefront error of four times the surface error of the primary. CO₂ interferometry increases the error capture range over standard HeNe interferometry by a factor of 16.75, the ratio of the two wavelengths. A diagram of the CO₂ interferometer/display monitor appears in Figure 6.4.1-5. The principal components are listed on the figure. The video image on the display monitor can be photographed for subsequent scanning by an off-line, interferometric data evaluation system.



- 1) HUGHES 3800 GHT CO₂ LASER
- 2) UNIBLITZ SHUTTER
- 3) GERMANIUM 18X BEAM EXPANDER
- 4) DIELECTRIC COATED BEAM SPLITTER
- 5) REFERENCE MIRROR
- 6) f/0.7 OBJECTIVE (PEV CAMERA LENS)
- 7) NEUTRAL DENSITY FILTER
- 8) FRINGE ACQUISITION LENS ASSEMBLY
- 9) FRINGE DISPLAY LENS ASSEMBLY
- 10) PYROELECTRIC VIDICON CAMERA
- 11) CAMERA'S INTEGRAL CHOPPER
- 12) DISPLAY MONITOR

CO₂ INTERFEROMETER/DISPLAY MONITOR

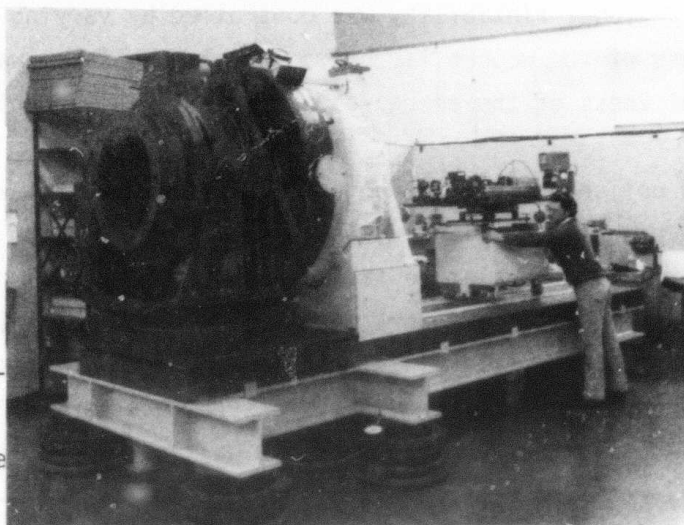
Figure 6.4.1-5

Figure 6.4.1-6 is a picture of the wavefront test setup. The demonstration asphere was supported on edge in a V-block support. (An assumption implicit in the approach is that variability in the on-edge support is small relative to the figure error of the asphere.) The test setup includes a stiff test bed mounted on vibration isolating air springs, a 1.2-meter diameter

autocollimating test flat, and an on-edge mount. The asphere is supported by the on-edge V-block.

Subsequent to aspherizing, polishing was started on a Kodak-developed programmable polishing machine using full-size polishing laps. These full-size polishing laps were designed with global flexibility and local compliance compatible with the steep aspheric profile. The laps were constructed from lami-

nated plywood covered with energy-absorbing foam rubber which was then covered with optical pitch. Figure 6.4.1-7 is a picture of a typical full-size flexible lap designed to correct symmetric figure errors.



WAVEFRONT TEST SETUP

Figure 6.4.1-6

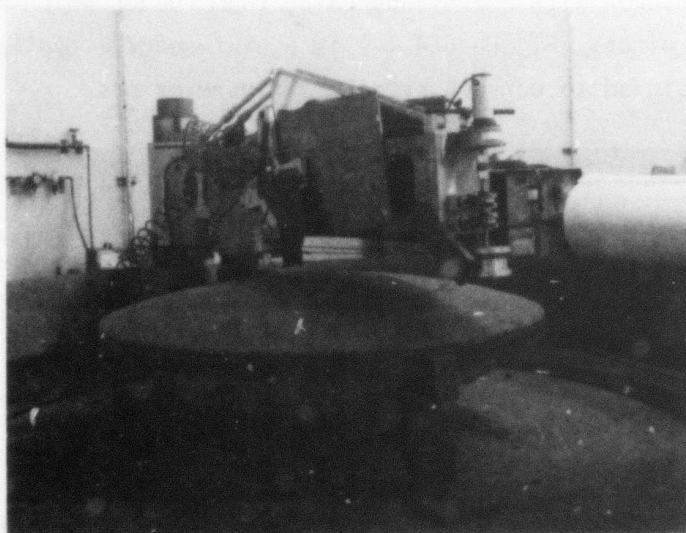


FLEXIBLE SYMMETRIC LAP

Figure 6.4.1-7

Lap global flexibility was controlled by varying the cross section or thickness of the wooden lap body. Local compliance was controlled by varying the thickness of the energy-absorbing material and pitch layer.

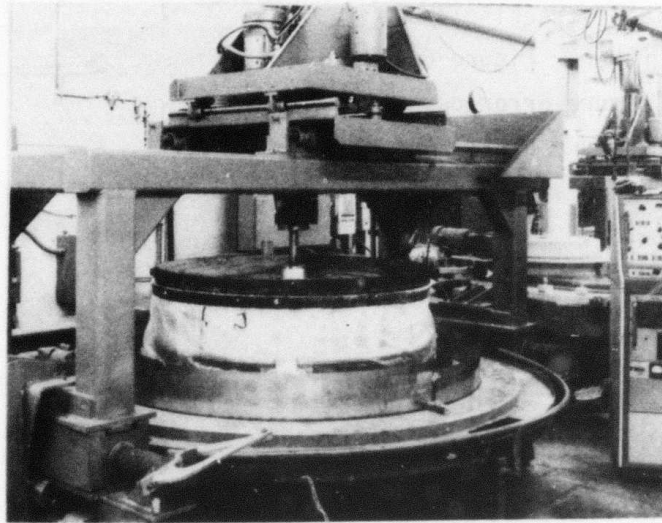
In polishing with conventional laps, a good fit with the optic can be achieved by pressing the lap out on the optic. The pitch layer is allowed to flow until a good relative fit, with no differential pressure, is achieved. This technique will not work with flexible laps employed here, because the compliant layer will "store" energy and isolated local high spots will not support the localized high pressure necessary to promote pitch flow. For these flexible laps, a good fit was achieved by first contouring the pitch layer to the approximate aspheric cross section using a cam-driven pitch cutter, then conditioning (running) the lap on the fast asphere. A good optic-lap fit could be typically achieved with a run time of 15 minutes or less. A picture of the pitch cutter appears in Figure 6.4.1-8.



PITCH CUTTER

Figure 6.4.1-8

Figure 6.4.1-9 shows the demonstration asphere in the polishing operation. This polishing machine can be programmed to drive polishing laps in both x and y directions, in synchronous rotation and variable out-of-sync rates from 0.1 rpm to 10 rpm relative to the optic.



DEMONSTRATION ASPHERE IN POLISH

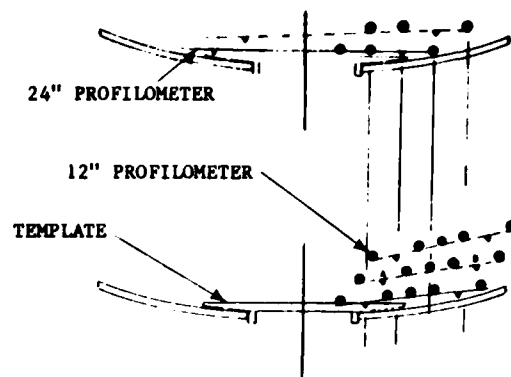
Figure 6.4.1-9

6.4.2 Figure Error Results

Profilometry was used to track the aspheric profile during the initial aspherizing operation. The steep slope of the demonstration asphere is such that registration errors associated with location of the profilometer on the asphere translates almost directly (one-to-one) into height (profile) errors.

Figure 6.4.2-1 is a schematic of the profilometry setup using the 12-inch and 24-inch long profilometers. A center hole template was used to register the location of the profilometers and minimize this error source.

Profilometry measurements were used to guide the aspherizing process to about the 0.002-inch (80 waves at 0.6328 micrometer) figure error level. The profiling technique and equipment available were incapable of reliably tracking the mirror profile further. Figure 6.4.2-2 is a plot of the figure error departure from the desired asphere at the end of the profilometry cycle and the transfer to CO₂ interferometry.



PROFILOMETER MEASUREMENTS

Figure 6.4.2-1

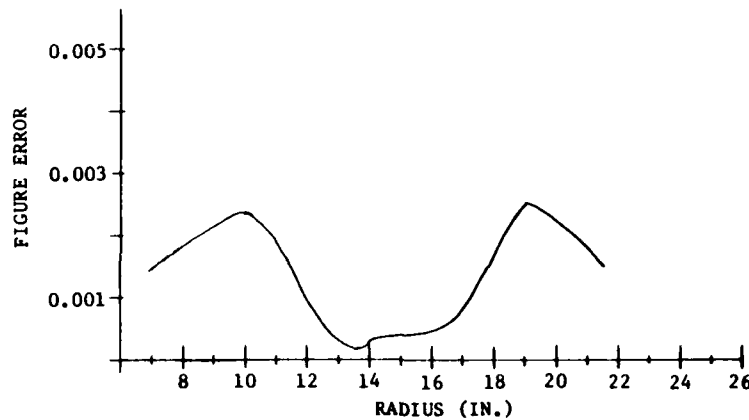


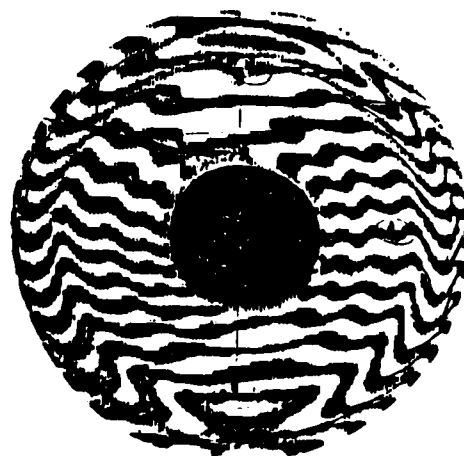
FIGURE ERROR DEPARTURE - ROUGH ASPHERIZING

Figure 6.4.2-2

Final aspherizing and initial polishing were guided by CO₂ wavelength (10.6 micrometers) interferometry. This testing was complicated by the double-pass nature of the test setup which scaled figure error up by a factor of four and reduced contrast to the extent that a spray silver coating was needed on the asphere to acquire interferometry.

At the start of CO₂ interferometry, the dominant figure error was zonal or symmetric in nature. The zonal error (exaggerated by the double-pass nature

of the test setup) exhibited fast (steeply-sloped) transition zones. These fast slopes could not be properly scanned and evaluated by traditional computer data reduction equipment. Therefore, estimates of figure error were initially made through manual data reduction methods and radial sector testing at CO_2 wavelength. This technique is sensitive only to the symmetric or zonal errors. Accordingly, processing was limited only to symmetric error correction. The aspherizing effort was halted when the estimated figure error had improved to 0.0005 inch (20 waves at 6328 \AA) and flexible laps were substituted for the relatively stiff tile grinding laps. Polishing operations employed full size, flexible laps and addressed the zonal, or symmetric error. Symmetric polishing improved the figure error to an estimated 14-wave ($\lambda = 0.6328 \text{ micrometers}$) surface error when the contract funding budget for this task was reached. Figure 6.4.2-3 is a picture of a final CO_2 interferogram. The dominant error is zonal in nature.



WAVEFRONT ERROR, CO_2 INTERFEROMETRY

Figure 6.4.2-3

During this demonstration, the figure error was improved from 920 waves (the departure from the minimum removal sphere) to 14 waves. Figure 6.4.2-4 summarizes the figure error measurement techniques and results used to guide demonstration asphere processing.

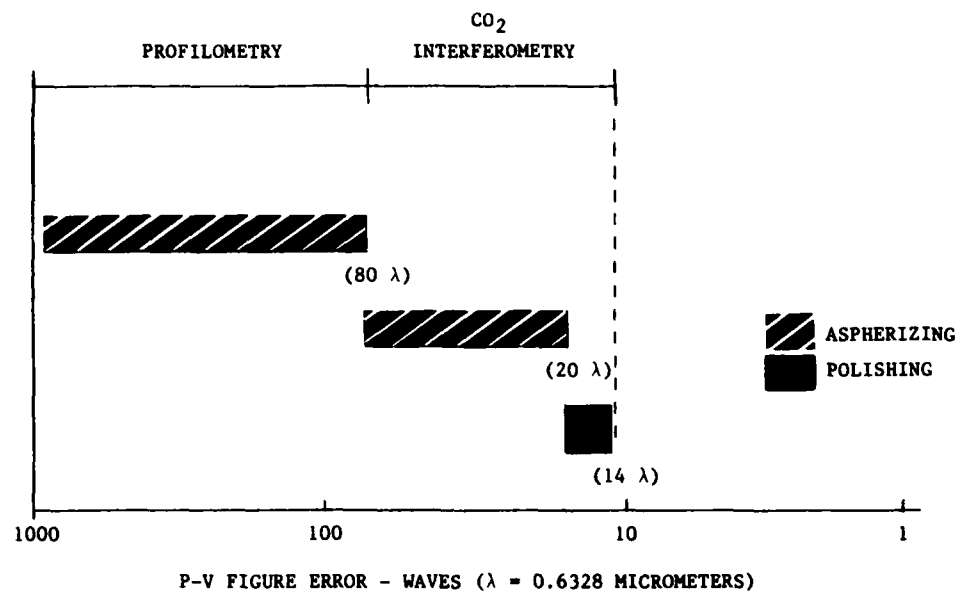


FIGURE ERROR MEASUREMENT TECHNIQUES AND RESULTS

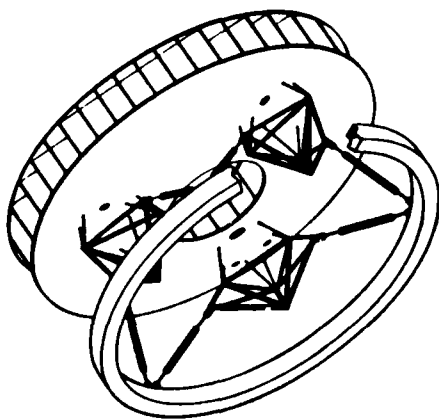
Figure 6.4.2-4

7.0 CRYOGENIC MIRROR MOUNTING

7.1 OBJECTIVE AND CONCLUSIONS

The objective of this task was to identify a mounting approach for an ultra lightweight mirror for use at cryogenic temperatures. The mounts and mirror must survive a Space Shuttle launch and landing, and must operate in a cryogenic space environment. This means that the mirror mount structure must be rigid enough to maintain the dynamic response of the mirror and, at the same time, must not significantly deform the surface of the mirror through a mismatch in the thermal contraction of the mirror and mount structure. Major design considerations also include the physical means of attaching the mount structure to the mirror and thermal stability control of the motion of the mirror along the optical axis.

This study concentrated on analyzing the influence of mirror mount material and geometry on these principle design considerations. The mount structure (Figure 7.0-1) consists of a support ring, which lies below the mirror, and six legs, which rise from the ring and connect to three intermediate structures. These intermediate structures, called "kinematic cells", are assumed to be completely rigid for the purpose of preliminary mount geometrical considerations. Because of this assumption, the particular geometry of the kinematic cells need not be included in initial design configuration evaluation.



CRYOGENIC MIRROR MOUNT CONCEPT

Figure 7.0-1

A mirror mount concept, was developed which is considered to be low risk, and can be applied to ultra lightweight or existing lightweight mirror designs. Detailed engineering of this concept was not performed.

7.2 MATERIAL AND CONFIGURATION EVALUATION

7.2.1 Mirror Geometry and Design Conditions

The dimensions and physical properties of the fused silica mirror which was used in the mirror mount study are given in Table 7.2.1-1. The temperature excursion of the mirror was taken to be 200⁰K, whereas assembly and Shuttle flight loading is assumed to occur at 20⁰C.

Table 7.2.1-1 MIRROR PARAMETERS	
CHARACTERISTIC	PARAMETER
OUTSIDE DIAMETER	55.62 IN.
INSIDE DIAMETER	16.04 IN.
MIRROR RADIUS OF CURVATURE	97.082 IN.
BACK PLATE RADIUS OF CURVATURE	105.082 IN.
FRONT PLATE THICKNESS	0.30 IN.
BACK PLATE THICKNESS	0.30 IN.
OVERALL THICKNESS	8.00 IN.
CORE SPACING	3.00 IN.
CORE PLATE THICKNESS	0.075 IN.
CENTER POST EDGE LENGTH	0.15 IN.
DENSITY	0.08 LB/IN. ³
WEIGHT	176.56 LBS
MODULUS OF RUPTURE (20 ⁰ C)	7190 LB/IN. ²
ELASTIC MODULUS (20 ⁰ C)	10.60x10 ⁶ LB/IN. ²
POISSON'S RATIO (20 ⁰ C)	0.17
ELASTIC MODULUS (@ LOW TEMP.)	9.92x10 ⁶ LB/IN. ²
POISSON'S RATIO (@ LOW TEMP.)	0.149

The center of gravity is located 1.883 inches back from the front surface of the mirror. It was assumed in the analysis that both the front and back surfaces of the mirror are spherical sections with a common center of curvature.

7.2.2 Effect of Mount Materials on Induced RMS Figure Error

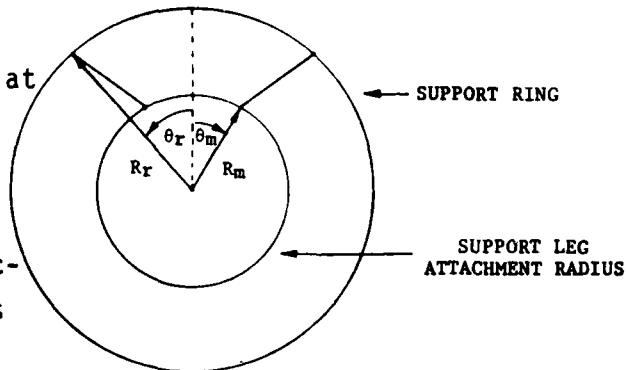
The primary concern in the mirror mount study was maintaining a low value for the mount-induced figure error over the temperature excursion of 200°K . The design goal is for an rms figure error of no more than 0.005 wave at a wavelength of 4 micrometers. The analysis performed at Kodak examined the possibility of using aluminum and/or titanium in the main support structure, both of which were chosen because of their light weight. Aluminum, which is relatively low cost, has good cryogenic properties, whereas titanium is stronger and has a significantly lower thermal coefficient of expansion. The kinematic cell and the small attachment flexures were assumed to be made of Invar in an effort to better match the mirror material.

In order to perform the analysis, it was necessary to know how the mirror responds to unit forces and moments applied at three points, equally spaced about the center of the mirror at a given radius. This was determined by constructing a NASTRAN model of the mirror. The mirror was modeled as an equivalent curved thin plate with the membrane bending and transverse shear stiffness as independently specified. The stiffness values that were used allowed the true mirror cross section to be accurately described with a single plane of elements. This approach is based on Kodak's extensive experience in understanding the structural and optical behavior of light-weight mirrors.

The unit loads were applied to two radii which correspond to the location of two grid points in the NASTRAN model. The remaining rms surface error after power was removed is given in Table 7.2.2-1 for each unit load at the two radii. The values are given in units of the operating wavelength of 4 micrometers. The forces and moments are assumed to act at the curved midplane of the mirror and lie in a horizontal plane.

Table 7.2.2-1 MIRROR FIGURE SENSITIVITY	
CHARACTERISTIC	PARAMETER
UNIT FORCE (LB, @ 15.441 IN. RAD)	$.914 \times 10^{-4} \lambda$ RMS
UNIT FORCE (LB, @ 20.389 IN. RAD)	$1.669 \times 10^{-4} \lambda$ RMS
UNIT MOMENT (IN.-LB, @ 15.441 IN. RAD)	$.555 \times 10^{-4} \lambda$ RMS
UNIT MOMENT (IN.-LB, @ 20.389 IN. RAD)	$.661 \times 10^{-4} \lambda$ RMS

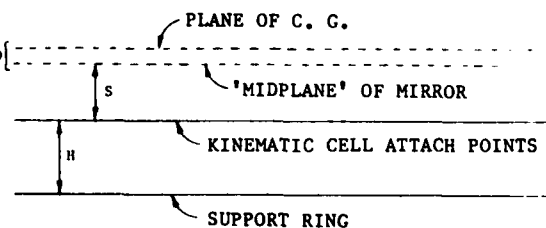
Figure 7.2.2-1 shows the geometry involved in the study. The support ring radius, R_r , was held equal to the mirror radius at 27.81 inches. The radius, R_m , and the angle, θ_m , at which the two legs attach to the kinematic cells, were fixed at 17.872 inches and 30.236 degrees, respectively. This placed the end of the legs at the x and y Cartesian coordinates of ± 9.0 inches and 15.441 inches, respectively. The other two bipods (not shown) are positioned at intervals of 120 degrees about the mirror.



CRYOGENIC MIRROR MOUNT

Figure 7.2.2-1

Figure 7.2.2-2 shows the vertical location of several planes which are referred to in the analysis. The vertical height, H , of the legs was a variable which took on values ranging from 9 to 20 inches. The separation, S , between the (curved) midplane of the mirror and the plane at which both the main legs and secondary flexures attach to the kinematic cell was fixed at 9.75 inches. This allowed



VERTICAL LOCATION OF PLANES

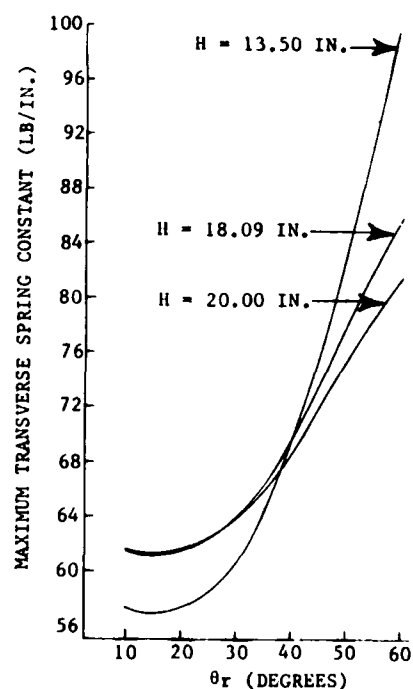
Figure 7.2.2-2

an average vertical separation of 5.75 inches between the back surface of the mirror and the kinematic cells. At the radial distance of 15.441 inches, the separation, D , between the horizontal plane containing the center of gravity and the midplane was 0.9307 inch.

For this analysis, it was assumed that the mirror and the mount will undergo an isothermal temperature change of 200°K during operation. The dimensional changes experienced by the mirror and mount materials, expressed as a percentage, are given in Table 7.2.2-2.

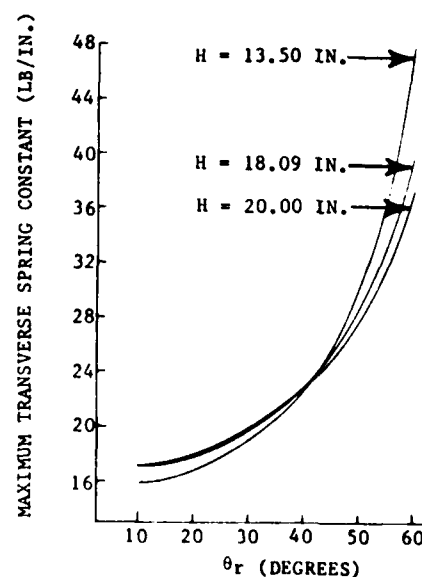
Table 7.2.2-2 PERCENT DIMENSIONAL CHANGE (200°K DELTA TEMPERATURE)	
MATERIAL	DIMENSIONAL CHANGE (%)
FUSED SILICA	-0.0047
INVAR	-0.0137
TITANIUM	-0.156
ALUMINUM	-0.370

The results of this analysis are shown in Figures 7.2.2-3 through 7.2.2-7. These graphs show the transverse spring constant of the support legs that just yield an rms surface figure error of 0.005 wave for four different combinations of materials and several support leg heights; therefore, the values shown represent the maximum values that may be permitted. The figure error, produced separately by errors that were calculated for each load type were added together to get the total rms error for a given configuration. Only those force and moment components from the legs of a bipod that do not cancel one another are effective in distorting the mirror.



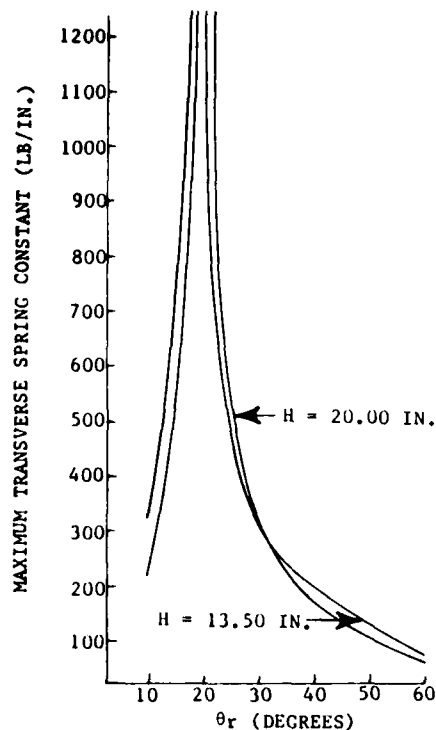
TITANIUM LEG- TITANIUM RING

Figure 7.2.2-3



TITANIUM LEG - ALUMINUM RING

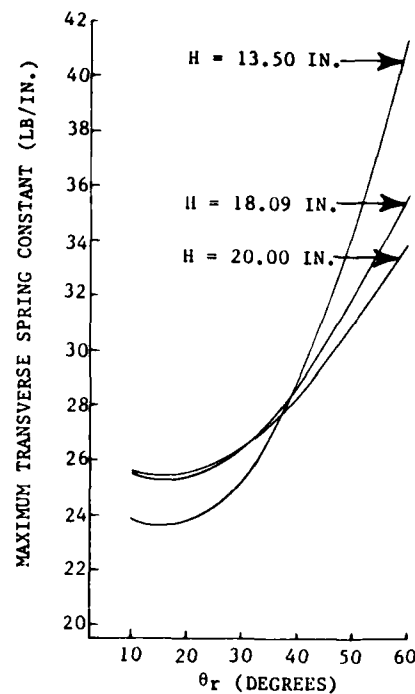
Figure 7.2.2-4



ALUMINUM LEG - TITANIUM RING

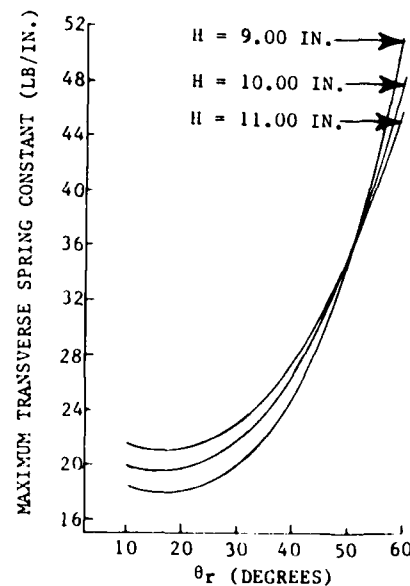
Figure 7.2.2-5

The singularity, shown in Figure 7.2.2-5, is real and indicates that no net load is transmitted to the mirror by the kinematic cell for θ_r slightly less than 20 degrees. The legs do undergo some bending, but in a direction that is opposed by the opposite leg in the bipod. This situation will occur whenever the thermal contraction of the leg is great enough to offset the decrease in the radius of the support ring. The very high transverse spring constants indicated in this figure represent a favorable situation. The vertical movement of the mirror is quite substantial in this configuration, however, much more so than for an all aluminum structure.



ALUMINUM LEG - ALUMINUM RING

Figure 7.2.2-6



ALUMINUM LEG - ALUMINUM RING

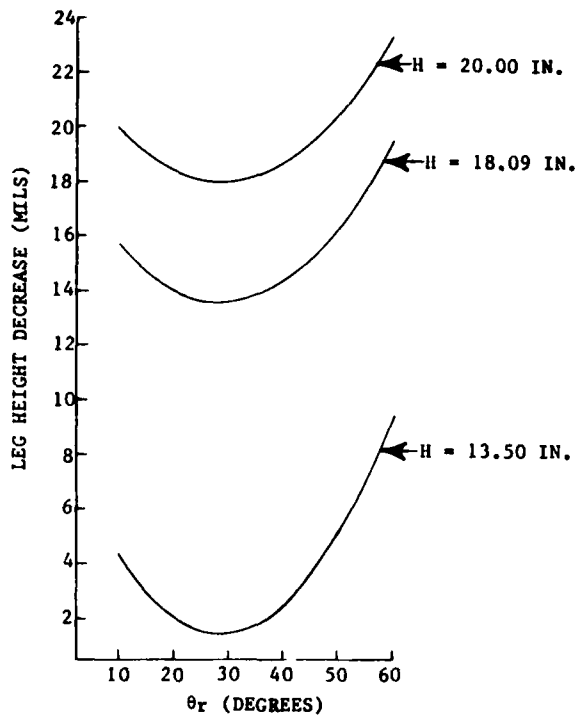
Figure 7.2.2-7

Other considerations will also prevent us from taking full advantage of the singularity. Fortunately, it was established that the need for an rms figure error of less than 0.005 wave does not represent a significant design constraint.

7.2.3 Effect of Mount Materials on Vertical Movement of Mirror

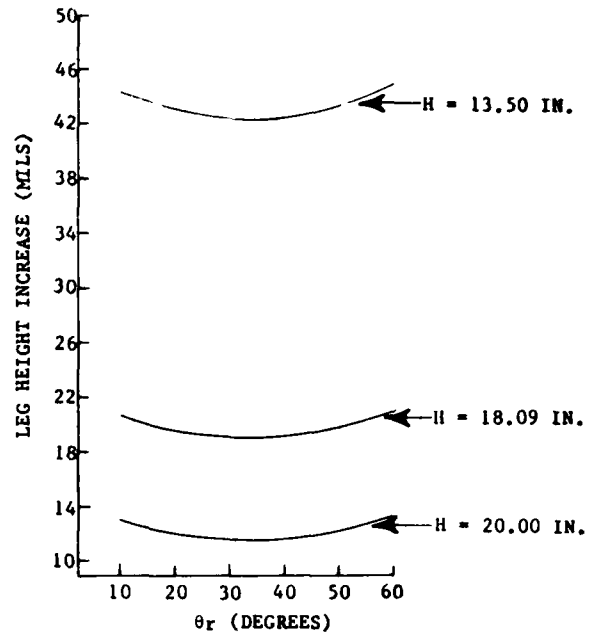
Any movement of the primary mirror along the axis of an optical system will cause a blurring of the image and a change in the image scale. It is important, therefore, to design the system such that it is insensitive to disturbances (e.g., temperature fluctuations) that might cause such a motion, and to keep any static shift in the location of the image as small as possible. A system cooled to cryogenic temperatures will probably have some sort of active or semiactive focus control, but it is a good design practice to keep the need for such correction as small as possible.

Change in the vertical height of the main support legs upon reaching operating temperature was determined for the same set of cases analyzed in the previous section. The height change of the legs will generally be the largest contributor to the movement of the primary mirror. Other sources of focus change, which were not analyzed in this section, include height change of the support ring and the Invar transition structure, change in the radius of curvature of the mirror due to thermal contraction, and change in the curvature of the mirror due to the stresses applied by the mounts. Figures 7.2.3-1 through 7.2.3-5 show the results; the units of displacement are in one-thousandths of an inch. Note that some of the graphs represent a height increase rather than a decrease. The common occurrence of a minimum or maximum in the functions at approximately 30 degrees is directly related to the fact the θ_m is equal to 30.236 degrees. If the kinematic cell was made of the same material as the mirror, the function extreme would occur exactly at θ_r equal to θ_m . The area around 30 degrees represents a favorable region in which to locate the support legs, since the vertical movement of the legs will be insensitive to their exact location; however, construction of the mount system in this configuration is prohibited by the dynamic and static behavior of the mirror/mount structure under loads.



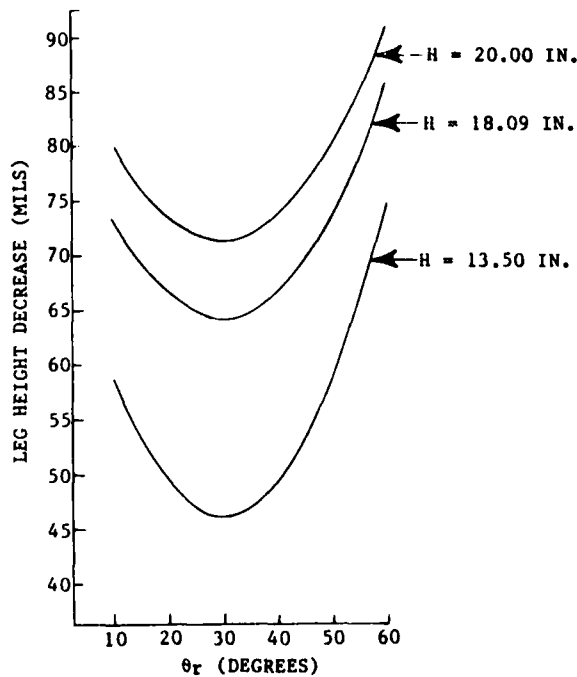
TITANIUM LEG - TITANIUM RING

Figure 7.2.3-1



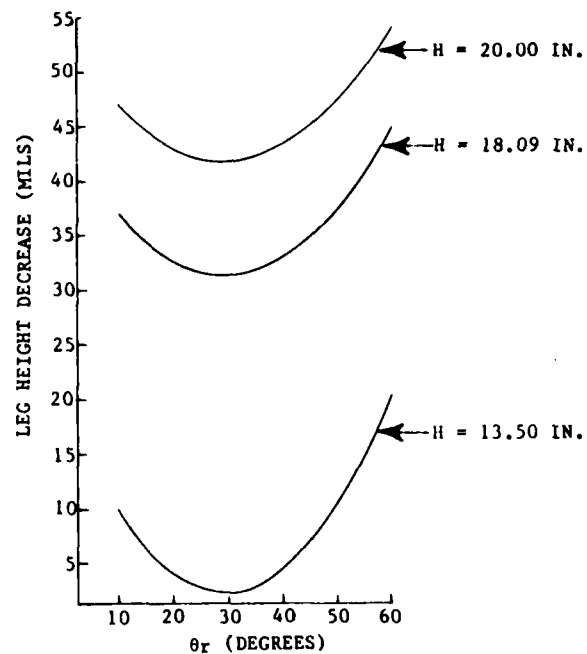
TITANIUM LEG - ALUMINUM RING

Figure 7.2.3-2



ALUMINUM LEG - TITANIUM RING

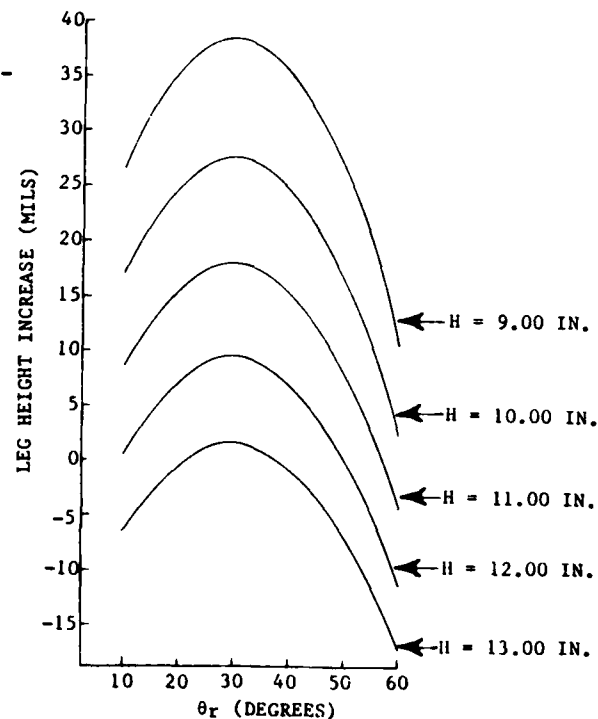
Figure 7.2.3-3



ALUMINUM LEG - ALUMINUM RING

Figure 7.2.3-4

Figure 7.2.3-5 shows the height increase of the legs for a support system consisting of an aluminum leg (flexure) and an aluminum ring. An initial leg height of 10 inches results in a height growth of 10 to 2.5 mils for θ_r in the range of 55 to 60 degrees. A value of θ_r in this range also represents a region in which a relatively high transverse spring constant for the legs is permitted. A positive change in the leg height is desirable since it can serve to offset any downward movement of the primary mirror from other sources. This configuration, which consists of an aluminum ring and leg and a leg height of 10 inches, formed the support structure baseline system for which feasibility was demonstrated.



ALUMINUM LEG - ALUMINUM RING

Figure 7.2.3-5

7.2.4 Fundamental Mode of Mirror/Mount Structure

During a Space Shuttle flight, the mirror will be subjected to dynamic and acoustic environments. These vibrations are potentially destructive in that they can result in large amplitude periodic motion of the mirror/mount structure. The restraining forces induced by the motion near mirror resonance build up to a level several times greater than the external exciting force. In order to prevent these forces from building up to a destructive level, the lowest natural frequency of the mirror mount system must lie above the vibrational noise spectrum reaching the mirror. For this study, the fundamental mode of the system was required to have a natural frequency greater than 30 hertz.

Factors that determine the fundamental frequency of the mirror/mount structure are the mass and moments of inertia of the mirror, the spring constants of the structural elements and joints between the mirror and the support ring, and the vibrational mode shape. The assumed weight of the mirror, which was 190 pounds for this analysis, represents an increase of 13.5 pounds over the calculated weight of the mirror. The extra weight partially takes into account the weight of the kinematic cells and the mount attachments. The mirror was assumed to be an 8-inch thick homogeneous annular disk, with the center of gravity at the same location as the center of gravity of the actual mirror. The main support legs are a principal contributor in determining the effective spring constant of the mirror/mount structure, and was the only contributor included in the parametric analysis. Other important contributors to the spring constant are the mount attachments and the flexures that connect the kinematic cells to the mirror. The stiffness of these components are not design-limited to the same extent as are the main support legs, in which the need for adequate longitudinal stiffness conflicts with the need for compliance in bending.

The analysis determined the minimum longitudinal spring constant for a support leg that would yield a fundamental mode frequency of 50 hertz. The system consisted of a rigid support ring which is connected to the mirror by six legs that can carry loads under tension or compression but not in bending. The mirror is a rigid structure capable of moving with six degrees of freedom. The kinematic cells are considered massless extensions of the mirror. A computer program was used by means of an iteration process to determine the vibrational mode of the structure with the lowest frequency. The spring constant of the legs were then adjusted either up or down so that the fundamental mode frequency would have a constant value of 50 hertz. The results for a number of different support leg heights are shown in Figure 7.2.4-1.

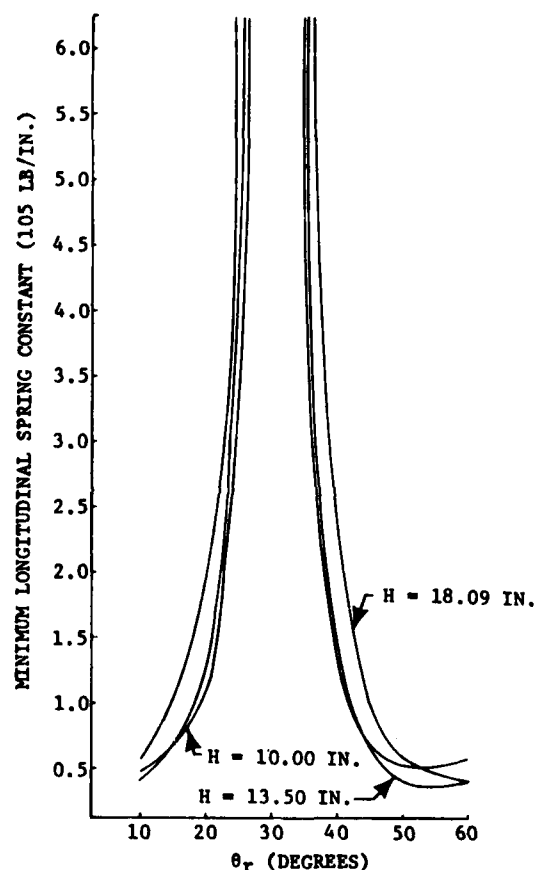
The curves show a strong singularity which occurs at θ_r equal to 30.236 degrees. At this angle the legs intersect at a virtual point lying above the center of the mirror, causing the mirror to behave as though it is suspended from this point. A swinging or rotating motion of the mirror about this point will cause the legs to deflect in a direction perpendicular to their

length, thereby exerting no restraining force. The natural frequency of this mode then approaches zero to the level of approximation used in the analysis. It can be seen that the strong dependence of the minimum required longitudinal spring constant of θ_r effectively eliminates from consideration the angles between 17 and 42 degrees, whereas the dependence of the mount-induced surface error on θ_r indicates that, in general, we should operate in the higher end of the range.

A leg height of 13.5 inches permits a lower value for the spring constant than either of the other two heights for θ_r between 45 and 60 degrees and, therefore, appears to be the most favorable. It might actually be more advantageous to operate at a somewhat lower leg height than 13.5 inches, since a higher spring constant can be achieved for a given leg diameter at a lower leg height.

7.2.5 Flight-Induced Loads

Vehicles in the Space Shuttle cargo bay will be subjected to dynamic acceleration loading during each of the elements of a Shuttle mission. Proper design of the main support legs requires knowledge of the maximum compressive load that will be experienced by the legs. A computer analysis was performed to determine these loads.



LEG STIFFNESS FOR A 50 HERTZ
FUNDAMENTAL MODE

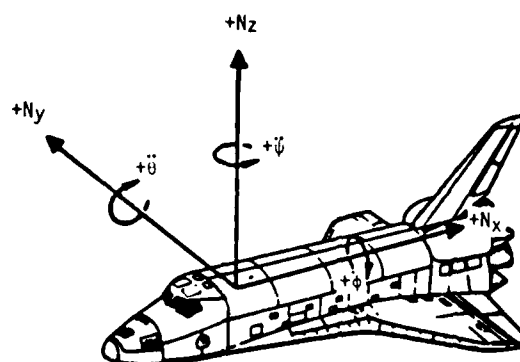
Figure 7.2.4-1

The loads were determined for 16 different occurrences of a simultaneous linear and angular accelerations in the x, y, and z directions. The accelerations used, shown in Table 7.2.5-1, were taken from NASA Document JSC 07700,

Volume 14, Attachment 1, ICD 2-19001. Forces were calculated, using a mirror which was placed in the cargo bay with its optical axis aligned along the x axis of the Shuttle coordinate system (shown in Figure 7.2.5-1). The orienta-

tion of the support structure about the optical axis was varied until the least favorable orientation was found. The loads were determined for the cases in which the mirror faced either toward the front or toward the back of the Shuttle. The maximum compressive loads were found to occur when the mirror was facing toward the rear. The tensile loads were 12 to 20 percent smaller. These results are shown in Figure 7.2.5-2.

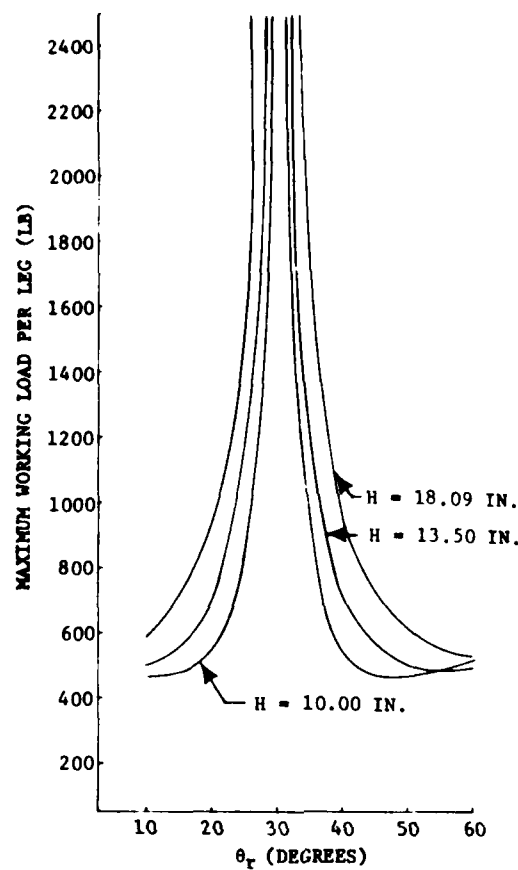
Table 7.2.5-1							
CARGO LIMIT-LOAD FACTORS/ANGULAR ACCELERATIONS FOR PRELIMINARY DESIGN (TRANSIENT FLIGHT EVENTS)							
FLIGHT EVENT	LOAD FACTOR g			ACCELERATION RAD/SEC ²			CARGO WEIGHT
	Nx	Ny	Nz	$\ddot{\phi}$	$\ddot{\theta}$	$\ddot{\psi}$	
<u>ASCENT</u> LIFT-OFF	-0.2 -3.2	±1.4	2.5 -2.5	±1.4	±3.2	±0.8	UP TO 65 KLB (29484 Kg)
<u>DESCENT</u> LANDING	1.8 -2.0	±1.5	+4.2 -1.0	±1.5	±2.5	±0.75	UP TO 32 KLB (14515 Kg)



SHUTTLE COORDINATE SYSTEM

Figure 7.2.5-1

The singularity that occurs at θ_r equal to 30.236 degrees has the same interpretation as that given in the analysis of the minimum required longitudinal spring constant. At an angle of 60 degrees, the three heights have a difference in compressive loads of less than 40 pounds with a height of 13.5 inches being the most favorable. However, a height of 10 inches is best for angles below 55 degrees.



FLIGHT-INDUCED COMPRESSIVE LOADS

Figure 7.2.5-2

7.2.6 Support Leg Design Analysis

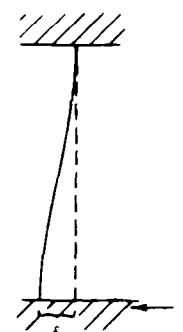
The main support legs must fulfill a number of requirements. They must be sufficiently compliant under bending so as not to cause excessive deformation of the mirror surface when cooled to the system operating temperature. Their longitudinal stiffness must be high enough so that the frequency of the fundamental mode lies above the bulk of the vibrational noise spectrum reaching the primary mirror. Finally, they must not yield or buckle when subjected to the normal Shuttle flight loads. A specific requirement is that the stress level not exceed the precision elastic limit at any point in the leg. In addition to pure compressive stresses, column (bending) stresses should be considered in determining the stress levels. These requirements cause a

very complicated problem, particularly when the constraints on the design are severe. A computer program was written during this study in order to satisfy these requirements.

The general shape acquired by the neutral axis of a leg when subjected to a bending force or a buckling force is shown in Figures 7.2.6-1 and 7.2.6-2. In each case the ends are constrained such that the surfaces remain parallel to each other.

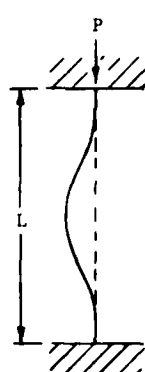
In the program the leg consists of a middle section and two end sections over which the diameter of the leg remains constant. The leg necks down to a smaller diameter at two other sections placed symmetrically around the middle. Figure 7.2.6-3 shows one-half of

such a leg. The length of these sections is specified by the user and remains fixed in the program. The central portion of each narrow section contains a region of constant diameter. The transition between the two diameters is accomplished through a fillet with a specified radius of curvature.



SHAPE OF NEUTRAL AXIS
UNDER TRANSVERSE LOADS

Figure 7.2.6-1



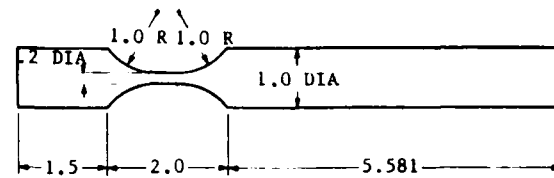
SHAPE OF NEUTRAL AXIS
UNDER LONGITUDINAL LOADS

Figure 7.2.6-2

The user specifies the length and geometry of the leg, and the program scales the transverse dimensions such that the precision elastic limit is not exceeded. The same scaling factor is applied along the entire length of the leg. The transverse and longitudinal spring constant of the leg and its weight are then calculated.

The natural buckling shape of the leg is determined by the program in order to account for the possibility of buckling and the accompanying stresses. The stress level within the leg is a function of the extent to which the neutral axis deviates from a straight line under zero

load. The shape of this deviation is assumed to be the same as the natural buckling shape of the leg. The peak-to-peak magnitude of the deviation, or wobble, is specified by the user.

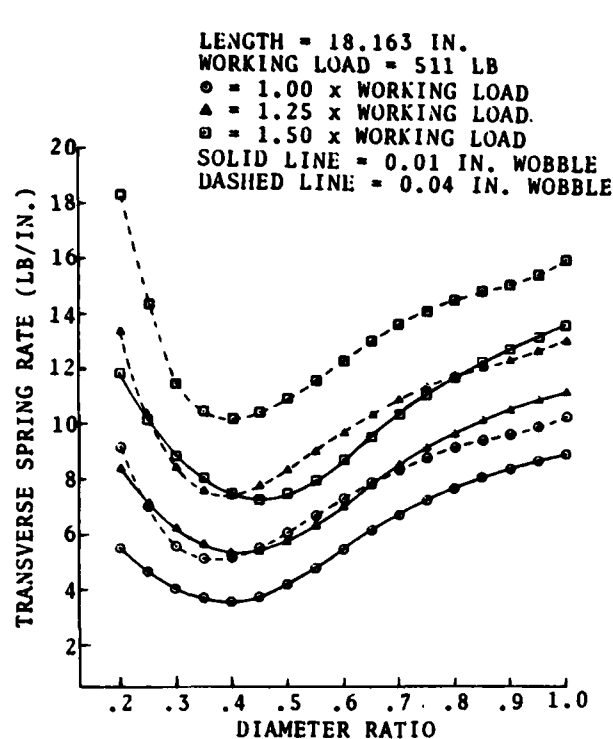


SUPPORT LEG GEOMETRY

Figure 7.2.6-3

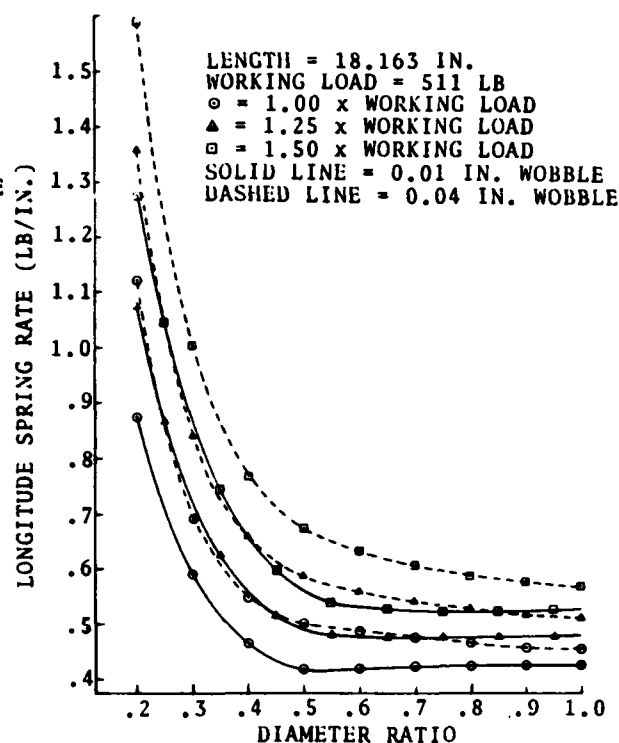
The design of a leg was performed for a single support structure configuration that corresponded to a leg height of 10 inches and a θ_r of 60 degrees. This resulted in an overall leg length of 18.163 inches. The aluminum aircraft alloy 2014-T6 was chosen as the leg material. The alloy has a 0.2 percent yield strength of 53,000 psi and a (compressive) elastic modulus of 10.7×10^6 psi.* The precision elastic limit was estimated by the general rule of thumb that it is approximately one-half the yield strength of the material; therefore, the stress level which produces a permanent set of 0.01 percent is assumed to be 26,500 psi for this alloy. The longitudinal position of the various sections of the leg are as shown in Figure 7.2.6-3. The basic geometry of the leg was held fixed except for the diameter of the narrow portion of the leg. This diameter formed the principal variable in the analysis and is specified as a fraction of the maximum leg diameter. The maximum compressive force experienced by a leg for this support structure configuration is 511 pounds. The analysis determined the characteristics of a leg that is capable of supporting 1.0, 1.25 and 1.5 times the maximum compressive load. For each of these loads a wobble of 0.01, 0.02, and 0.04 inch was assumed. The resulting transverse and longitudinal spring rate of the leg is shown as a function of the ratio of the minimum leg diameter to the maximum leg diameter in Figures 7.2.6-4 and 7.2.6-5, respectively. The curves corresponding to a wobble of 0.02 inch are not shown.

*MIL-HDBK-5B, "Metallic Materials and Elements for Aerospace Vehicle Structures," 1 September 1971.



SUPPORT LEG TRANSVERSE SPRING RATE

Figure 7.2.6-4



SUPPORT LEG LONGITUDINAL SPRING RATE

Figure 7.2.6-5

The requirements for the given support structure configuration can be determined from Figures 7.2.2-7 and 7.2.4-1. It is seen that the leg is required to have a transverse spring constant of less than 48 pounds per inch and a longitudinal spring constant of greater than 5.8×10^4 pounds per inch. All the design curves shown in Figure 7.2.6-4 lie well below the maximum allowed transverse spring constant. For each curve shown in Figure 7.2.6-5, a value for the diameter ratio can also be found below which the longitudinal spring constant is above the minimum required value. It is possible, therefore, to select a leg design that will meet all the requirements while at the same time provide comfortable margins of safety.

The behavior of the curves in Figure 7.2.6-4 can be simply explained. The maximum stress in a leg that has a diameter ratio between approximately 0.4 and 0.5 occurs in the transition zone between the minimum and maximum leg diameters, close to the beginning of the narrow portion of the leg. In order to maintain a fixed stress level, the maximum leg diameter must increase as

the diameter ratio is reduced, while at the same time the minimum leg diameter experiences a net decrease. The decrease in the minimum leg diameter tends to be the controlling factor, however, and the transverse spring constant goes down. As the region of maximum stress moves deeper into the narrow portion of the leg, the minimum leg diameter decreases less rapidly. The reduced flexibility of the other portions of the leg then becomes the determining factor, causing the curves to flatten out. The minimum leg diameter ultimately begins to increase and the transverse spring constant goes up sharply. The curves will eventually approach a finite value as the diameter ratio goes to zero. Figure 7.2.6-5 can be explained through the same set of arguments.

7.3 CRYOGENIC MIRROR MOUNT PERFORMANCE EVALUATION

7.3.1 Mirror/Mount System Performance

A mirror/mount design, which met the requirements for both the longitudinal and transverse spring constant, was selected from the support leg analysis. The mount configuration selected corresponds to a vertical leg height of 10 inches and a θ_r of 60 degrees. The resulting system performance for this configuration is described in this section. The leg design and support structure meet all the previously mentioned system requirements, but are not necessarily presented as a final design.

The leg design which was selected had an assumed initial eccentricity of the neutral axis of 0.02 inch. This represents a liberal estimate of the extent to which the neutral axis of the leg might deviate from a straight line due to manufacturing errors, as well as providing an additional factor of safety in the analysis. The maximum compressive load permitted to act on the leg is equal to 1.25 times the calculated value of 511 pounds. At this maximum load the precision elastic limit is just reached within the leg. Examination of the computer results for this case showed that a diameter ratio of 0.2 provides a reasonable tradeoff between having both a low transverse spring constant and high longitudinal spring constant, while at the same time keeping

the overall bulk of the leg at a manageable level. Figure 7.2.6-3 shows the dimensions, in inches, of the leg design arrived at by this analysis, and Table 7.3.1-1 gives the important properties.

The compressive elastic modulus was used in generating the curves shown in Figures 7.2.6-4 and 7.2.6-5. This was done so that the correct value for the modulus could be used in the internal buckling calculations. In determining the transverse and longitudinal spring constant of a leg, however, the

Table 7.3.1-1 SUPPORT LEG PROPERTIES	
CHARACTERISTIC	PARAMETER
ELASTIC MODULUS, @ 20°C (LB/IN. ²)	10.5x10 ⁶
ELASTIC MODULUS, @ LOW TEMP. (LB/IN. ²)	11.65x10 ⁶
COMPRESSIVE ELASTIC MODULUS, @ 20°C (LB/IN. ²)	10.7x10 ⁶
DENSITY (LB/IN. ³)	0.101
WEIGHT (LB)	1.19
TRANSVERSE SPRING CONSTANT, @ 20°C (LB/IN.)	11.34
TRANSVERSE SPRING CONSTANT, @ LOW TEMP. (LB/IN.)	12.58
LONGITUDINAL SPRING CONSTANT, @ 20°C (LB/IN.)	1.237x10 ⁵

tensile elastic value is usually used. This is reflected in the room temperature values for the spring constants shown in Table 7.3.1-1. Similarly, in order to determine the rms figure error induced in the mirror by the mounts, the transverse spring constant at the operating temperature should be used. The elastic modulus is approximately 11 percent higher than the room temperature value at an operating temperature of 100°K. The corresponding change in the transverse spring constant is given in the table.

The power change in the mirror surface and the rms surface error after power has been removed was determined for this particular support system configuration. A NASTRAN model was run in which a radial inward force and an outward turning moment acted simultaneously at three points on the midplane of the mirror at a radius of 15.441 inches. The size of the loads correctly reflected the support system geometry and the transverse spring constant of the legs at the operating temperature. The resulting surface deflection was analyzed for power change (sag) and residual rms surface error.

The loads applied to the mirror at the support points and the resulting surface deflections are given in Table 7.3.1-2. The figure error is given in units of the operating wavelength of 4 micrometers; the induced sag is

measured from the center of the mirror. The changes in the position of the mirror's focal point, due to the mount induced change in the radius of curvature of the mirror, the thermal contraction of the mirror, and the height change of the main support legs, are also given in the table. (Not included in this list is the very sizable contribution to focus shift by the thermal contraction of the aluminum support ring along the optical axis.) Finally, the resonant frequency of the mirror/mount system is given under the assumption that the support legs are the only compliant component in the structure. The longitudinal spring constant given in Table 7.3.1-1 was used in the calculation.

Table 7.3.1-2 MIRROR/MOUNT SYSTEM PERFORMANCE	
CHARACTERISTIC	PARAMETER
APPLIED FORCE (LB)	1.266
APPLIED MOMENT (IN.-LB)	18.69
MIRROR SAG (IN.)	-1.360×10^{-6}
FIGURE ERROR (λ RMS)	9.792×10^{-4}
MOUNT INDUCED FOCUS CHANGE (MILS)	0.03315
THERMALLY INDUCED FOCUS CHANGE (MILS)	-2.657
LEG HEIGHT CHANGE (MILS)	2.707
TOTAL FOCUS CHANGE (MILS)	0.08232
RESONANT FREQUENCY (HZ)	72.93

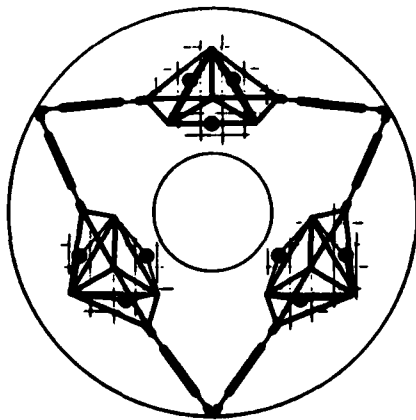
It can be seen that all of the performance goals discussed in the report can be met by a very comfortable margin. The rms figure error given is almost unmeasurable even at visible wavelengths. In addition, the resonant frequency of the structure, as modeled, is more than 45 percent greater than the design goal of 50 hertz. The near zero change in the position of the focal point is completely fortuitous. The additional negative focus shift that can be expected by the support ring contraction can be countered by moving the support leg angle θ_p to around 55 degrees instead of 60, with very little performance degradation.

7.3.2 Kinematic Cell and Attachment Geometry

The kinematic cell is a rigid structure which serves to take up any opposing loads that are applied by the support legs and distributes the loads over a greater area of the mirror's surface. This also permits a greater flexibility in the support structure geometry by not restricting a support leg to terminate at a specific point in relation to the core cells. The small size

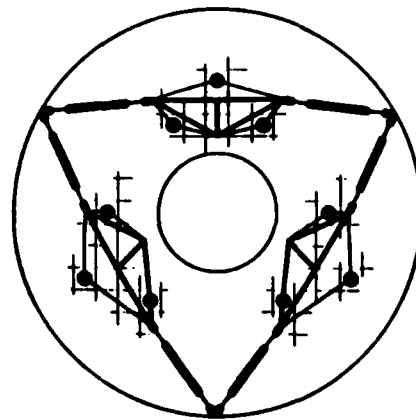
of these cells, in relation to the overall structure, permits the use of Invar in their construction without causing an excessive weight penalty.

Figures 7.3.2-1 and 7.3.2-2 show two different concepts for a kinematic cell as they might appear in the support structure configuration which was discussed previously. The topmost cell in the figures are shown from a side view in Figure 7.3.2-3. Each cell is attached to the mirror by six Invar flexures, which are arranged in pairs with the flexures to each pair positioned so that they intersect at a vertical point located within the body of the mirror along the center line of a cell. This is a constraint imposed on the flexures by the attachment concept discussed in the following section. The kinematic cells consist of a rigid tetrahedral truss structure, in which the apex of the tetrahedron is a symmetric structure that has an equilateral triangle as a base. Additional trusses extend from the sides of the tetrahedron to form the attachment for the main support legs, resulting in two additional tetrahedrons. The points at which the support legs are attached to the cell lie in the same horizontal plane as the base of the main tetrahedron. Figure 7.3.2-4 shows an artist's sketch of a perspective view of Concept 1.



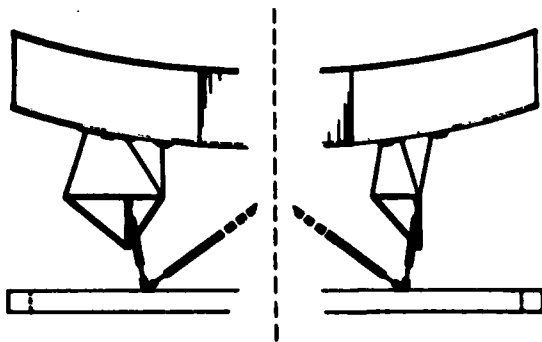
CONCEPT 1 OF A KINEMATIC CELL

Figure 7.3.2-1



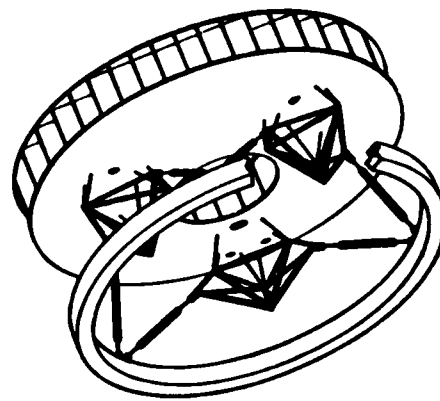
CONCEPT 2 OF A KINEMATIC CELL

Figure 7.3.2-2



SIDE-VIEW OF KINEMATIC CELLS

Figure 7.3.2-3



PERSPECTIVE VIEW OF CONCEPT 1

Figure 7.3.2-4

Concept 2 represents a lighter weight design, which has a single asymmetric tetrahedron forming the cell. The support legs are attached to the base of the cell at two of the vertices. The advantage of this design over Concept 1 is its potentially lighter weight and simpler construction. The maximum number of struts and legs that terminate at a common point is six for this design versus seven for the previous design. The disadvantages of Concept 1 are the greater asymmetry in the length and position of the Invar flexures, and the location of the attachment points. This may result in a significant lateral shift or tilt of the mirror upon reaching the operating temperature. Greater peak loads may also be placed upon individual flexures and attachments during flight due to geometrical considerations. The degree to which these considerations may present a problem is unknown, however, and may be alleviated through detailed design.

The maximum compressive load experienced by a flexure during a Shuttle flight was determined for Concept 1 using the same computer programs that determined the maximum load experienced by a support leg. The fundamental mode frequency of the system, in which the flexures and the support legs both act as compliant members, was also determined. The support structure configuration and the support leg design in the analysis was the same as previously discussed. Each pair of Invar flexures was angled so that they intersected in the curved midplane of the mirror above the center of the core cells indicated in Figure 7.3.2-1. It is desirable to have the six flexures between the

kinematic cell and the mirror be, in the aggregate, at least twice as stiff as the two support legs. A simple calculation which ignored geometric considerations showed that the flexures should have a longitudinal spring constant of at least 0.8×10^5 lb/in. Therefore, all the flexures were given a spring constant of this value in the program, and the resulting system fundamental mode frequency was determined.

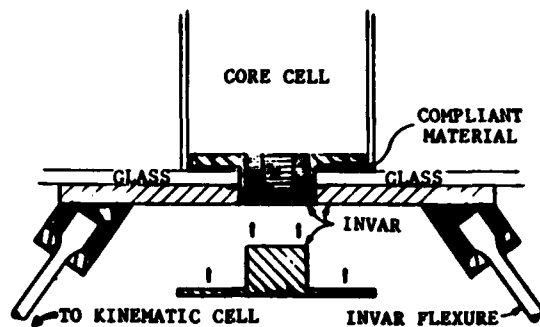
The analysis showed the system had a fundamental mode frequency of 48.3 hertz, and the maximum compressive force on a flexure was 468.5 pounds. The length of the flexures ranged from 6.067 to 7.799 inches. Since the flexures had a fixed longitudinal spring constant, the cross sectional areas also varied from 0.0255 to 0.0328 square inch with an assumed modulus of 19.0×10^6 psi. If the worst case is assumed, in which the maximum stress on a flexure (ignoring buckling) will be 18,373 psi. Since the precision elastic limit for Invar can range from 18,000 to 25,000 psi, it can be seen that this first cut design of the Invar flexures is close to what is required as far as the fundamental frequency and stress levels are concerned.

7.3.3 Mount Attachment Concept

A critical factor in any mirror mounting scheme is the means by which the mount structure is attached to the mirror. The mount attachment can present a severe design problem when the mirror is subjected to both Shuttle flight loads and large, thermally-induced, dimensional changes in the mount structure. Part of the problem lies in the high temperatures used in constructing an ultra lightweight mirror, which does not allow the designer to build or place an attachment device within the mirror prior to assembly.

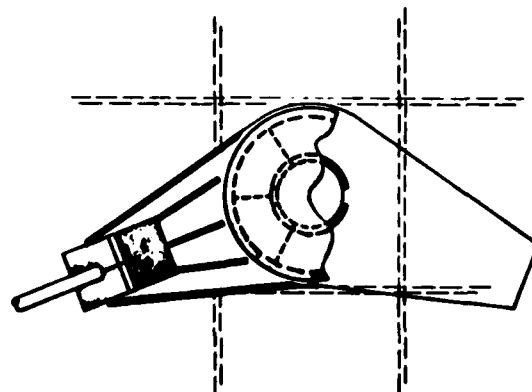
The mount attachment concept developed during the study is shown in Figures 7.3.3-1 and 7.3.3-2. The fixture consists of an Invar plate which is clamped to the back of the mirror. Posts are welded to this baseplate, into which Invar flexures are set. The flexures are bolted to the posts. The other end of the flexures are connected to the kinematic cell. The baseplate is held to the back of the mirror by a threaded Invar cap, which screws into a pipe

with an inside thread to which a plate has been attached at one end. The pipe and plate are cut into six pieces and passed through a hole in the back of the mirror which is centered on a core cell. The threaded pipe is then reassembled with the plate on the inner surface of the back face of the mirror. Spacers between the sections replace the material that has been cut away. In order to take up any irregularities in the surfaces and reduce local stress levels, a compliant material can be placed between the Invar plate and fused silica backplate. This material could be RTV, which is bonded to the Invar and scored into small sections. Another possibility would be a Teflon material which can maintain plasticity down to very low temperatures.



MOUNT ATTACHMENT CONCEPT

Figure 7.3.3-1



MOUNT ATTACHMENT CONCEPT

Figure 7.3.3-2

Figure 7.3.3-2 shows the mount attachment concept as seen from the back of the mirror. The pipe sections are prevented from rotating when the cap is screwed in place by a key on the baseplate, as shown in the figure. Stiffening ribs can also be seen on the left half of the baseplate (not shown on the right half) which would prevent the plate from bending when a tensile load is applied to the flexures. No detailed engineering of this attachment concept was performed during the study; an important part of any follow-on program would be to design, build, and test this concept thoroughly.

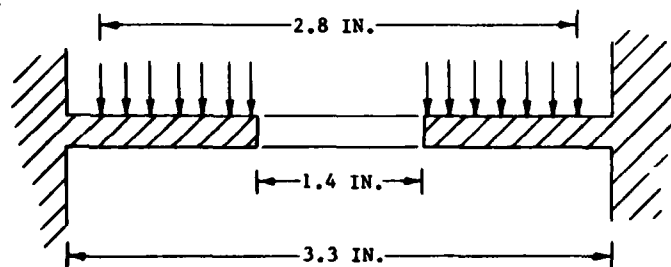
The maximum shear, tensile, and compressive force which the mount attachments would experience during a normal Shuttle flight were determined during the study. The loads on the structure were the same as described in Section 7.2.5, but with the assumed weight of the mirror taken to be its actual weight

of 176.5 pounds. The supporting structure was Concept 1, which was identified in the previous section. The precise geometry of the Invar flexures and the combined effect of each pair of flexures on the mount attachments were taken into account in the analysis. The results indicated that the maximum shear, tensile, and compressive force which a mount attachment would experience under normal conditions are 321 pounds, 327 pounds, and 412 pounds, respectively.

An estimate was made of the tensile stresses that would be induced in the backplate of the mirror when a tensile load of 327 pounds is applied to a mount attachment. The plate was modeled as an annular disk of fused silica, with its outer edge held fixed and its inner edge free. The mount was assumed to apply a uniform load from the inner edge of the disk out to a radius of 1.4 inches. The assumed conditions are shown in Figure 7.3.3-3. The diameter of the disk was chosen so that the area was equal to the free area of the core cell. The results indicated that

at the outer edge of the disk, a maximum tensile stress of 1065 psi would be generated. This compares favorably with a 7190 psi modulus of rupture for abraded fused silica, and an empirical modulus of rupture of several thousand psi for a frit-

bonded, fused silica L-joint. Compressive loading of the mount should not cause a stress problem due to the greater area of contact that occurs. The shear strength of the mount was not estimated, since it is dependent on the clamping force between the glass and metal, the coefficient of static friction, and the precise nature of the metal-to-glass contact within the hole. The shear strength is probably best determined on an experimental basis.



GEOMETRY AND LOAD CONFIGURATION FOR FLAT
PLATE STRESS ANALYSIS

Figure 7.3.3-3

DISTRIBUTION LIST

Capt. Doris Hamill RADC/OCSE	7
RADC/TSTD GRIFFISS AFB NY 13441	1
RADC/DAP GRIFFISS AFB NY 13441	2
ADMINISTRATOR DEF TECH INF CTR ATTN: DTIC-DDA CAMERON STA BG 5 ALEXANDRIA VA 22314	12
HQ ESC (XPZP) SAN ANTONIO TX 78243	1
HQ ESC/DOO SAN ANTONIO TX 78243	1
DMAAC/STT ST LOUIS AFS MO 63118	1
DMA HYDROGRAPHIC/TOPOGRAPHIC CENTER ATTN: STT WASHINGTON DC 20315	2

DIRECTOR 1
DMAHTC
ATTN: SDSIM
6500 Brookes Lane
WASH DC 20315

RACC/RBRAC 1
GRIFFISS AFB NY 13441

HQ AFSC/DLAE 1
ANDREWS AFB DC 20334

HQ AFSC/XRTD 1
ANDREWS AFB DC 20334

HQ AFSC/XRKR 1
ANDREWS AFB MD 20334

HQ AFSC/XRK 1
ANDREWS AFB MD 20334

HQ SAC/NRI (STINFO LIBRARY) 1
OFFUTT AFB NE 68113

3245 TESTW/TZE 1
EG AFB FL 32542

TAFIG/IID0 1
LANGLEY AFB VA 23665

HQ TAC/XPS (STINFO)
LANGLEY AFB VA 23665

1

HQ TAC/DRCT
LANGLEY AFB VA 23665

1

HQ TAC/DRF
LANGLEY AFB VA 23665

1

AFSC LIAISON OFFICE
LANGLEY RESEARCH CENTER (NASA)
LANGLEY AFB VA 23665

1

ASD/XRS
WRIGHT-PATTERSON AFB OH 45433

1

AFWAL/MLP
WRIGHT-PATTERSON AFB OH 45433

1

AFWRL/HE
WRIGHT-PATTERSON AFB OH 45433

1

AFHRL/OTS
Williams AFB AZ 85224

1

HQ ADCOM/SPACECOM/XPY
ATTN: DR W R MATDOUSH
PETERSON AFB CO 80914

1

3420 TCHTG/TTMNL
LOWRY AFB CO 80230

1

CODE R141B TECHNICAL LIBRARY
DEFENSE COMMUNICATIONS
ENGINEERING CENTER
1860 WIEHLE AVENUE
RESTON VA 22090

1

COMMANDER
BALLISTIC MISSILE DEFENSE SYSTEMS COMMAND
ATTN: BMDSC-AOLIB
PO BOX 1500
HUNTSVILLE AL 35807

1

DET 1, AFOSR
EOARD/CI
TECHNICAL INFORMATION OFFICE
BOX 14
FPO NEW YORK NY 09510

1

COMMANDING OFFICER
NAVAL AVIONICS CENTER
LIBRARY - CODE 765
INDIANAPOLIS IN 46218

1

COMMANDING OFFICER
NAVAL TRAINING EQUIPMENT CENTER
TECHNICAL INFORMATION CENTER
BUILDING 2068
ORLANDO FL 32813

1

COMMANDER
NAVAL OCEAN SYSTEMS CENTER
ATTN: TECHNICAL LIBRARY, CODE 4473B
SAN DIEGO CA 92152

1

US NAVAL WEAPONS CENTER, CODE 343
ATTN: TECHNICAL LIBRARY
CHINA LAKE CA 93555

1

SUPERINTENDENT (CODE 1424)
NAVAL POSTGRADUATE SCHOOL
MONTEREY CA 93940

1

COMMANDING OFFICER
NAVAL RESEARCH LABORATORY
CODE 2627
WASHINGTON DC 20375

1

REDSTONE SCIENTIFIC INFORMATION CENTER
ATTN: DRSMI-RPRD
US ARMY MISSILE COMMAND
REDSTONE ARSENAL AL 35809

2

MILITARY SEALIFT COMMAND
TECHNICAL INFORMATION CENTER M-16
DEPARTMENT OF THE NAVY
WASH DC 20390

1

ADVISORY GROUP ON ELECTRON DEVICES
FTS (FEDERAL COMM SYSTEM)
201 VARICK STREET, Rm 1140
NEW YORK NY 10014

2

FRANK J SEILER RESEARCH LAB
FJSRL/NHL
US AIR FORCE ACADEMY CO 80840

1

LOS ALAMOS SCIENTIFIC LABORATORY
ATTN: REPORT LIBRARY
MAIL STATION 5000
PO BOX 1663
LOS ALAMOS NM 87545

1

AIR FORCE ELEMENT (AFELM)
THE RAND CORP
1700 MAIN STREET
SANTA MONICA CA 90406

1

DR RAYNER K. ROSICH
ENERGY SYSTEMS
c/o 7932 W. NICHOLS AVE.
LITTLETON CO 80123

1

AEDC LIBRARY (TECH FILES)
ARNOLD AFS TN 37389

1

1
Director
National Security Agency
ATTN: W07
Fort Meade MD 20755

1
Director
National Security Agency
ATTN: W31
Fort Meade MD 20755

1
Director
National Security Agency
ATTN: R21 VICE R2
Fort Meade MD 20755

1
Director
National Security Agency
ATTN: R5
Fort Meade MD 20755

1
Director
National Security Agency
ATTN: R091, DR. MOORE
Fort Meade MD 20755

1
Director
National Security Agency
ATTN: R7
Fort Meade MD 20755

1
Director
National Security Agency
ATTN: R8
Fort Meade MD 20755

1
Director
National Security Agency
ATTN: P207
Fort Meade MD 20755

HQ ESD/FASE
HANS COM AFB MA 01731

1

HQ ESD/TCSR (BURT HOPKINS)
HANS COM AFB MA 01731

1

ESD/XRT
HANS COM AFB MA 01731

1

ESD/XRVT
HANS COM AFB MA 01731

1

ESD/XRC
HANS COM AFB MA 01731

1

ESD/XRW
HANS COM AFB MA 01731

1

ESD/TCG (MR RON LANZA)
HANS COM AFB MA 01731

1

ESD/XR
HANS COM AFB MA 01731

2

HQ ESD/DCR-11
HANS COM AFB MA 01731

1

AFEWC/ESRI
San Antonio TX 78243

1

485 EIG/EIEXR (DMO)
Griffiss AFB NY 13441

2

ESD/TCS-1D
ATTN: E D SPRAGUE
HANSCOM AFB MA 01731

1

ASD/AXPP
WRIGHT-PATTERSON AFB OH 45433

1

Attn: John A Spina
Eastman Kodak Company
901 Elm Grove Rd
Rochester, NY 14650

5

Aerospace Corporation
Attn: Mr. Steve Burrin
Advanced Systems Technology Division
2400 E. El Segundo Blvd. Bldg 125/1054
El Segundo, CA 90245

1

The Aerospace Corp.
Attn: Dr. Silvertooth
P.O. Box 92957
El Segundo, CA 90009

1

Air Force Wright Aeronautical Laboratory
FIEE
ATTN: Mr. Joseph Johnson
Wright Patterson AFB, OH 45433

1

Airsearch Manufacturing Co. of California 1
Attn: Mr. Oscar Buchmann
2525 West 190th Street
Torrance, CA 90509

Analytic Decisions Incorporated 1
Attn: Mr. Richard Mollicone
5155 West Rosecrans Ave.
Suite 307
Hawthorne CA 90250

Analytic Decisions, Incorporated 1
Attn: Mr. Gary Glaser
1401 Wilson Blvd
Arlington, VA 22209

Center for Analysis 1
Attn: Mr. Jim Justice
13 Corporate Plaza
Newport Beach, CA 92660

The Charles Stark Draper Laboratory, Inc. 1
Attn: Dr. Keto Soosaar
555 Technology Square
Cambridge, MA 02139

Charles Starke Draper Labs 1
Attn: Dr. V. Mahajan
555 Technology Square
MS-65
Cambridge, MA 02139

DARPA/STO 1
Attn: Maj E. Deitz
1400 Wilson Blvd
Arlington, VA 22209

DARPA/STO 1
Attn: Lt. Col A. Herzberg
1400 Wilson Blvd
Arlington, VA 22209

DARPA/DEO 1
Attn: Col R. Prater
1400 Wilson Blvd
Arlington, VA 22209

DARPA/MIS 1
1400 Wilson Blvd
Arlington, VA 22209

General Research Corporation 1
Attn: Mr. G.R. Curry
P.O. Box 3587
Santa Barbara, CA 93105

General Research Corporation 1
Attn: Mr. Thomas Zakrzewski
7655 Old Springhouse Road
McLean, VA 22101

Hughes Aircraft Company 1
Attn: Mr. Ken Beale
Centinela & Teale Streets
Culver City, CA 90230

Hughes Aircraft Company 1
Attn: Fritz Benning
MS 6/D 126
Centinela & Teal Sts
Culver City, CA 90230

Institute of Defense Analyses 1
Attn: Dr. Hans Wolfhard
400 Army Navy Drive
Arlington, VA 22202

Itek Corporation 1
Attn: Mr. Edward Galat
10 Maguire Road
Lexington, MA 02173

Kaman Sciences Corporation Attn: Dr. Walter E. Ware 1500 Garden of Gods Road P.O. Box 7463 Colorado Springs, CO 80933	1
Lockheed Missiles & Space Company Attn: Mr. Paul Williamson 3251 Hanover Street Palo Alto, CA 94304	1
Naval Electronic Systems Command PME-106-4 Attn: Mr. Charles Good National Center I Washington, D.C. 20360	1
Naval Research Laboratory EOTPD Attn: Dr. John McCallum 4555 Overlook Ave, SW Washington, D.C. 20375	1
Naval Sea Systems Command Attn: Dr. S. Siahatgar PMS-405 NCI Room 11N08 Washington, D.C. 20742	1
NASA Ames Research Center Attn: Ramsey Mallugin MS 244-7 Moffett Field, CA 94035	1
OPTICAL SCIENCES CO Attn: Dr. D. Fried P.O. Box 446 Placentia, CA 92670	1
Perkin-Elmer Corp Attn: Mr. H. Levinstein 100 Wooster Heights Rd. Danbury, CT 06810	1

Photon Research Associates 1
Attn: Mr. Jim Myer
P.O. Box 1318
La Jolla, CA 92038

Riverside Research 1
Attn: HALO Library, Mr. Bob Passut
1701 N. Fort Myer Drive
Arlington, VA 22209

Rockwell International 1
Attn: Russell Loftman (Space Systems Group)
12214 Lakewood Blvd.
Downey, CA 90241
(Mail Code - SL 56)

Science Applications, Inc. 1
Attn: Mr. Richard Ryan
3 Preston Court
Bedford, MA 01730

SSG, Inc. 1
Attn: Joseph S. Titus
150 Bear Hill Rd.
Waltham, Mass 02154

TRW 1
Attn: Mr. Len Pincus
Bldg. P-5 Room 2031
Redondo Beach, CA 90278

IRW

University of Arizona 1
Attn: Robert Shannon
% Charles Peyton
Administration Bldg.
Tucson, AZ 85721

U.S. Army/DARCOM 1
Attn: Mr. Bernie Chasnov
AMC Bldg
5001 Eisenhower Ave
Alexandria, VA 22333

U. S. Army Missile Command
Attn: DRSMI-RAS/Mr. Fred Haak
Redstone Arsenal, AL

1

Space Division
Attn: LtCol Carey O'Brien
SD/VLVM P. O. 92960
Worldway Postal Center
Los Angeles, CA 90009

1

AFWL/ARA
Attn: Lt. Col Jim Mayo
Kirtland AFB, NM 87117

1

BMD/ATC
Attn: A. Carmichael
PO Box 1500
Huntsville, AL 35807

1

Corning Glass Works
Attn: E. T. Decker
Technical Products Division
Corning, NY 14830

1

GRC
Attn: G. Gurski
7655 Old Springhouse RD
McLean, VA 22102

1

Itek Corp
Attn: Roland Plante
Optical Systems Division
10 Maguire Rd.
Lexington, MA 02173

1

Lockheed Palo Alto Research Lab
Attn: Richard Feaster
0754-03, B201
3201 Hanover St.
Palo Alto, CA 94304

1

MRJ Corp
Attn: Dr. Kenneth Robinson
71 Blake St.
Needham, MA 02192

1

NASA Marshall Space Flight Center
Attn: Charles O. Jones
Mail Code EC32
Huntsville, AL 35812

1

United Technologies Research Center
Attn: Jeff Greenough
Optics & Applied Technology Lab
PO Box 2691
West Palm Beach, FL 33402

1

W. O. Schaffer Assoc. Inc.
Attn: Richard Dyer
Corporate Place 128
Bldg 2, Suite 300
Wakefield, MA 01880

1

Lockheed Space and Missile Co.
Attn: Dennis Aspinwall
Dept 5203 Bldg 201
3251 Hanover St.
Palo Alto, CA 94304

1

Perkin Elmer Corp
Attn: Henry Dieselman
100 Wooster Heights Road
Danbury, CT 06810

1

Martin Marietta Aerospace
Attn: C.W. Spieth
Denver Division
P.O. Box 179
Denver, CO 80201

1

MIL/Lincoln Laboratory
Attn: Alex Parker
P.O. Box 73
Lexington, MA 02173

1

RADC/ESM
Attn: Dr. Osama El Bayoumi
Hanscom AFB, MA 01731

1

Naval Weapons Center
Attn: Dr. Hal Bennett
Code 38103
Michaelson Lab
China Lake, CA 93555

1



MISSION of Rome Air Development Center

RADC plans and executes research, development, test and selected acquisition programs in support of Command, Control Communications and Intelligence (C³I) activities. Technical and engineering support within areas of technical competence is provided to ESD Program Offices (POs) and other ESD elements. The principal technical mission areas are communications, electromagnetic guidance and control, surveillance of ground and aerospace objects, intelligence data collection and handling, information system technology, ionospheric propagation, solid state sciences, microwave physics and electronic reliability, maintainability and compatibility.